First Observation of Normalised Emittance Reduction through Ionization Cooling

DRAFT - MICE Internal

C. T. Rogers

Muon ionization cooling is a technique by which muon beam emittance may be reduced in order to improve the beam transmission and luminosity. Ionization cooling is a key component of proposed muon facilities such as the Muon Collider and Neutrino Factory but until now has never been demonstrated in practice.

In this paper, the effect of focussing of muons onto an energy absorber, using a very high acceptance solenoid assembly, is described. The muon phase space distribution is measured upstream and downstream of the focus. The muons are studied both with and without an energy absorber. The emittance of the muon ensemble is shown to decrease in the presence of an energy absorber and the phase space density is shown to increase, indicating that the beam has been successfully cooled.

Contents

1 Introduction

1.1 Ionisation Cooling

Ionization cooling [1] is the only known technique that can cool a muon beam on a timescale competitive with the muon lifetime [2] [3] [4] [5]. Muon cooling has never been demonstrated previously. In ionization cooling, a beam is passed through an absorber causing energy to be lost due to ionization of atomic electrons. This yields a reduction in normalized transverse emittance. Multiple Coulomb scattering from atoms causes an increase in angular divergence of the beam, and hence emittance growth. The change in normalized RMS emittance $\varepsilon_\perp$ in distance dz is [1]

$$\frac{d\varepsilon_\perp}{dz} \approx -\frac{\varepsilon_\perp}{\beta^2 E_\mu}\left\langle\frac{dE}{dz}\right\rangle + \frac{\beta_\perp (13.6\,\mathrm{MeV/c})^2}{2\beta^3 E_\mu m_\mu X_0} \tag{1}$$

where $\beta_\perp$ is the transverse optical Twiss function, βc, E_μ, m_μ are the particle velocity, energy and mass, and X_0 is the radiation length. There exists an equilibrium RMS emittance ε_{eqm}

$$\varepsilon_{eqm} \approx \frac{1}{2m_\mu}\frac{13.6^2}{X_0}\frac{\beta_\perp}{\beta\langle dE/dz\rangle} \tag{2}$$

at which $d\varepsilon_\perp/dz = 0$. If a beam with emittance below equilibrium is incident on an absorber, its emittance increases on passage through the absorber. Otherwise the emittance decreases. The Muon Ionisation Cooling Experiment (MICE) collaboration seek to demonstrate ionization cooling for the first time.

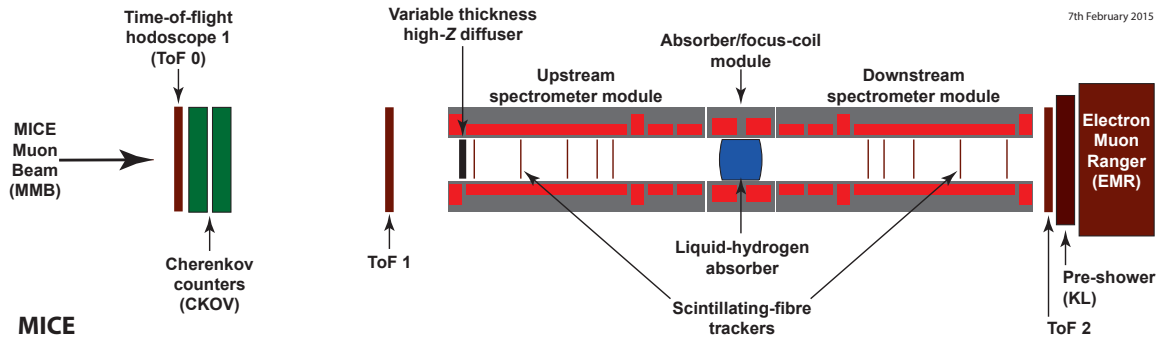## 1.2 The Muon Ionisation Cooling Experiment

Figure 1: The MICE apparatus.

MICE Step IV [6] [7] consists of a transfer line to bring particles from the ISIS synchrotron at Rutherford Appleton Laboratory to the cooling experiment. The cooling equipment consists of a section of a solenoid focussing ionization cooling cell. Detectors, placed upstream and downstream of the emittance reduction apparatus, measure the momentum, position and species of particles entering and leaving the cooling channel, enabling the measurement of change in normalized beam emittance of the ensemble. A schematic of the apparatus is shown in fig. 1.

1.3 MICE Muon Beam line

Pions are created by dipping a titanium target into the ISIS proton synchrotron. The MICE Muon Beam line is a transfer line that has been constructed to transport the resultant particles to the cooling apparatus [8] [9] [10].

The incoming particle momentum can be selected by varying the field in a pair of dipoles. Higher magnetic field selects higher particle momentum. A series of tungsten and brass irises are positioned in the transfer line, enabling the selection of different emittances for the ensemble.

Up to around 100 particles are observed per second. MICE accumulates data in runs, each run consisting of a single experimental configuration and lasting of order hours. Several runs are taken for each solenoid configuration. MICE has taken data over thousands of runs, with many different configurations.
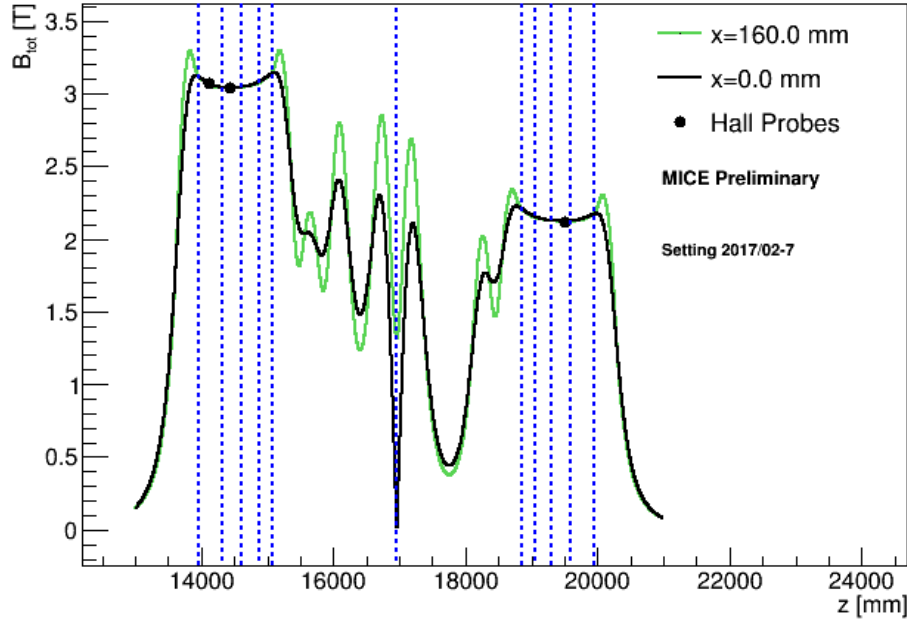

Figure 2: Modelled magnetic field for the configuration on the axis and with 160 mm horizontal displacement from the axis. The readings from Hall probes, situated 160 mm from the beam axis, are shown. Dashed lines indicate position of the tracker stations and absorber. A cusp near to the absorber position corresponds to the position of a flip in the field polarity from positive to negative.

1.4 Cooling Channel

The cooling channel consists of three superconducting solenoid modules [11] [12]. Spectrometer solenoid modules at the upstream and downstream end of the channel (SSU and SSD respectively) each generate a region of uniform field in which diagnostic trackers are situated and a matching region that transports the beam from the solenoid to the focus coil module (FC). The focus coil module, positioned between the solenoids, provides additional focussing to increase the angular divergence of the beam at the absorber, improving the amount of emittance reduction that can be achieved.

The effect of two absorbers are studied in this note, placed in the centre of the FC. The liquid hydrogen absorber is a 21 litre vessel. When filled, the absorber presents 350 mm of liquid Hydrogen along the experimental axis. Liquid hydrogen was chosen as an absorber material as it provides less multiple Coulomb scattering for a given energy loss. Containment of the Hydrogen is provided by a pair of thin Aluminium windows. An additional pair of windows provided secondary containment in case of failure of the primary containment windows.

The lithium hydride absorber is a 65 mm thick cylinder. The cylinder had a thin coating of parylene to prevent

2

ingress of water or oxygen. Configurations with no absorber installed at all and with just the liquid hydrogen containment vessel are also studied in this note.

1.5 Diagnostic Apparatus

Upstream of the cooling apparatus, two time-of-flight detectors (ToFs) [13] [14] enable the measurement of particle velocity. A complementary velocity measurement is made by a threshold Cerenkov counter [15]. Scintillating fibre trackers, positioned either side of the absorber module (TKU and TKD respectively), enable the measurement of particle position and momentum upstream and downstream of the absorber. Further downstream an additional ToF detector, a KLOE Light pre-shower detector and Electron Muon Ranger enable rejection of electron impurities.

The trackers consist of 5 stations [16] [17]. Each station consists of 3 views, each view rotated by 120° with respect to the previous view. Each view consists of 2 layers of scintillating fibres. Gangs of 7 scintillating fibres are read out together by cryogenically operated Visible Light Photon Counters, enabling the position of incident particles to be measured. The trackers are situated in uniform fields such that particles make a helical path. The magnitude of the field is measured using Hall probes situated in the region of the tracker. By measuring the radius and pitch of the helix, the momentum of the particle can be deduced. The trackers have sufficient redundancy to enable the track reconstruction to be internally validated in order to estimate the efficacy of the reconstruction.

Each ToF consists of two planes. Each ToF plane is made up of a number of scintillator slabs. Photomultiplier tubes at either end of the ToF slabs produce a signal when particles pass through the ToF. The time at which muons pass through the apparatus can be measured with a resolution of 60 ps.

1.6 Operation of the Equipment

In this paper the evolution of phase space density is reported for a single configuration of the cooling magnets, '2017-02 7'. The cooling channel magnet set currents and the beam optical parameters assuming no beta-beating in the upstream spectrometer solenoid are listed in table 1. A model of the magnetic field in this configuration is shown in fig. 2.

The MICE Muon Beam line settings were varied to mimic different beam conditions. Results from four transfer line configurations are reported, with the accumulated muon sample having nominal emittances of 3 mm, 4 mm, 6 mm and 10 mm at momenta around 140 MeV/c in the upstream spectrometer solenoid. These configurations are '3-140+M3-Test4', '4-140+M3-Test1', '6-140+M3-Test2' and '10-140+M3-Test4' henceforth denoted '3-140', '4-140', '6-140' and '10-140' respectively. The corresponding run numbers and time during which the datasets were taken are listed in table 2.

1.7 Simulation

The cooling channel was modelled using various codes. Simulated particles based on a representative model of the pion yield from the target were transported through to the downstream edge of D2 using G4Beamline [18]. Downstream of this region, MAUS [19] was used to model particle transport and the response of the MICE detectors to the incoming beam.

Some issues exist in the simulation, some of which have been eliminated by artificially tuning the simulated experiment:

3

Table 1: Magnet parameters and other information for 2017-02 7. The cooling channel was powered in flip mode, meaning that SSU and the upstream coil in FC had positive polarity while the downstream coil in FC and SSD had negative polarity.

Setting	2017-02 7
$\beta_\perp$ at absorber [mm]	660
Nominal momentum [MeV/c]	140
SSU Center Coil [A]	205.7
SSU Match Coil2 [A]	168.25
SSU Match Coil1 [A]	191.0
FC Coil [A]	129.24
SSD Match Coil2 [A]	195.72
SSD Center Coil [A]	144.0

Table 2: List of datasets for the 2017-02 7 cooling channel configuration, together with the beginning and end time of the data sets. Runs in bold have been included in the analysis; the others may be included in the future.

	Full absorber	Empty absorber	No absorber	Lithium Hydride
3-140+M3-Test4	9947 9956 9961 **9971**	10019 10025 10031 10038 10044 10049 10054 10055 10056 10057 10058 10059 10060 10061 10062 **10069** 10075	**10444** 10448 10458	10478 **10483** 10488
4-140+M3-Test1	9948 9950 9958 **9962**	10022 10028 10034 10040 10047 **10064** 10071	**10445** 10449 10453 10461	10480 **10484** 10489
6-140+M3-Test2	9949 9959 9960 9963 **9966** 9972 9976	10023 10029 10036 10042 **10051** 10066 10067 10073	**10446** 10450 10454 10459 10460 10463	10481 **10485** 10487
10-140+M3-Test4	9953 9964 9967 9969 **9970**	10024 10026 10030 10035 10037 10041 10043 10048 **10052** 10053 10065 10068 10072 10074 10077	**10447** 10451 10452 10455	10482 **10486** 10490
Start of first run End of last run	12/10/2017 12:10 15/10/2017 10:52	20/10/2017 18:18 23/10/2017 09:28	06/12/2017 19:54 08/12/2017 09:28	11/12/2017 18:02 12/12/2017 11:59

- The momentum of the incoming beam has approximately 4 % discrepancy between data and simulation. This has been tuned out of the incoming beam distributions by modifying the simulated dipole field so that the field is about 4 % higher than suggested by measurements with a hall probe.
- The ToF reconstruction of the simulation shows a mean residual of order 100 ps.
- The modelled tracker density has been tuned so that the simulated χ^2/n_{dof} distributions are consistent with data. The density was increased from the expected 1 g/cm^2 to 2 g/cm^2.
- The simulated extrapolated radial distribution of particles at the diffuser does not match the measured extrapolated distribution of particles (discussed below).

1.8 Demonstration of Ionization Cooling

This note explores the details of MICE. Because it is the first analysis to use the full MICE system, it is necessary to validate the subsystems. To this end,
- Section 2: describes the sample selection used in the rest of the analysis.
- Section 3: describes steps taken to validate the detector equipment for events within the sample outlined previously
- Section 4: describes steps taken to validate the cooling channel
- Section 5: explains the cooling measurement

2 Sample Selection

The selection of data from the reconstructed sample is detailed below.

2.1 Particle events

The MICE data acquisition system was set to trigger if ToF1 received simultaneous hits in a given slab. The trigger enables readout of the diagnostics during a short trigger window. All data acquired during this period is associated together and known as a particle event.

Signals in the same detector are associated into space points, for signals that are consistent with a particle passing through a given spatial region, and tracks, for signals that are consistent with a particle with a given momentum passing through a number of space points. The full reconstruction chain is described in [20].

2.2 Sample Selection

Particle events are selected for analysis according to a number of different criteria. Two samples are considered: the upstream sample is selected based on criteria in the upstream detector system only; the downstream sample is selected from the upstream sample, based on additional criteria in the downstream detector system.

The number of events surviving each sample selection criterion are listed for data in Tables 3, 4, 5 and 6. The number of surviving events are listed for simulation in Tables 7, 8, 9 and 10. The criteria are described in detail below. In the tables criteria are listed sequentially, in the order that the selection was made. The number of events surviving the selection and all preceding selections in the table is listed.

Table 3: The upstream reconstructed data sample is listed. Samples are listed for 3-140 and 4-140 datasets.

	2017-2.7 3-140 None	2017-2.7 3-140 lH2 empty	2017-2.7 3-140 lH2 full	2017-2.7 3-140 LiH	2017-2.7 4-140 None	2017-2.7 4-140 lH2 empty	2017-2.7 4-140 lH2 full	2017-2.7 4-140 LiH
All Events	258683	172444	183035	240396	268081	217469	75102	218161
One space point in ToF1	249235	166313	177064	231587	259651	210480	73147	211032
One space point in ToF0	196955	133090	146186	183288	205023	164195	60699	163990
One track in TKU	74535	50901	56195	69895	140549	113793	41107	113726
TKU χ^2/dof	67654	46157	50464	63252	126403	101857	36187	102054
TKU fiducial volume	67282	45926	50165	62934	125951	101529	36051	101703
$t_{ToF1} - t_{ToF0}$	39747	26920	28670	37505	78880	62821	22459	63222
TKU momentum	14475	9548	9987	13143	32808	26233	9291	26562
Successful extrapolation to ToF0	14473	9547	9981	13142	32798	26217	9275	26530
Diffuser aperture cut	13940	9317	9752	12703	32012	25728	9088	25936
Upstream Sample	13940	9317	9752	12703	32012	25728	9088	25936

Table 4: The upstream reconstructed data sample is listed. Samples are listed for 6-140 and 10-140 datasets.

	2017-2.7 6-140 None	2017-2.7 6-140 lH2 empty	2017-2.7 6-140 lH2 full	2017-2.7 6-140 LiH	2017-2.7 10-140 None	2017-2.7 10-140 lH2 empty	2017-2.7 10-140 lH2 full	2017-2.7 10-140 LiH
All Events	258972	177328	283405	307300	398000	209994	374910	479187
One space point in ToF1	250774	171124	275269	296958	376486	196606	356829	448579
One space point in ToF0	198333	132548	226008	229741	287657	144999	281242	331756
One track in TKU	134951	90985	151587	158194	151577	76646	146733	176111
TKU χ^2/dof	120532	80629	131917	140694	135293	68248	128669	157056
TKU fiducial volume	119939	80227	131247	140059	129260	65159	122803	150219
$t_{ToF1} - t_{ToF0}$	77702	51148	85624	90183	85564	42666	84236	97156
TKU momentum	30987	20428	33700	35411	25371	12545	24512	28468
Successful extrapolation to ToF0	30959	20396	33553	35274	24903	12226	22905	26900
Diffuser aperture cut	30320	20027	32943	34613	20403	10027	19234	22516
Upstream Sample	30320	20027	32943	34613	20403	10027	19234	22516

8

Table 5: The downstream reconstructed data sample is listed. Samples are listed for 3-140 and 4-140 datasets.

	2017-2.7 3-140 None	2017-2.7 3-140 lH2 empty	2017-2.7 3-140 lH2 full	2017-2.7 3-140 LiH	2017-2.7 4-140 None	2017-2.7 4-140 lH2 empty	2017-2.7 4-140 lH2 full	2017-2.7 4-140 LiH
Upstream Sample	13940	9317	9752	12703	32012	25728	9088	25936
One track in TKD	13722	9112	9421	12413	31040	24720	8717	24927
TKD χ^2/dof	13208	8791	9113	12008	30041	23982	8472	24172
TKD fiducial volume	13135	8703	8893	11731	29347	23380	8207	23482
TKD momentum	12945	8598	8838	11641	29028	23143	8146	23345
Downstream Sample	12945	8598	8838	11641	29028	23143	8146	23345

Table 6: The downstream reconstructed data sample is listed. Samples are listed for 6-140 and 10-140 datasets.

	2017-2.7 6-140 None	2017-2.7 6-140 lH2 empty	2017-2.7 6-140 lH2 full	2017-2.7 6-140 LiH	2017-2.7 10-140 None	2017-2.7 10-140 lH2 empty	2017-2.7 10-140 lH2 full	2017-2.7 10-140 LiH
Upstream Sample	30320	20027	32943	34613	20403	10027	19234	22516
One track in TKD	28358	18603	30718	32458	15696	7666	15380	17857
TKD χ^2/dof	27293	17975	29763	31420	15069	7376	14873	17268
TKD fiducial volume	25969	17024	28626	30157	13099	6484	13519	15524
TKD momentum	25727	16864	28459	30013	12971	6430	13461	15462
Downstream Sample	25727	16864	28459	30013	12971	6430	13461	15462

Table 7: The upstream reconstructed simulated sample is listed. Samples are listed for 3-140 and 4-140 datasets.

	Simulated 2017-2.7 3-140 None	Simulated 2017-2.7 3-140 lH2 empty	Simulated 2017-2.7 3-140 lH2 full	Simulated 2017-2.7 3-140 LiH	Simulated 2017-2.7 4-140 None	Simulated 2017-2.7 4-140 lH2 empty	Simulated 2017-2.7 4-140 lH2 full	Simulated 2017-2.7 4-140 LiH
All Events	159538	159322	159498	159950	201380	19237	201563	201596
One space point in ToF1	141035	141130	141065	141655	181394	17388	181956	181798
One space point in ToF0	131638	131559	131411	131966	169328	16258	169852	169573
One track in TKU	57449	64155	57118	57566	120987	11617	122058	121826
TKU χ^2/dof	51367	57960	51027	51448	109085	10471	109335	109429
TKU fiducial volume	48540	56027	48180	48721	107977	10377	108222	108362
$t_{ToF1} - t_{ToF0}$	27503	33335	27352	27652	59105	5666	59271	59397
TKU momentum	9585	10539	9460	9577	20649	1862	20979	20916
Successful extrapolation to ToF0	9582	10519	9453	9571	20645	1860	20922	20848
Diffuser aperture cut	9351	9980	9263	9363	19680	1783	19986	19956
Upstream Sample	9351	9980	9263	9363	19680	1783	19986	19956

Table 8: The upstream reconstructed simulated sample is listed. Samples are listed for 6-140 and 10-140 datasets.

	Simulated 2017-2.7 6-140 None	Simulated 2017-2.7 6-140 lH2 empty	Simulated 2017-2.7 6-140 lH2 full	Simulated 2017-2.7 6-140 LiH	Simulated 2017-2.7 10-140 None	Simulated 2017-2.7 10-140 lH2 empty	Simulated 2017-2.7 10-140 lH2 full	Simulated 2017-2.7 10-140 LiH
All Events	211422	20294	211174	211571	296971	28407	297111	298029
One space point in ToF1	190904	18330	190842	191258	268252	25632	268550	269256
One space point in ToF0	178199	17029	178120	178573	251126	23915	251552	251994
One track in TKU	118921	11852	118688	119820	142143	12920	142204	143264
TKU χ^2/dof	105790	10478	104687	105813	127313	11579	127069	128045
TKU fiducial volume	103775	10310	102637	103692	108707	10118	108693	109849
$t_{ToF1} - t_{ToF0}$	57928	5938	57627	58008	64554	6131	64627	65161
TKU momentum	21072	2111	21065	21276	16545	1403	16546	16777
Successful extrapolation to ToF0	21035	2104	20970	21165	15786	1351	14721	15110
Diffuser aperture cut	20498	1955	20577	20738	12513	1068	12327	12473
Upstream Sample	20498	1955	20577	20738	12513	1068	12327	12473

Table 9: The downstream reconstructed simulated sample is listed. Samples are listed for 3-140 and 4-140 datasets.

	Simulated 2017-2.7 3-140 None	Simulated 2017-2.7 3-140 lH2 empty	Simulated 2017-2.7 3-140 lH2 full	Simulated 2017-2.7 3-140 LiH	Simulated 2017-2.7 4-140 None	Simulated 2017-2.7 4-140 lH2 empty	Simulated 2017-2.7 4-140 lH2 full	Simulated 2017-2.7 4-140 LiH
Upstream Sample	9351	9980	9263	9363	19680	1783	19986	19956
One track in TKD	9038	9700	8854	8996	18902	1721	19049	19135
TKD χ^2/dof	8762	9406	8615	8733	18454	1674	18621	18675
TKD fiducial volume	8714	9304	8484	8587	18109	1639	18280	18220
TKD momentum	8543	9103	8382	8481	17915	1617	18121	18111
Downstream Sample	8543	9103	8382	8481	17915	1617	18121	18111

Table 10: The downstream reconstructed simulated sample is listed. Samples are listed for 6-140 and 10-140 datasets.

	Simulated 2017-2.7 6-140 None	Simulated 2017-2.7 6-140 lH2 empty	Simulated 2017-2.7 6-140 lH2 full	Simulated 2017-2.7 6-140 LiH	Simulated 2017-2.7 10-140 None	Simulated 2017-2.7 10-140 lH2 empty	Simulated 2017-2.7 10-140 lH2 full	Simulated 2017-2.7 10-140 LiH
Upstream Sample	20498	1955	20577	20738	12513	1068	12327	12473
One track in TKD	18651	1724	18772	18944	9306	802	9521	9638
TKD χ^2/dof	18102	1673	18363	18423	9031	777	9300	9397
TKD fiducial volume	17046	1565	17637	17680	7960	677	8518	8586
TKD momentum	16809	1539	17490	17549	7856	667	8422	8517
Downstream Sample	16809	1539	17490	17549	7856	667	8422	8517

Table 11: Upper and lower bound of ToF cuts for different beamline settings.

Beamline	Lower Bound [ns]	Upper Bound [ns]
3-140	1.5	6.5
4-140	1.5	6.0
6-140	1.5	5.5
10-140	1.5	4.5

2.3 Upstream Sample

Cuts applied to the upstream sample are described below.

- One ToF1 Space Point: Events have exactly one space point reconstructed in ToF1. The number of space points per event observed in ToF1 is shown in fig. 3.
- One ToF0 Space Point: Events have exactly one space point reconstructed in ToF0. The number of space points per event observed in ToF1 is shown in fig. 4.
- One TKU Track: Events have exactly one track reconstructed in TKU. The number of tracks observed in TKU is shown in fig. 5.
- TKU χ^2 per degree of freedom: The reconstructed χ^2 per degree of freedom in TKU is required to be less than 4. The χ^2 per degree of freedom of events in each sample is shown in fig. 6.
- TKU fiducial cut: Events are required to have a maximum radial excursion from the axis in TKU less than 150 mm. The maximum radial excursion of the track is estimated assuming a helical trajectory between tracker stations. The maximum radial excursion of events in each sample is shown in fig. 7.
- ToF01 Time: Pions and electrons in the momentum selection described above have a quite different time-of-flight between ToF0 and ToF1 to muons. Events are required to have time-of-flight between ToF0 and ToF1 consistent with a muon in order to reject this background. The time-of-flight of events in each sample is shown in fig. 8. The velocity of particles upstream of the diffuser is faster for thicker diffuser settings, in order to yield a muon sample with momentum peaked around 140 MeV/c in TKU. In order to correctly reject impurities, the ToF01 cut is different for different beamline settings, as listed in table 11
- TKU Momentum: Events are required to have momentum reconstructed by TKU between 135 and 145 MeV/c. The momentum of events in each sample is shown in fig. 9.
- Successful extrapolation to ToF0: Those events that are not successfully extrpolated from TKU to ToF0 are rejected.
- Diffuser aperture cut: Those events that have radius greater than 100 mm at either the upstream or downstream face of the diffuser are rejected. The distribution of extrapolated radii are shown in fig. 10 and fig. 11 for upstream and downstream faces of the diffuser respectively.

Events which do not meet these criteria are not considered for analysis at all.

2.3.1 Diffuser Geometry

The anomaly between MC and data in diffuser radius is noted in fig. 10 and fig. 11. The physical layout of the diffusers and support structure has been studied in a reasonable amount of detail and checked to be consistent with the geometry implemented in MAUS. The discrepancy still exists. It is noted that the discrepancy is in the region outside the upstream sample cut.
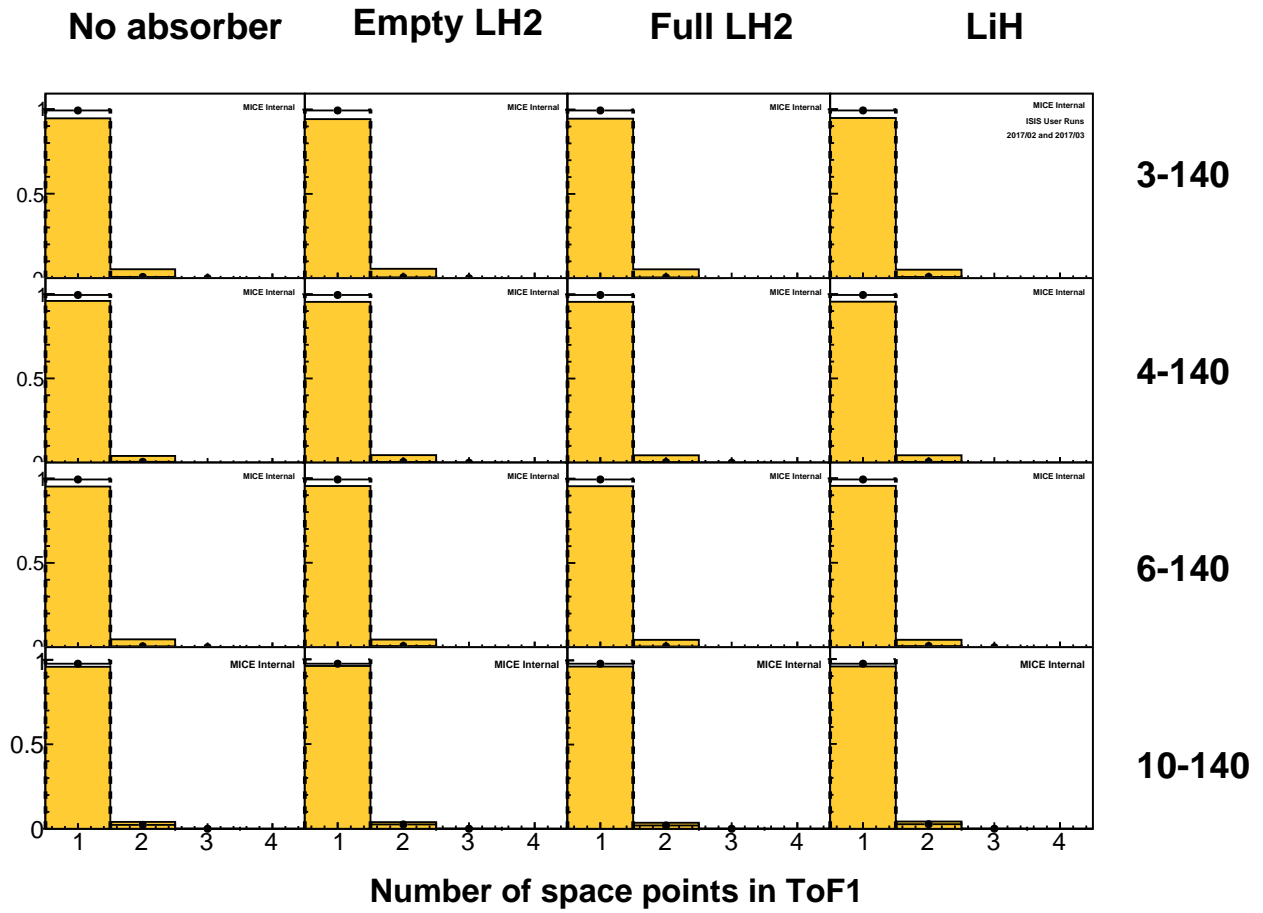
Figure 3: The number of ToF1 space points for events that are accepted by every cut except the requirement that there is 1 ToF1 space point.
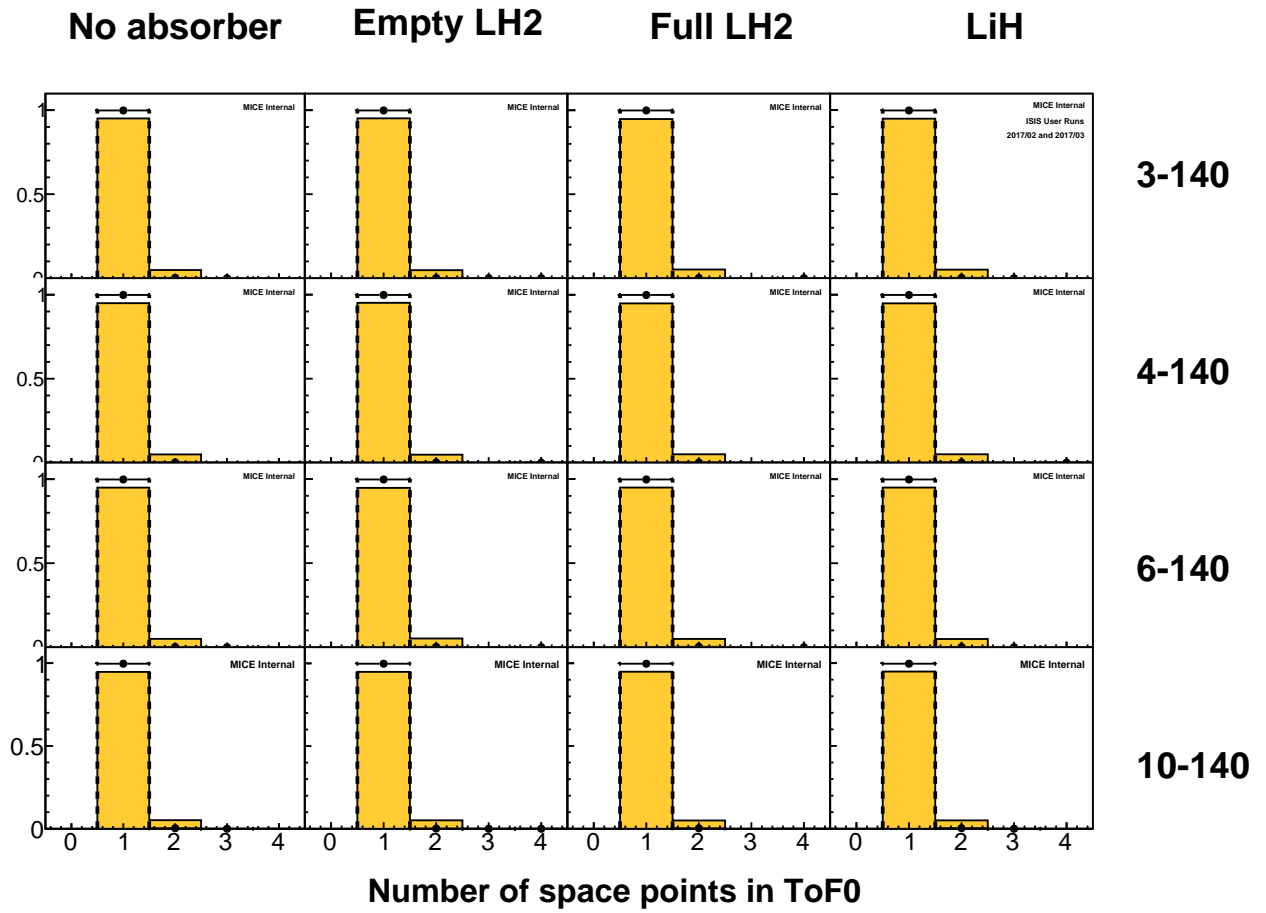
Figure 4: The number of ToF0 space points for events that are accepted by every cut except the requirement that there is 1 ToF0 space point.
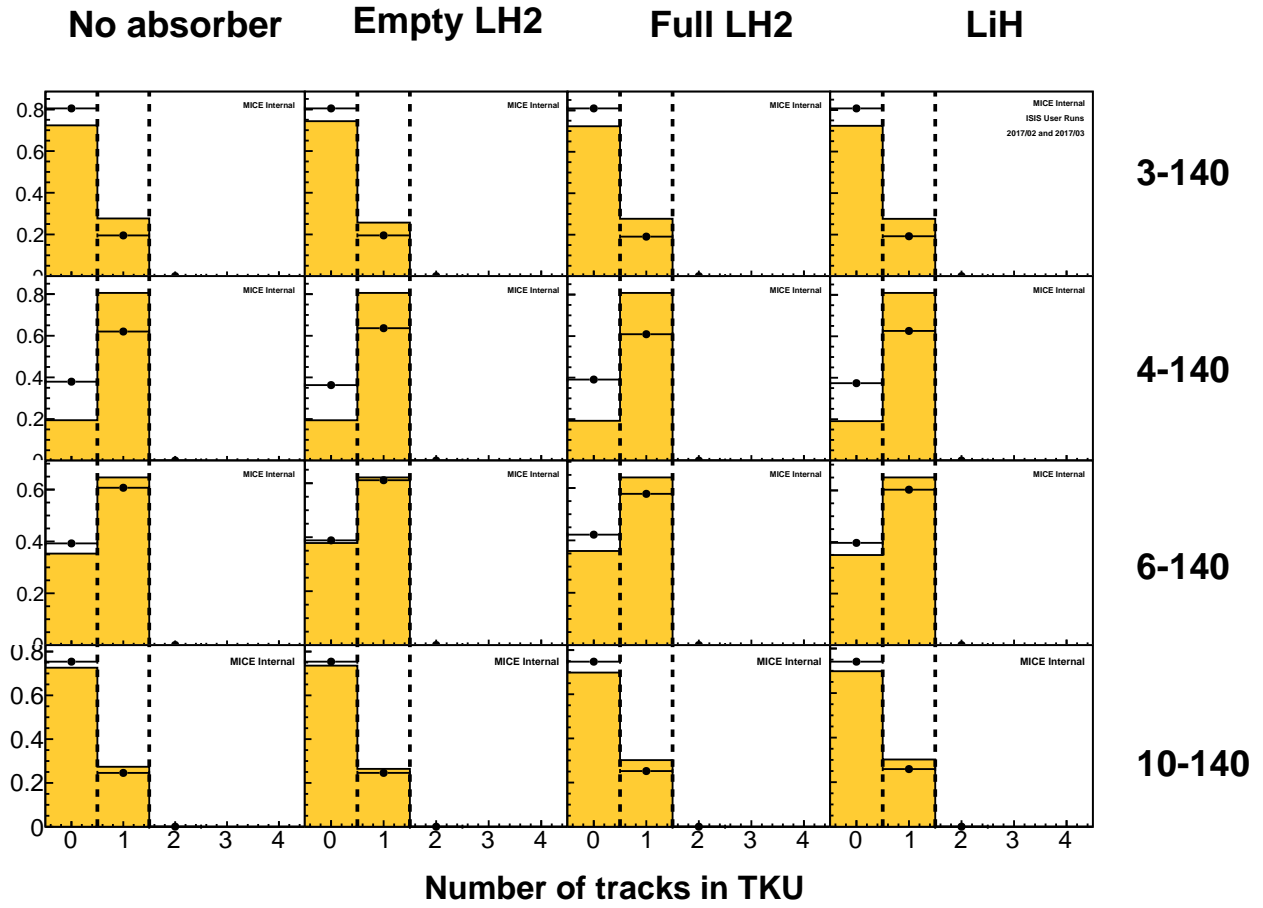
Figure 5: The number of tracks in TKU for events that are accepted by every upstream cut except the requirement that there is 1 TKU track.
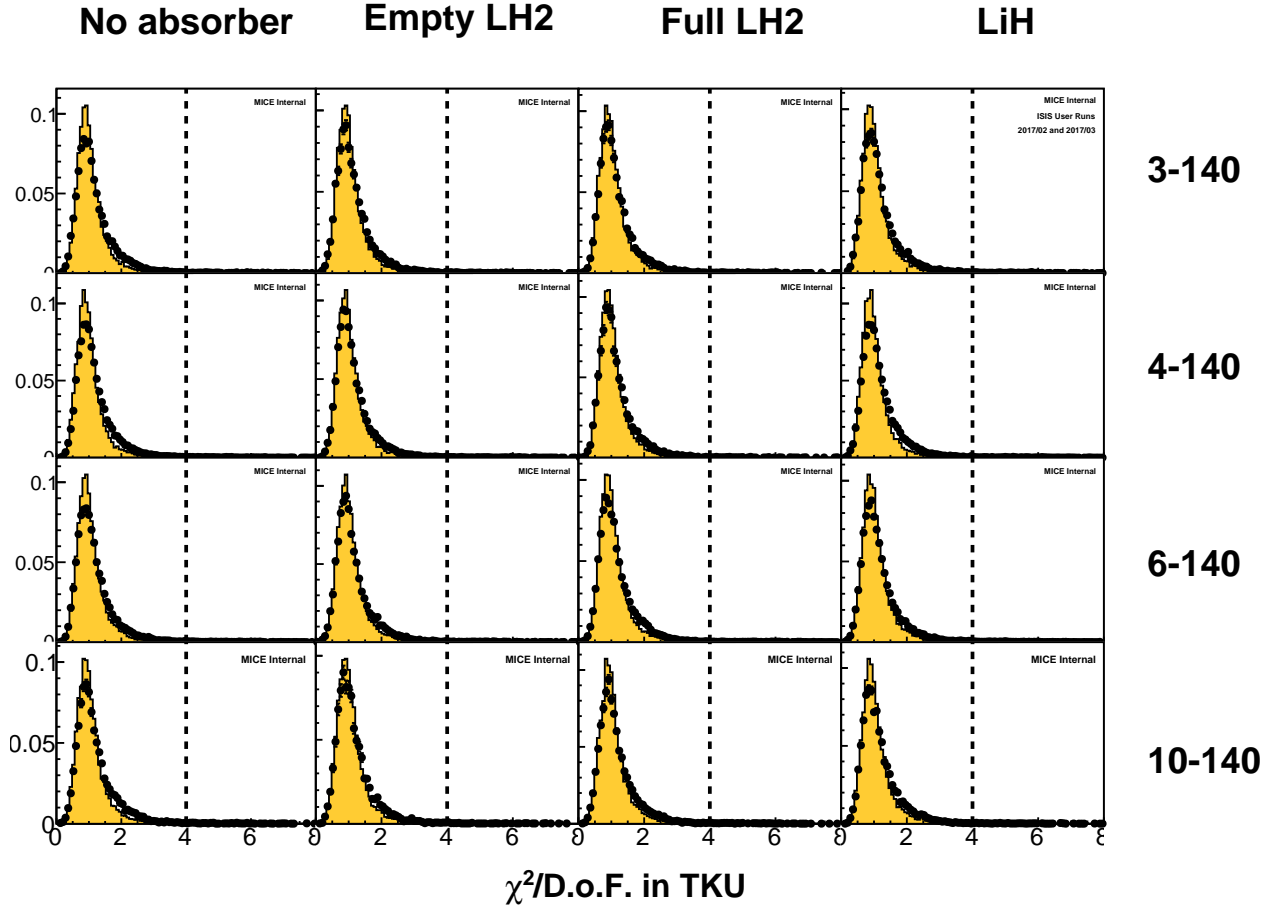
Figure 6: χ^2 per degree of freedom distribution in TKU for events that are accepted by every upstream cut except the requirement on TKU χ^2 per degree of freedom.
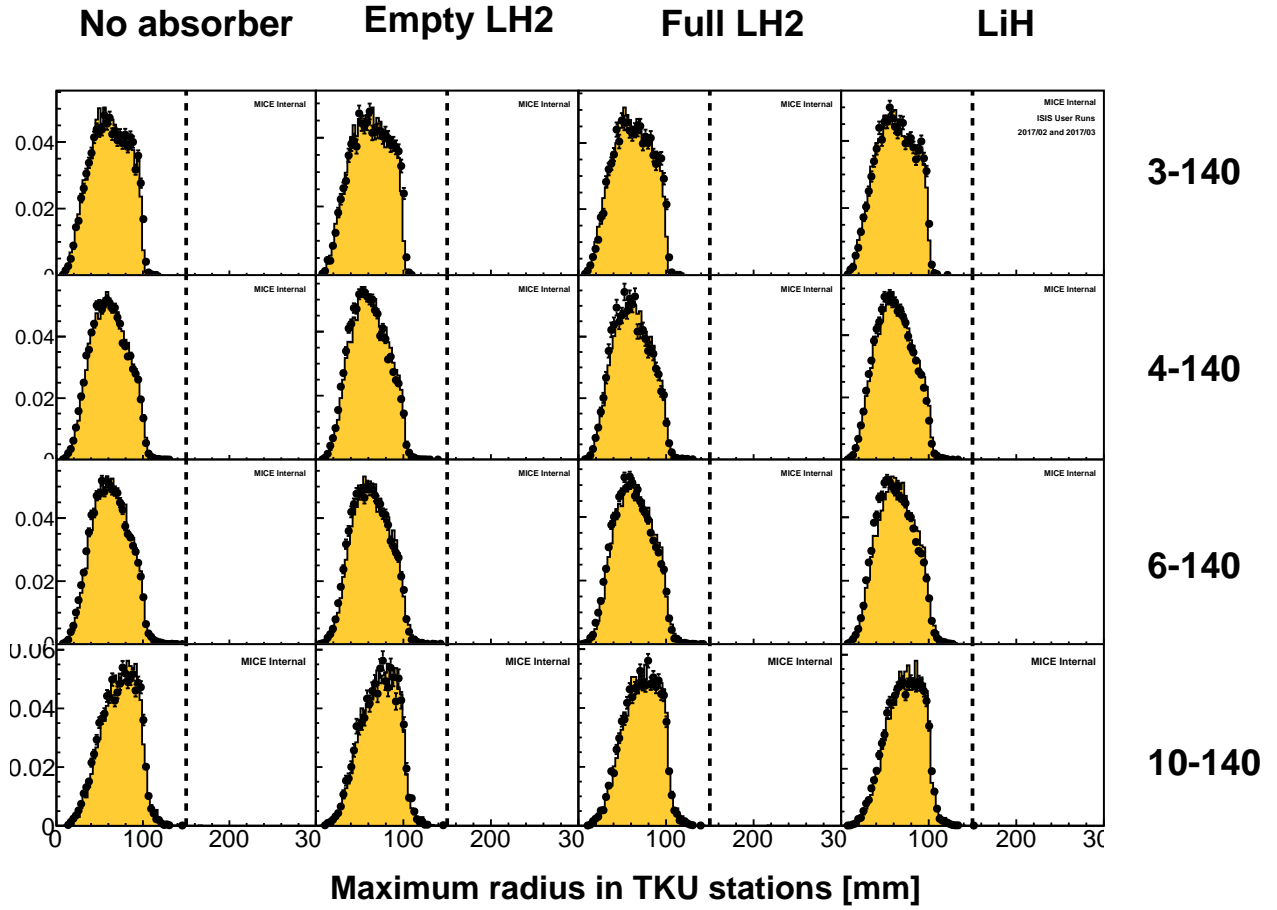
Figure 7: Maximum radius in TKU for events that are accepted by every cut except the maximum radius requirement.
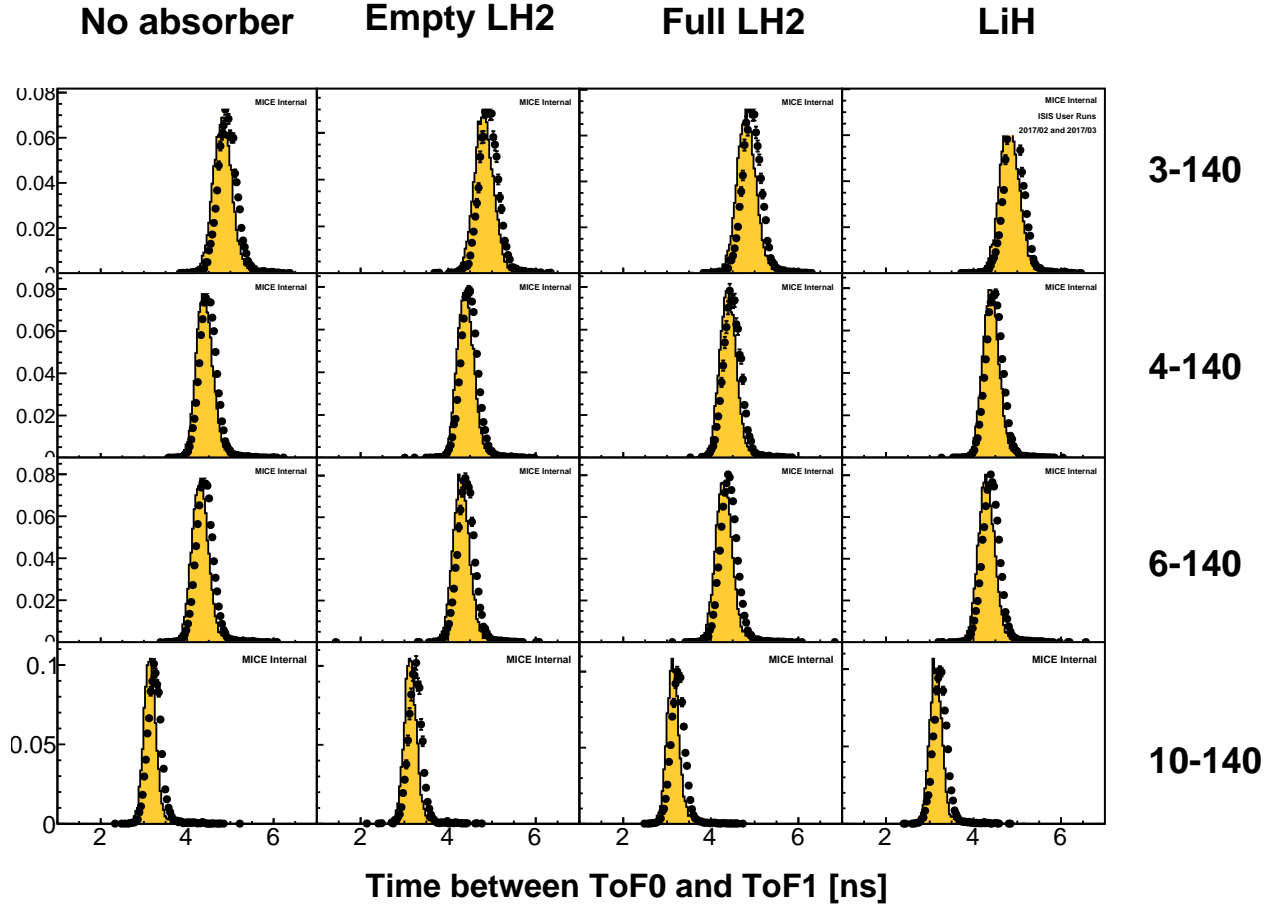
Figure 8: Time-of-flight measured between ToF0 and ToF1 for events that are accepted by every upstream cut except for the time-of-flight cuts.
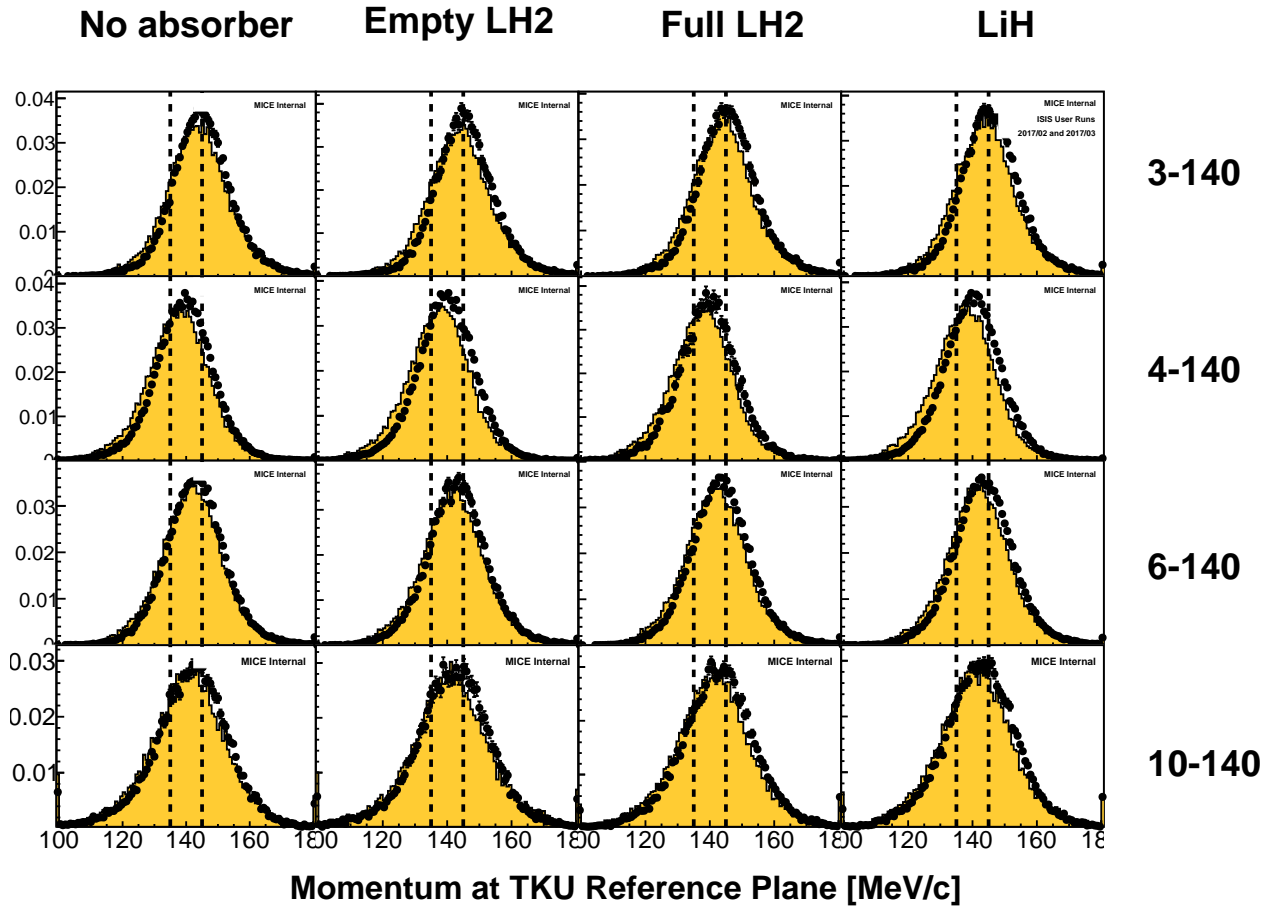
Figure 9: Momentum measured by TKU for events that are accepted by every upstream cut except for the TKU momentum cut.

No absorber **Empty LH2** **Full LH2** **LiH**

3-140

4-140

6-140

10-140

Radius at diffuser (downstream) [mm]
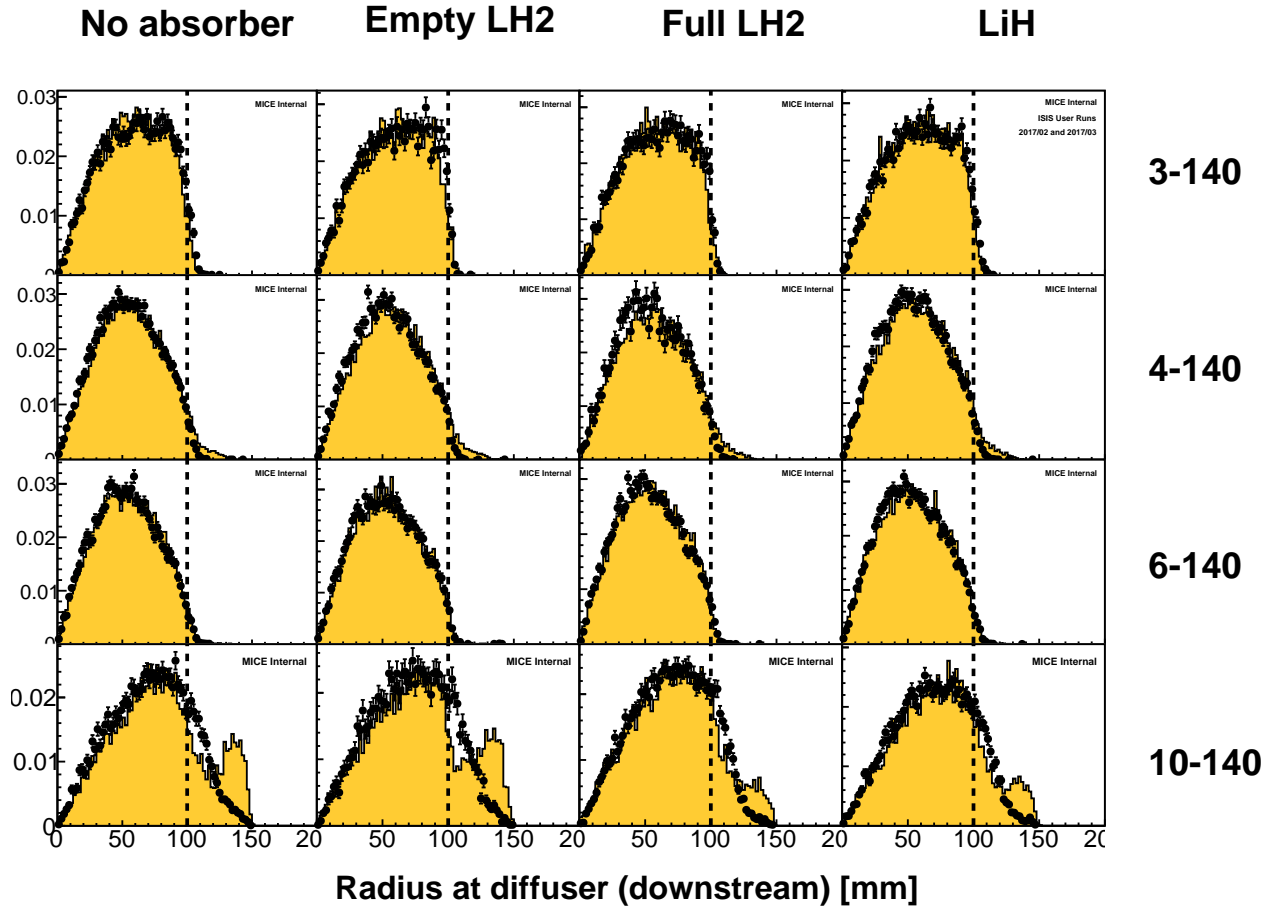
Figure 10: Extrapolated radius of tracks at the upstream face of the diffuser for events that are accepted by every upstream cut except for the diffuser radius cut. BUG: 10-140 MC issue.
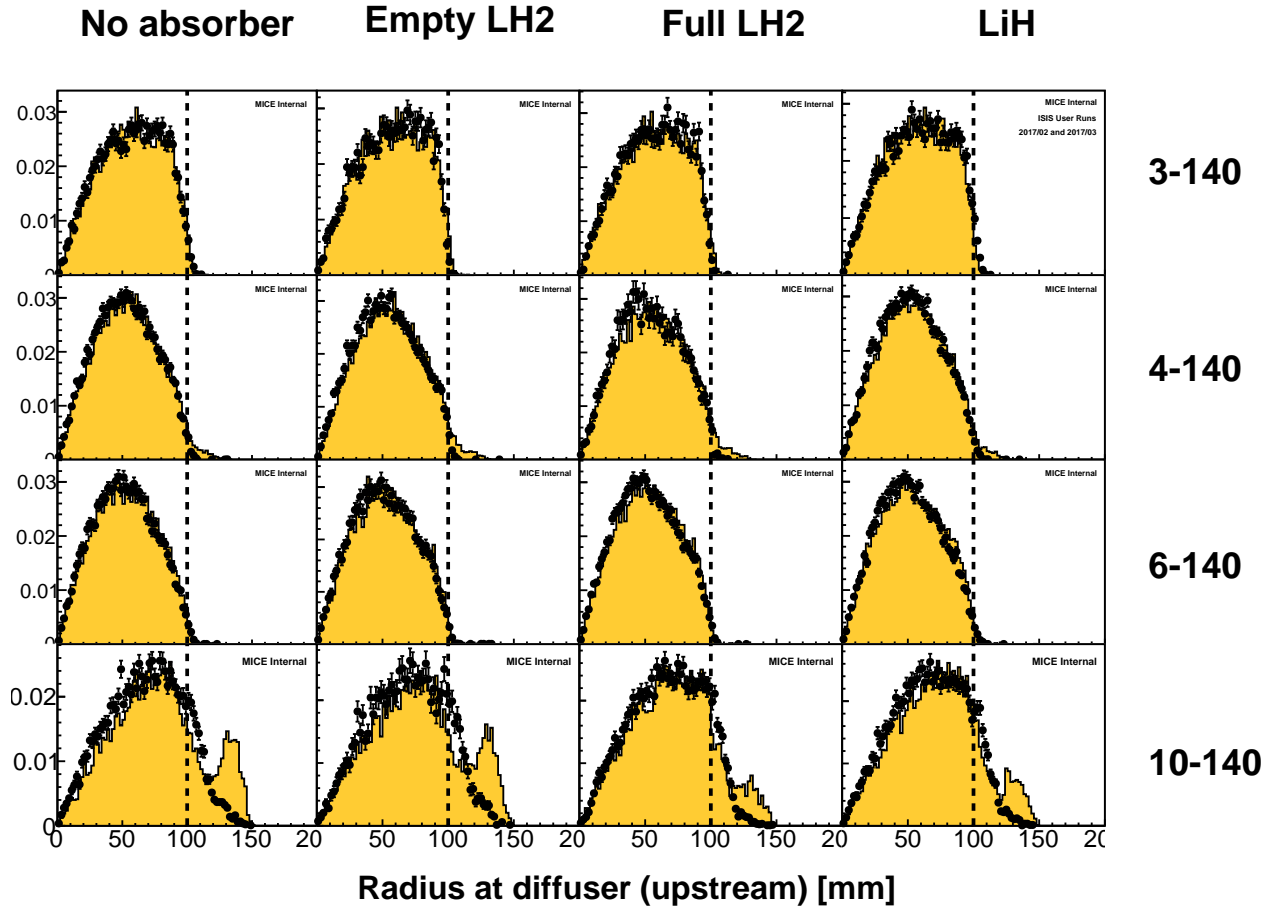
Figure 11: Extrapolated radius of tracks at the upstream face of the diffuser for events that are accepted by every upstream cut except for the diffuser radius cut. BUG: 10-140 MC issue.

24

2.4 Downstream Sample

Cuts applied to the downstream sample are described below.

- In Upstream Sample: Events are required to be in the upstream sample to be considered in the downstream sample.
- One TKD Track: Events have exactly one track reconstructed in TKD. The number of tracks in TKD for each event is shown in fig. 12.
- TKD χ^2 per degree of freedom: The reconstructed χ^2 per degree of freedom in TKD is required to be less than 4. The χ^2 per degree of freedom of events in each sample in TKD is shown in fig. 13.
- TKD Fiducial Volume: Events are required to have a maximum radial excursion from the axis in TKD less than 150 mm. The maximum radial excursion of the track is estimated assuming a helical trajectory between tracker stations. The maximum radial excursion of events in each sample is shown in fig. 14.
- TKD Momentum: Events are required to have reconstructed momentum between 90 and 170 MeV/c. The momentum as reconstructed by TKD of events in each sample is shown in fig. 15
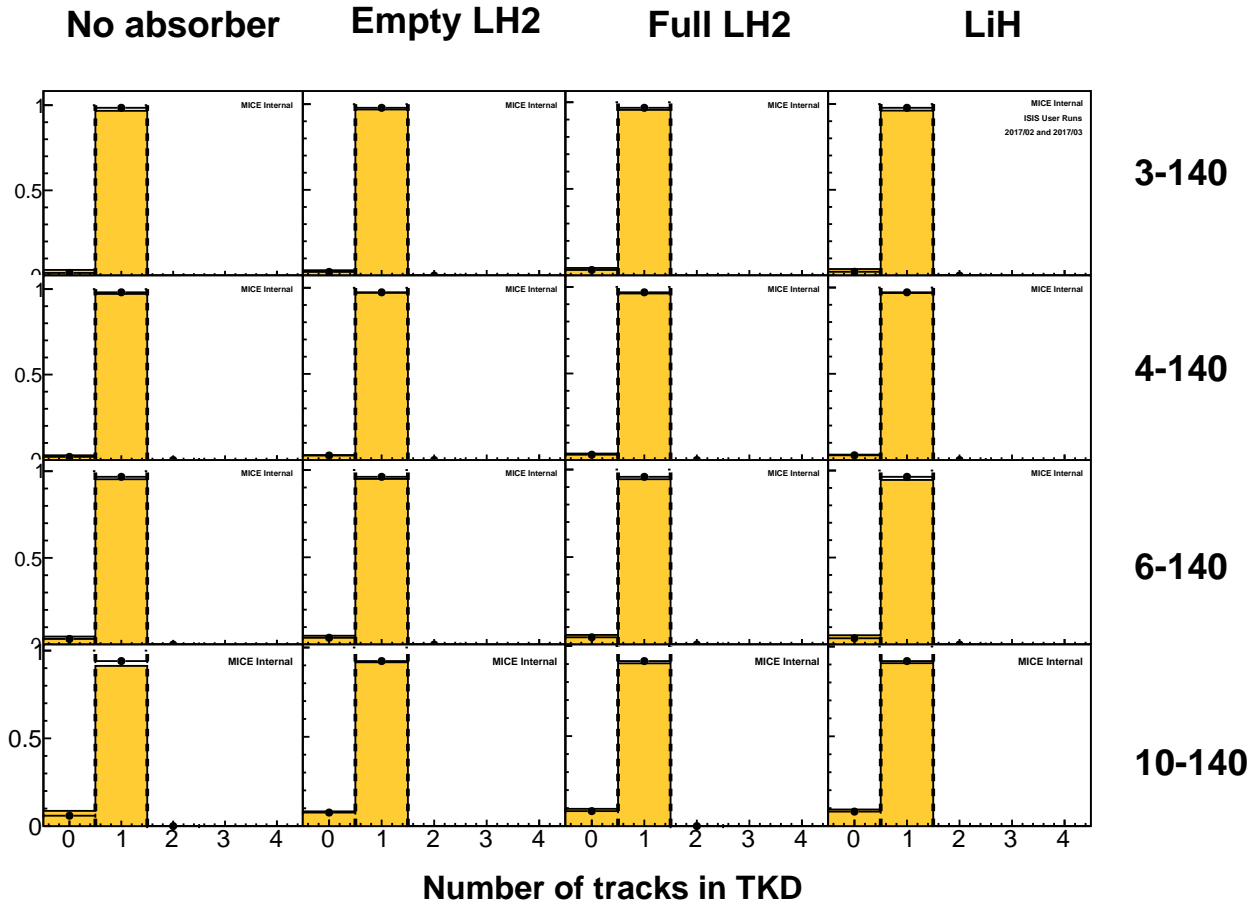
Figure 12: The number of tracks measured in TKD for events that are accepted by every cut except the requirement that there is 1 TKD track.

Events which do not meet these downstream sample criteria are not considered for analysis in the downstream region. They may either have collided with the cooling channel aperture and been lost (scraping), or they may
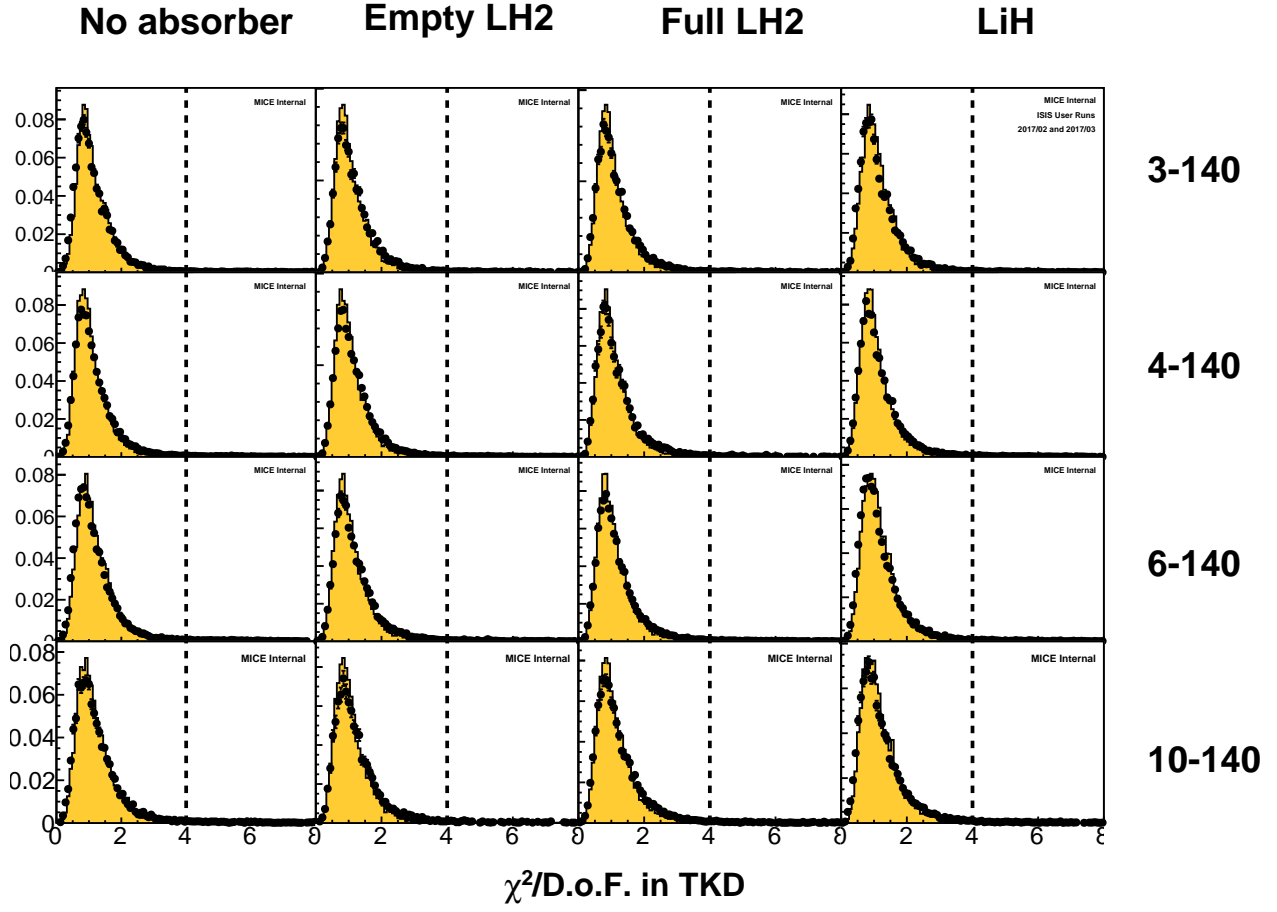
Figure 13: χ^2 distribution in TKD for events that are accepted by every cut except the requirement on χ^2.

have been not observed by the detectors (inefficiency). Systematic correction due to detector inefficiency and the associated uncertainty is discussed in Section 5.1.4.
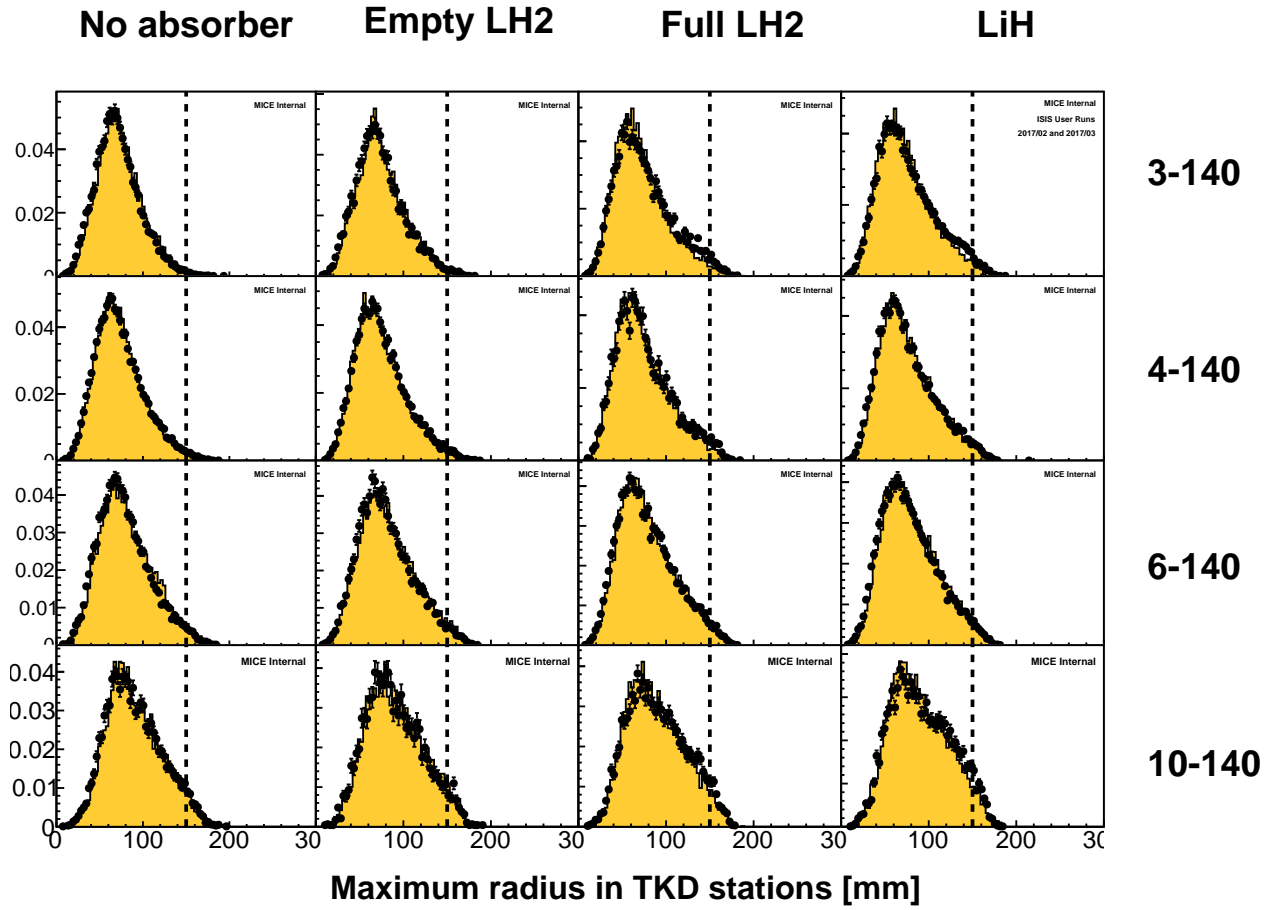
Figure 14: Maximum radius of tracks in TKD for events that are accepted by every cut except the requirement on maximum radius.
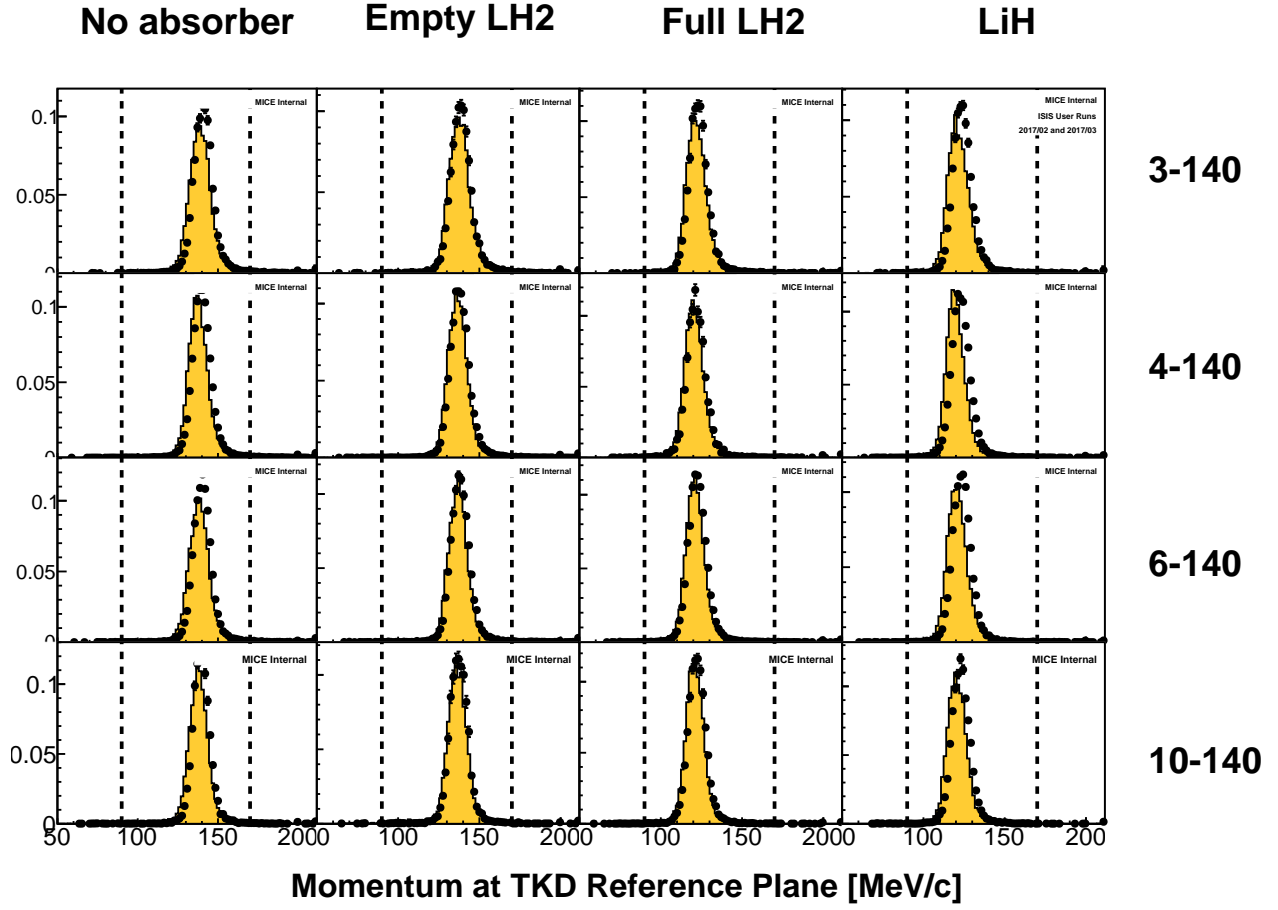
Figure 15: Momentum in TKD, for events that are accepted by every downstream cut except the TKD momentum requirement track.

Table 12: The "as designed" axial and azimuthal position of hall probes is listed.

Hall Probe	Axial position [mm]	Azimuthal position [$^\circ$]
SSU HP 77	14104	30
SSU HP 79	14429	270
SSU HP 65	14429	30
SSU HP 67	15286	150
SSD HP 66	18625	210
SSD HP 72	19482	330

3 Detectors

In this section, the resolution and efficiency of the detector systems is discussed. The reconstruction is validated both internally within each detector system, using the detector's internal redundancy, and by extrapolating reconstructed events between detectors.

3.1 Tracker

Two trackers, made up of five stations each with three planes of scintillating fibres are used to reconstruct the momentum of incoming particles. Particles make helical trajectories whose radius and wavelength vary according to the transverse and longitudinal momentum respectively. The radius of the helix is given approximately by

$$r = \frac{p_t}{qB_z} \tag{3}$$

and the wavenumber by

$$k = \frac{qB_z}{p_z}. \tag{4}$$

Fitting is performed in several steps. Electronics signals arising from adjacent fibres are collected into clusters. The position of clusters in adjacent planes are collected to form a space point. A first-pass fit of a perfect helix to the space points, pattern recognition, is used for noise rejection and to seed a second-pass fit using a Kalman filter. Tracks that do not fit a helix but successfully fit a straight line are seeded using the time-of-flight between ToF0 and ToF1 to estimate momentum.

The trackers are the main detectors used in this analysis. The efficacy of the trackers is discussed below.

3.1.1 Resolution

In the first instance, the correct operation of the tracker is studied by examining the quality of the fitted tracks and comparing the measured magnetic field with the field assumed during reconstruction.

If the reconstruction is well-understood, the path of the reconstructed trajectories should match the position of the clusters. The χ^2 distribution per degree of freedom of reconstructed tracks was shown in fig. 6 and 13 for the upstream and downstream detectors respectively.

In order to accurately reconstruct tracks the field must be well known. If the modelled field used in reconstruction differs from the actual field, a helix can be found but the reconstructed longitudinal and transverse momenta will scale with the field according to eq. (3) and eq. (4). In order to accurately reconstruct the field correctly it is essential to understand the field accurately in the measurement region.
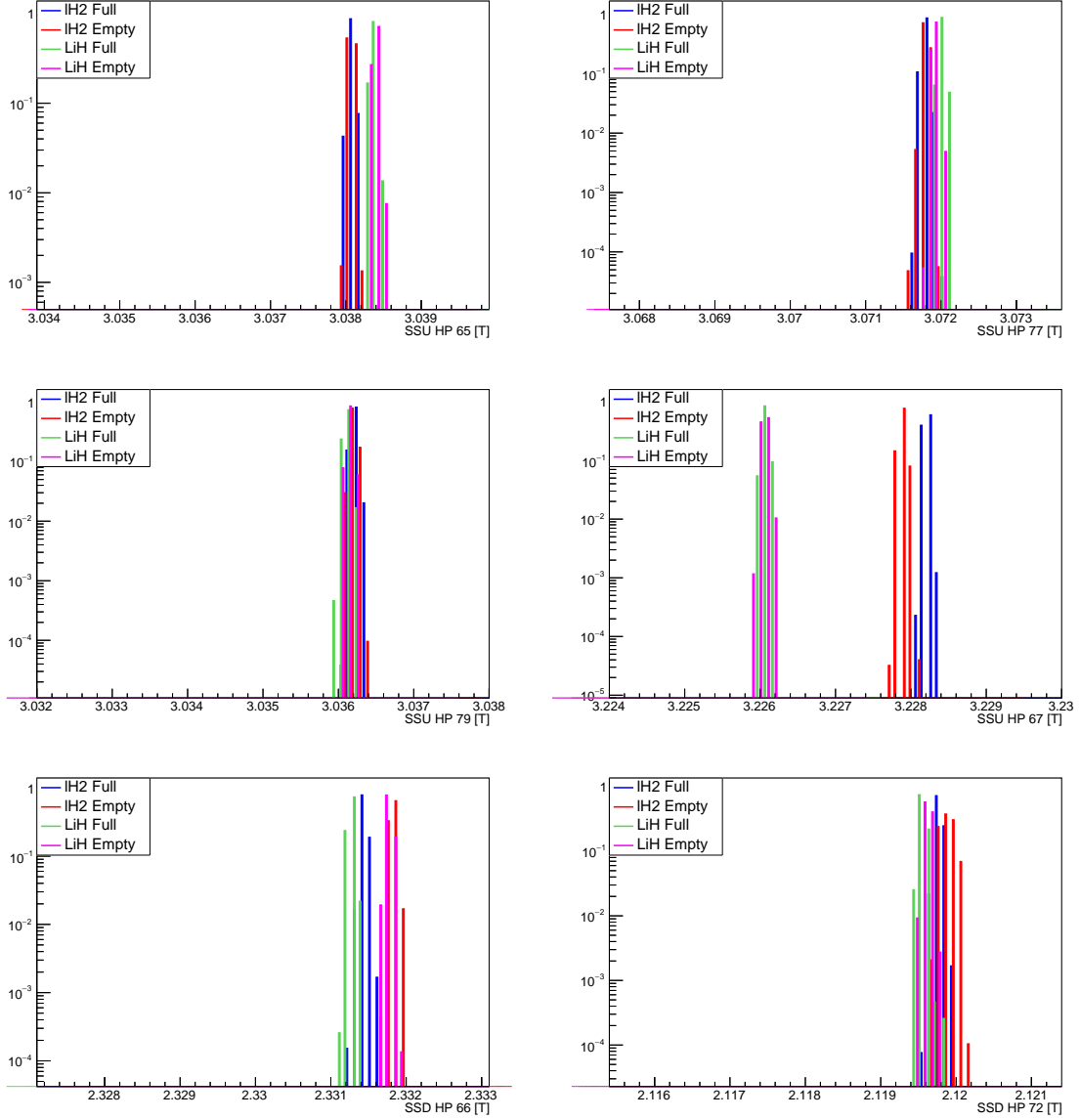
Figure 16: Hall probe readings for the four datasets across the entire period where data was taken.

The field in the tracker region was monitored during the data taking period by several Hall probes. The Hall probe measurement in the tracker region is shown in fig. 16 for the data taking periods under study in this paper. Reproducibility is demonstrated at around the 10^{-3} T level for HP67 and around 10^{-4} T level for the other hall probes. The design position of the Hall probes is listed in table 12. HP67 and HP66 were both dislocated from their design position during installation and so the actual position is uncertain. They are included here for reference only.

The measured fields are shown overlayed with the modelled field in the tracker region in fig. 17. The SSU and SSD coil currents have been tuned so that the modelled field agrees with the measured field, and this tuned field is used for simulation and reconstruction.

The simulated resolutions for TKU and TKD are shown in fig. 18 and 19 respectively. A small systematic bias is noted in the momentum reconstruction. The asymmetry can arise due to the intrinsic angular momentum of the beam or a simulated misalignment of the detector and field. Significant tails are apparent in the p_z residual. Low transverse momentum tracks are challenging to reconstruct. The tails are longer in TKD, where the field
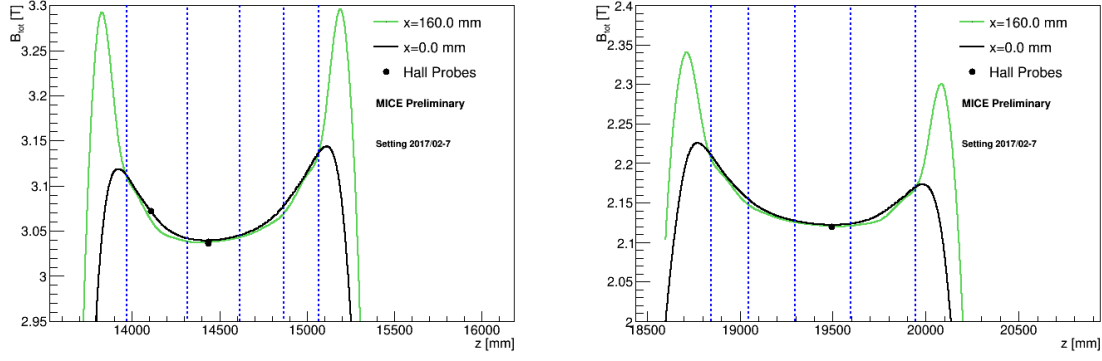
Figure 17: Hall probe readings compared to the field model used for reconstruction and track extrapolation. Blue dashed lines show the position of the tracker stations.

is 2 T rather than 3 T as in TKU.

3.1.2 Inefficiency and Impurity

The efficiency of track-finding can be studied. This analysis will count the change in the number of events in different bins in amplitude. Impurity can lead to an overestimation of the number of events in a bin. Inefficiency can lead to an underestimation of the number of events in a bin. Because the sample is defined according to events measured in the upstream tracker, only inefficiency in the downstream tracker contributes to uncertainties in this analysis. Impurity in both trackers can contribute to uncertainties.

The inefficiency can be estimated by studying the response in detectors other than the tracker and comparing this with the tracker response. The number of clusters in events contained within the upstream sample, not making a TKD track but making exactly one ToF2 space point is shown in fig. 20. These tracks are candidates for reconstruction inefficiency; they may be real particles that did not make a track, for example due to excess scattering leading to a rejection by the pattern recognition phase of the reconstruction.

Impurity can arise due to noise in the tracker readout, leading to clusters and even tracks that are not associated with a particle. The magnitude can be estimated in TKU by studying the number of planes that register at least one cluster in events that pass the ToF01 cuts but did not make a TKU track. By observing the amount of noise in the tracker, one can infer the number of impure tracks. The distribution of noise for these events is shown in fig. 21. There are a few events with 1 or 2 clusters, but there is not enough noise to contribute significantly to track construction.

The magnitude can be estimated similarly in TKD by studying the number of clusters in events that pass the upstream cuts but did not make a TKD track or a ToF2 space point. These events are expected to correspond to events where no particle traversed the detector. This is shown in 22. There is a clear separation between the peak corresponding to noise events (< 4 clusters) and the peak corresponding to real tracks.

There is a significant discrepancy between the simulated distribution of clusters and the measured distribution of clusters. This is not expected to effect the simulated inefficiency significantly as the dominant source of inefficiency arises due to processes like scattering in the detector planes deforming the muon helix and causing pattern recognition to fail.

The resultant inefficiency of TKD is shown as a function of phase space in Fig. 23, 24, 25 and 26, calculated using eq 11. At low p_t track reconstruction is challenging because scattering in the tracker stations is dominant over curvature due to the magnetic field. Where this is the case, no p_z can be reconstructed and the tracks are rejected. Additional inefficiency is observed at large amplitudes. This may arise due to deformation of the track
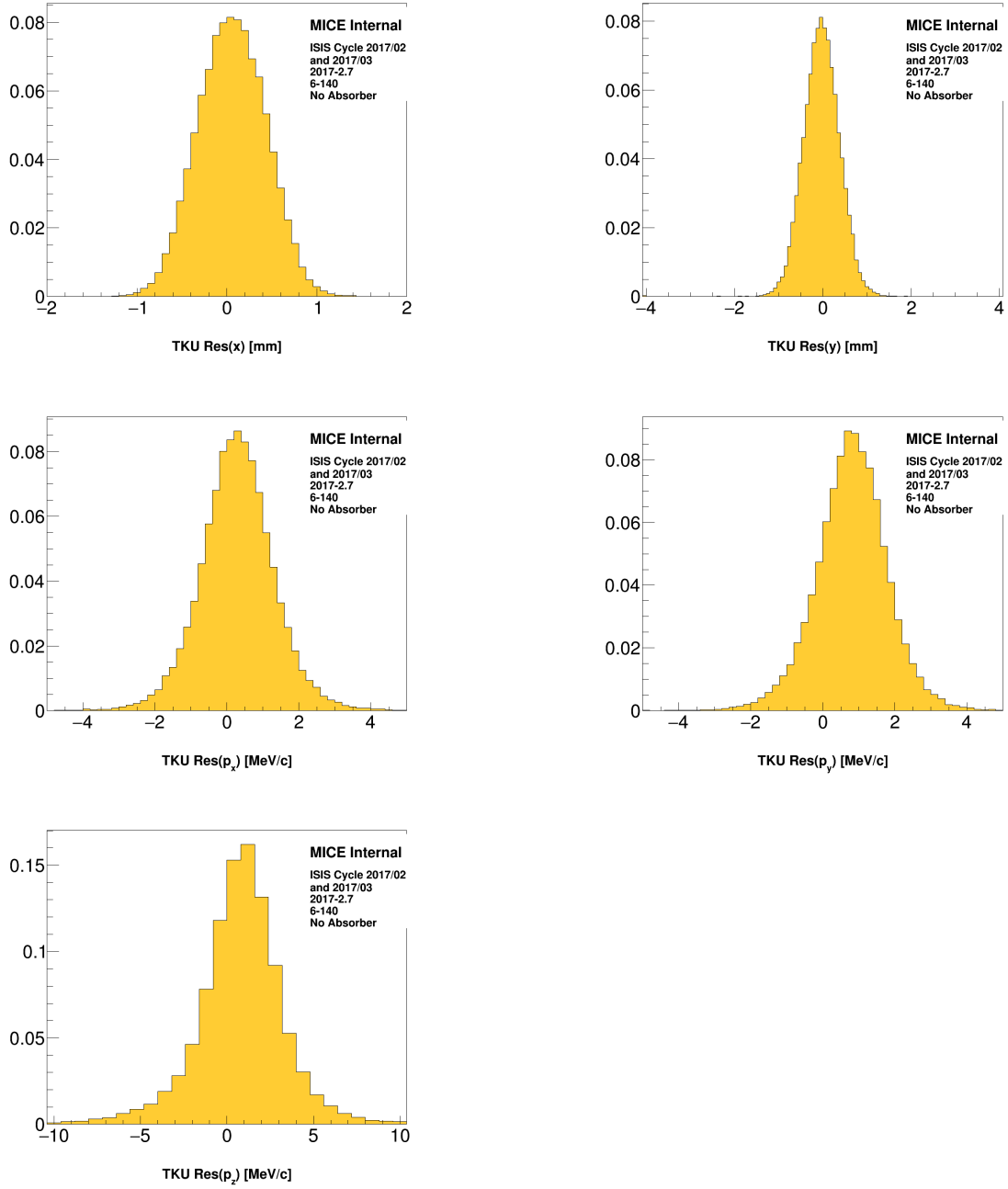
31

Figure 18: Simulated TKU resolution in the transverse phase space variables and pz for events in the upstream sample.

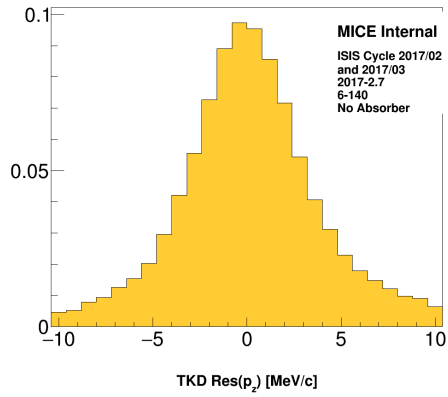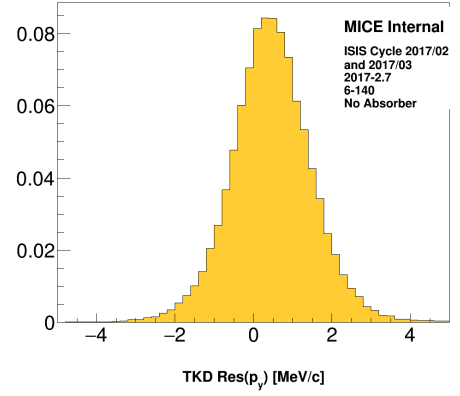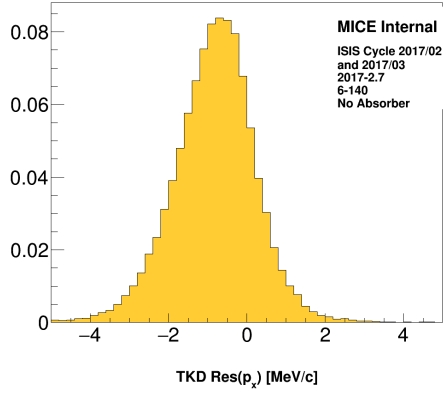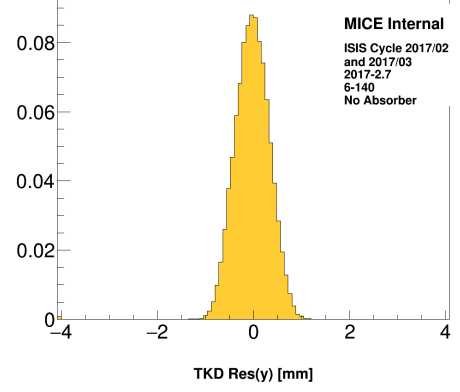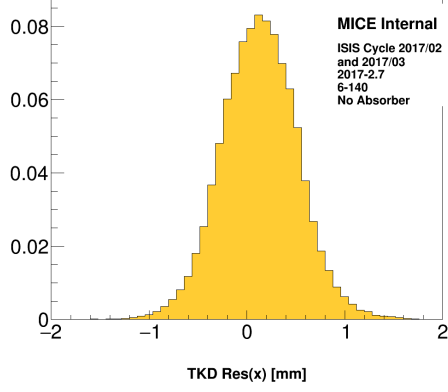helix in the non-uniform fields near to the end coils.

Figure 19: Simulated TKD resolution in the transverse phase space variables and pz for events in the down-stream sample.
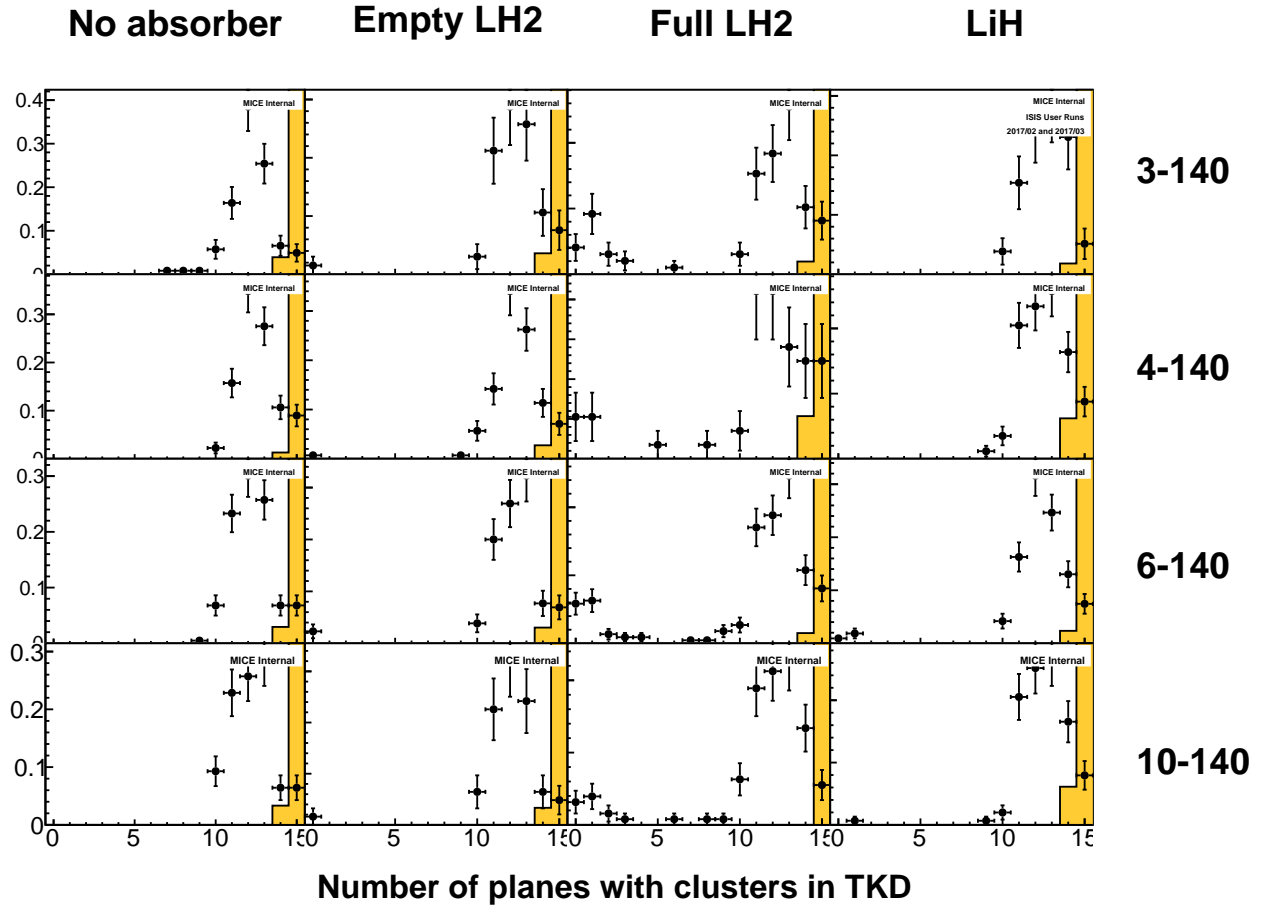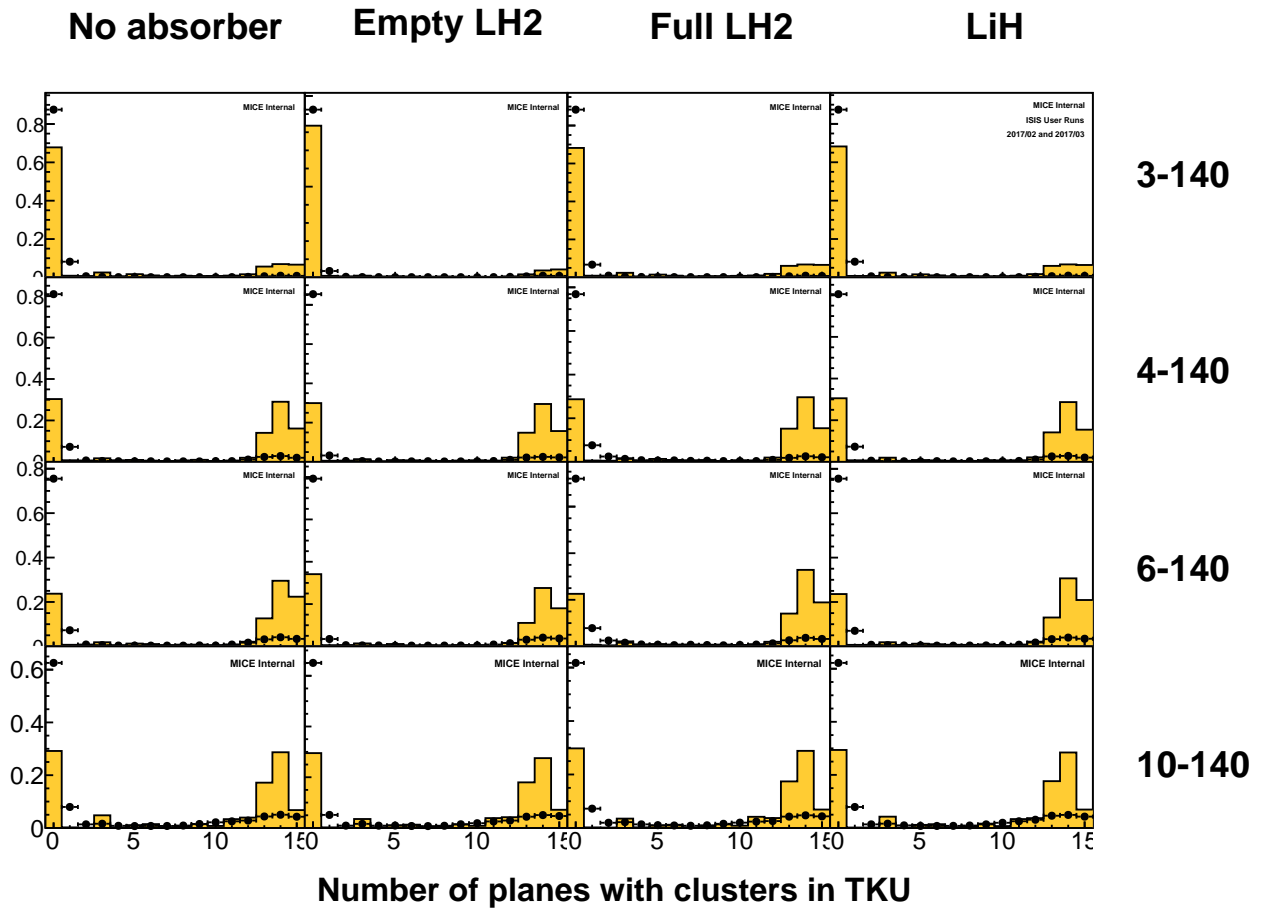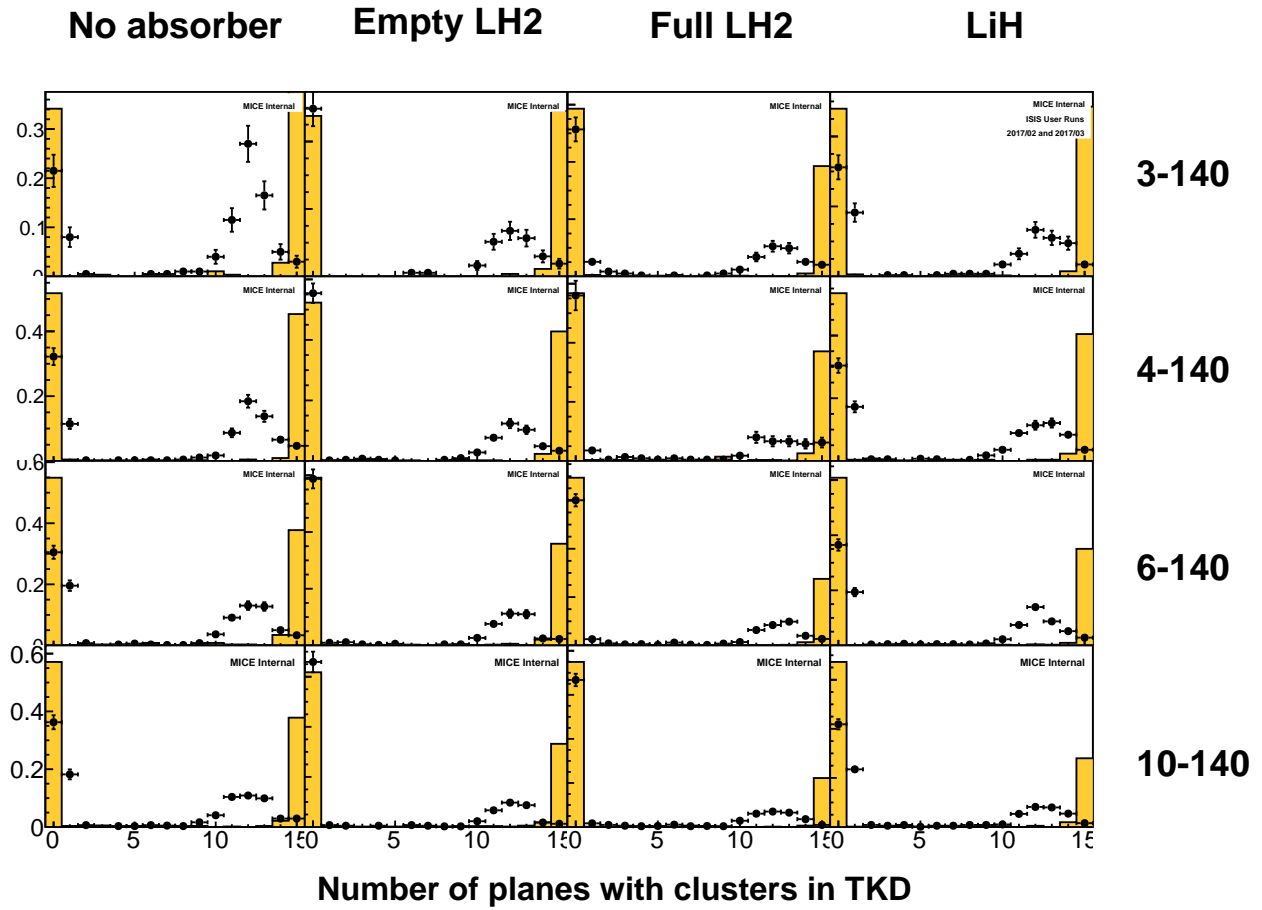
Figure 20: Number of planes in TKD that contain at least one cluster. Here we take all events in the upstream sample, and add the requirement that exactly one space point was reconstructed in ToF2 and no track was reconstructed in TKD.

Figure 21: Number of planes in TKU that contain at least one cluster. Here we take all events in the upstream sample, except we require that no TKU track was constructed. The peak around 13-14 planes are real particles in TKU that were not reconstructed. A few events are observed with fewer than 5 clusters which may be associated with noise.

Figure 22: Number of planes in TKD that contain at least one cluster. Here we take all events in the upstream sample, and add the requirement that no track was reconstructed in TKD. The peak at 15 planes are real particles in TKD that were not reconstructed. The peak at 5 planes arises due to noise. In the overlap region, a few events may have sufficient clusters to produce a track, which could lead to impurity due to noise.
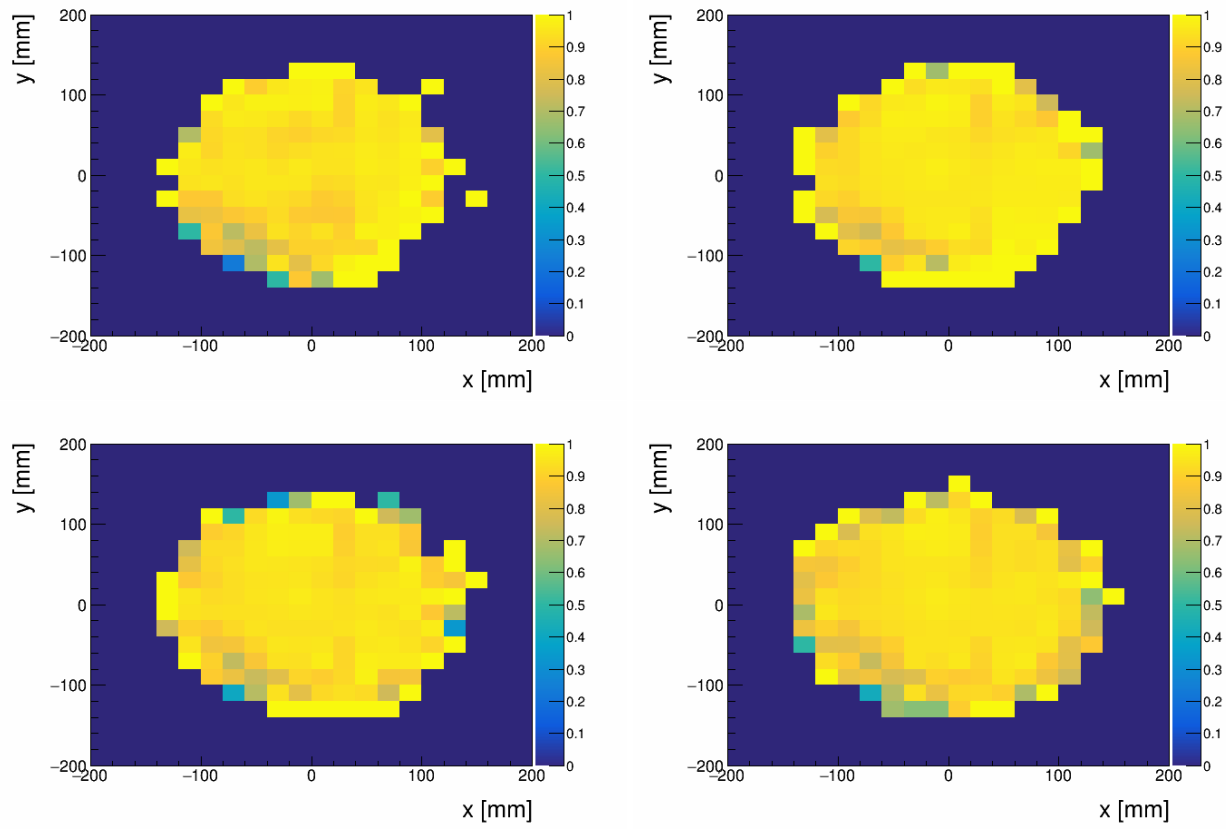
Figure 23: TKD efficiency as a function of x and y for 3-140 (top left); 4-140 (top right); 6-140 (bottom left) and 10-140 (bottom right) configuratons.
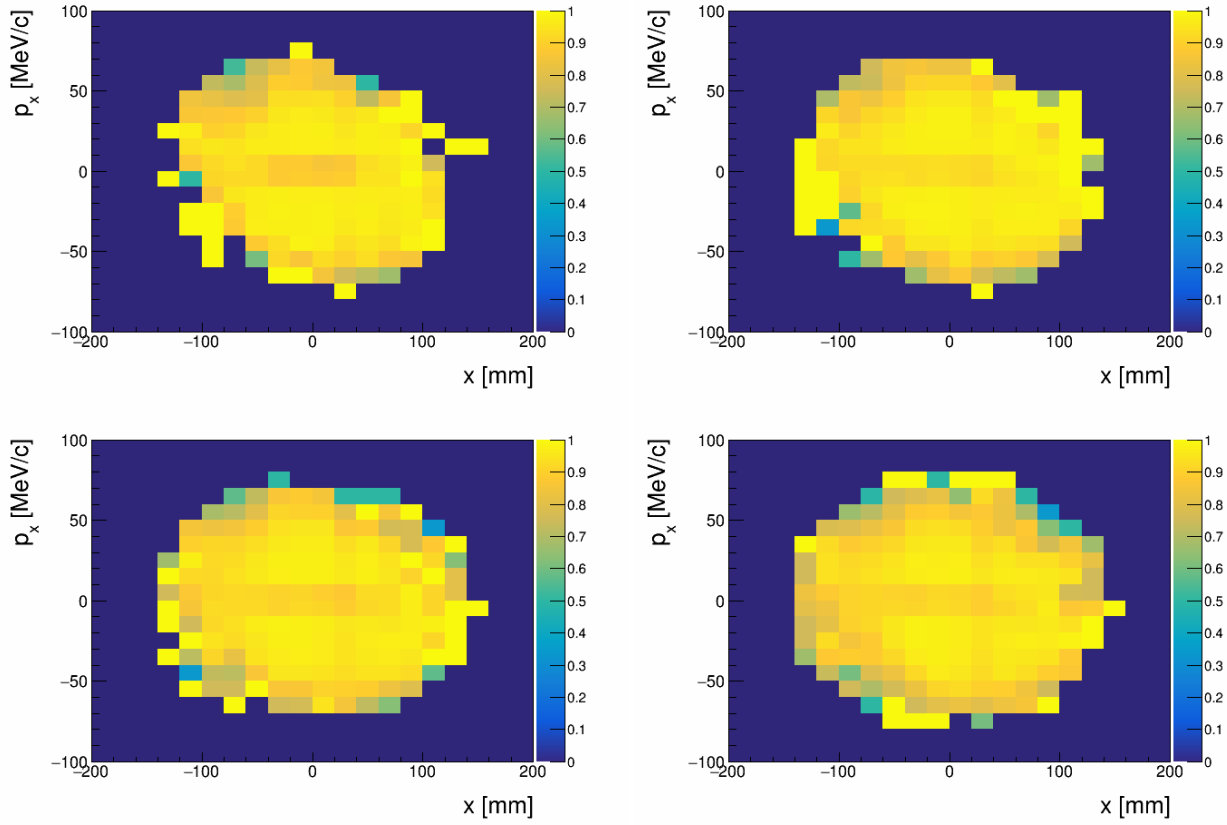
Figure 24: TKD efficiency as a function of x and p_x for 3-140 (top left); 4-140 (top right); 6-140 (bottom left) and 10-140 (bottom right) configuratons.
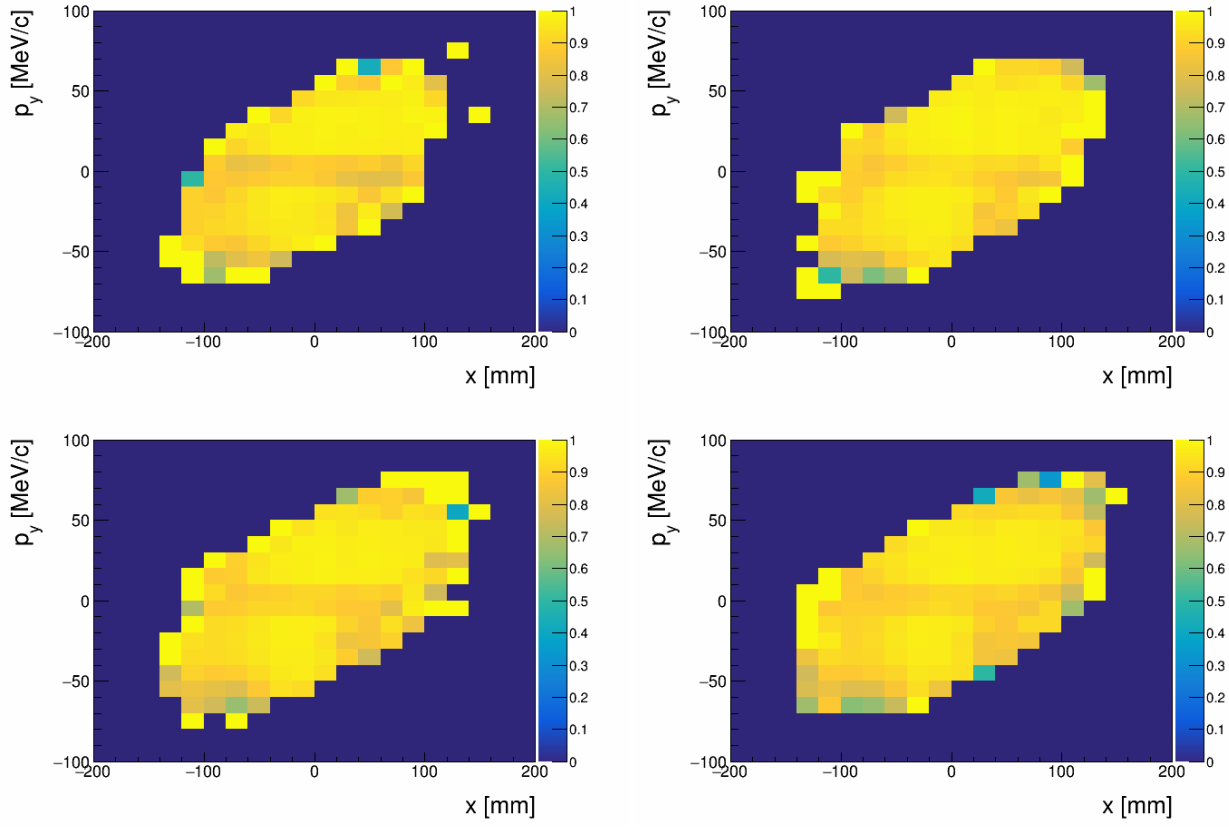
Figure 25: TKD efficiency as a function of x and p_y for 3-140 (top left); 4-140 (top right); 6-140 (bottom left) and 10-140 (bottom right) configuratons.
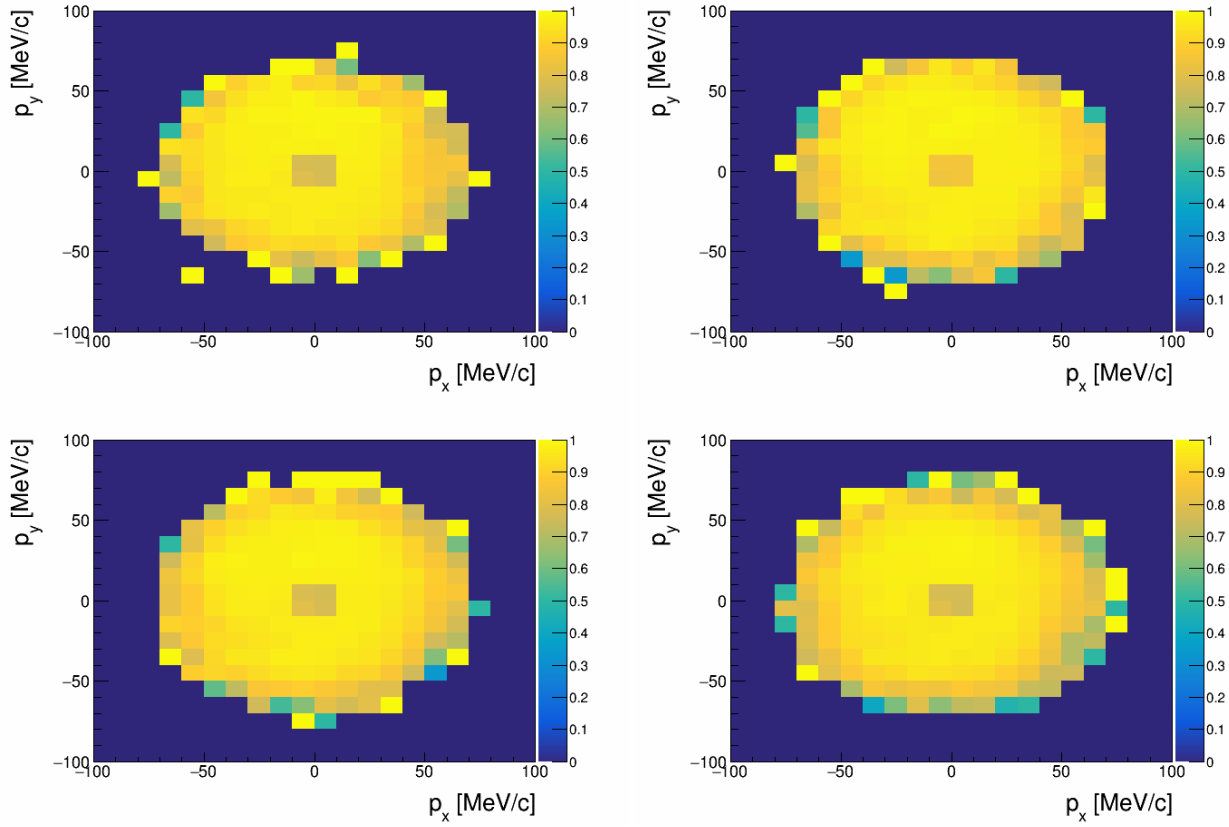
Figure 26: TKD efficiency as a function of p_x and p_y for 3-140 (top left); 4-140 (top right); 6-140 (bottom left) and 10-140 (bottom right) configuratons.

3.2 ToF
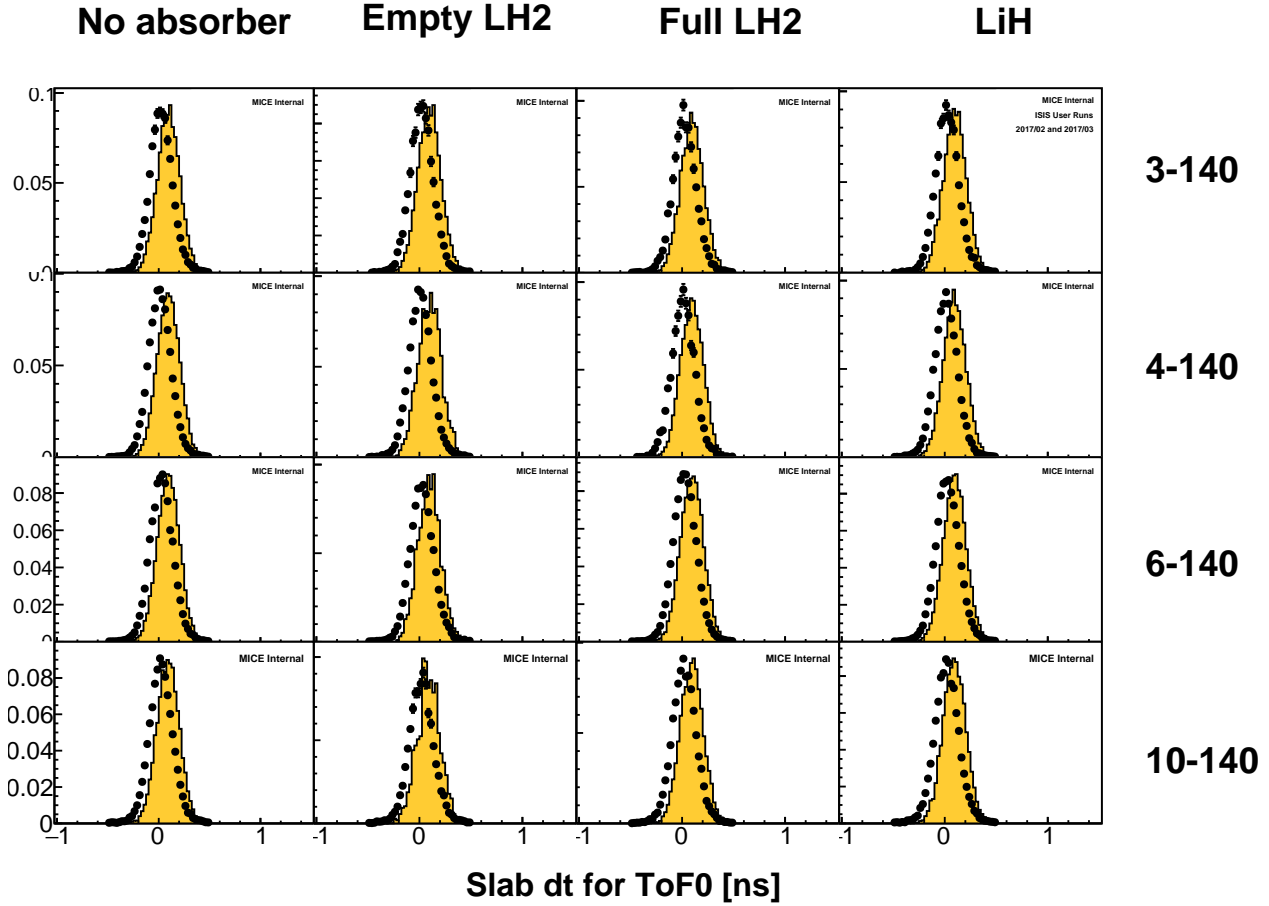
Figure 27: Measured time difference between ToF0 slabs for events in the upstream sample.

Three ToF stations are used to measure the time at which particles pass through the experiment. The ToF stations consist of two layers aligned at right angles, each made up of several scintillating plastic slabs. Each slab has a PMT at either end that records the time at which particles pass through the detector. Reconstruction software searches for coincidences of the PMTs at either end of a slab and coincidences of slabs in each layer in order to make a ToF "space point". A calibration is applied to account for cable lengths and correct for so-called "time walk" that arises due to a different PMT response for a different charge deposited by the PMT.

The ToF resolutions can be estimated by comparing the reconstructed time between each slab, after calibration. This is shown for each of the ToF detectors in fig. 27, 28 and 29. Inconsistency in the reconstruction at the 100 ps level has been observed. Investigation has shown calibration issues that effect the calibration differently in different pixels. The resolution is considered acceptable for this analysis as the muons are not highly relativistic. The inconsistency is greater for the simulation.

As the ToF is only used for validation of the tracker and for particle identification in the upstream region, impurity and inefficiency in the ToF does not affect this analysis.
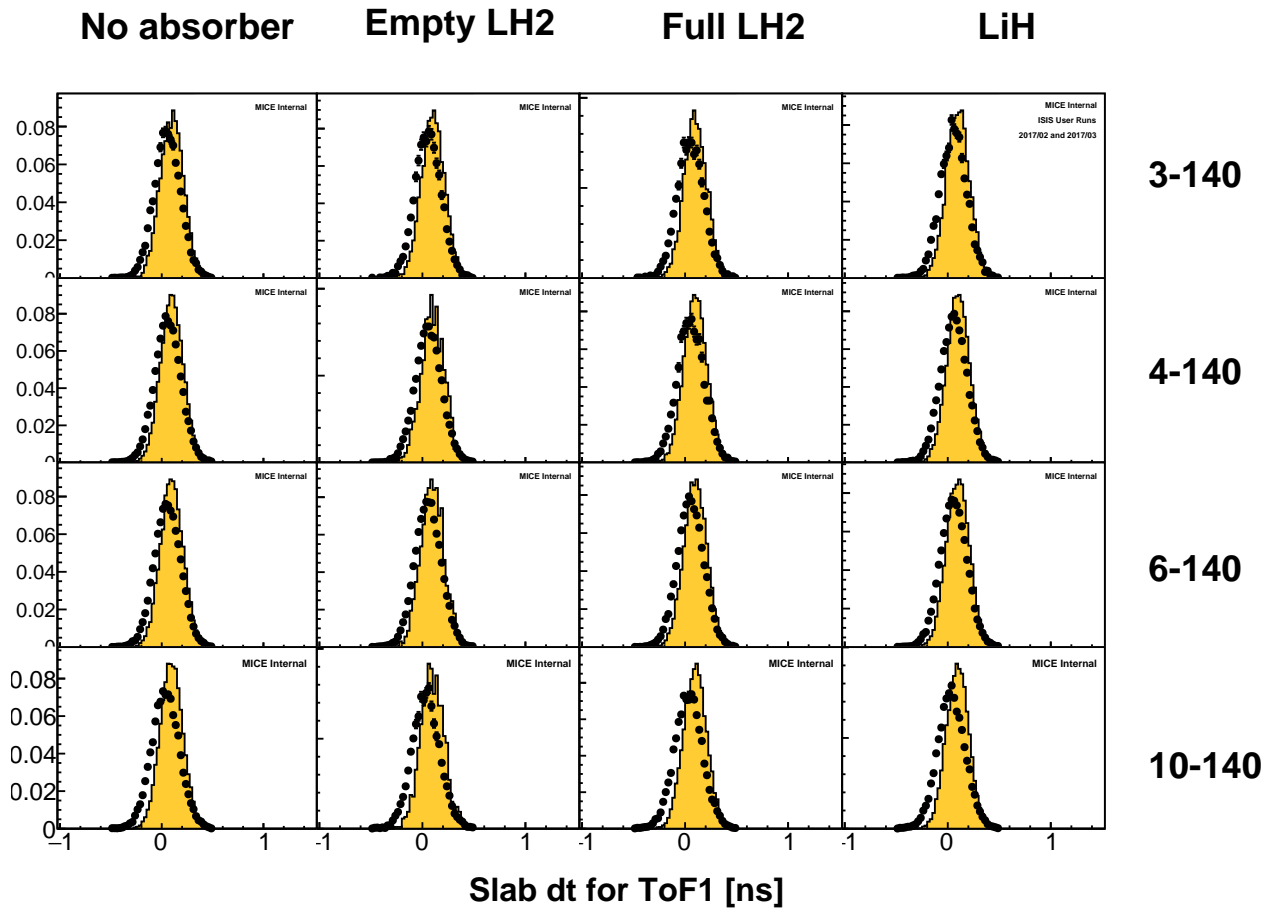
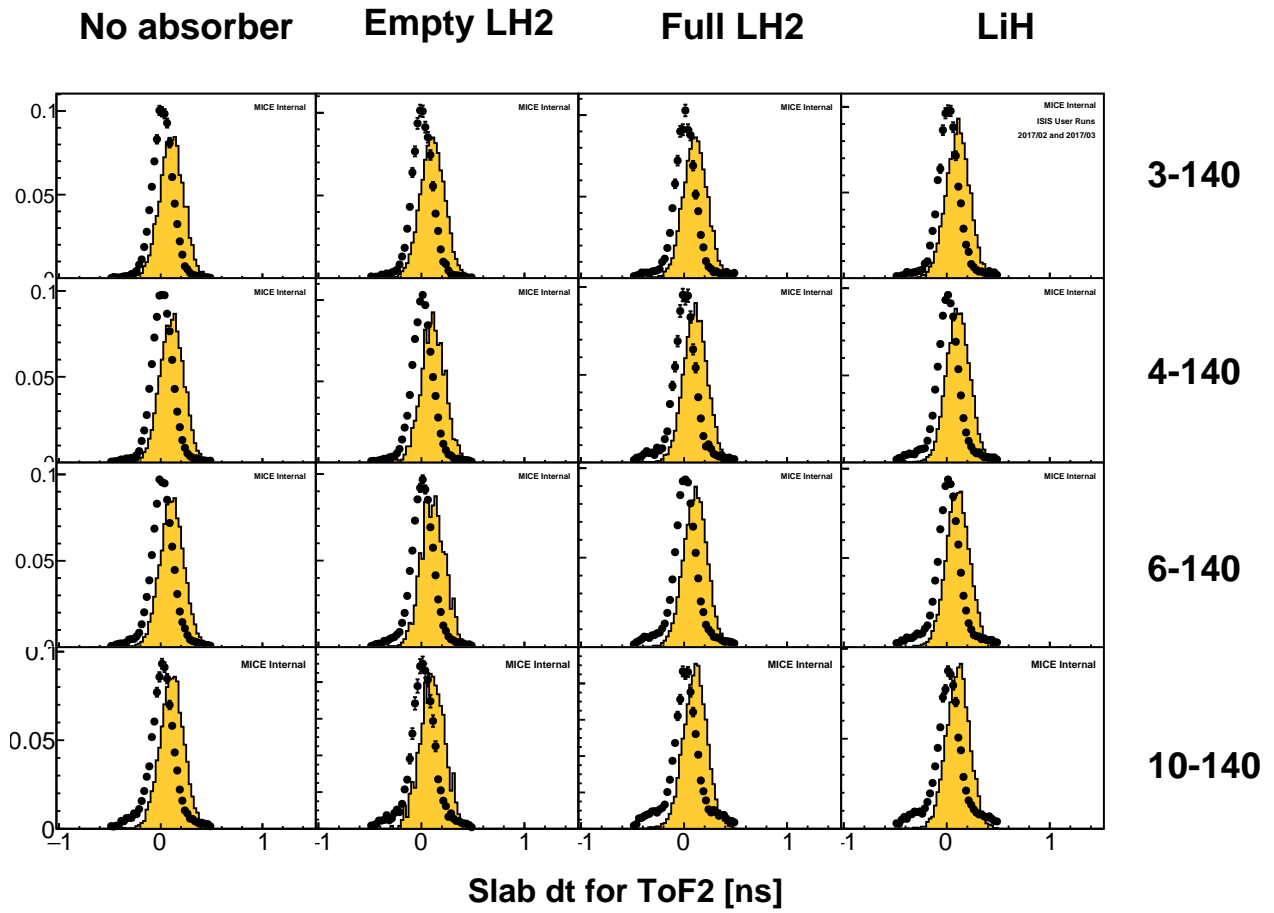Figure 28: Measured time difference between ToF1 slabs for events in the upstream sample.

No absorber **Empty LH2** **Full LH2** **LiH**

3-140

4-140

6-140

10-140

Slab dt for ToF2 [ns]

Figure 29: Measured time difference between ToF2 slabs for events in the downstream sample that make a ToF2 space point.

3.3 Global reconstruction

The overall detector performance can be validated by extrapolating tracks from one detector to another and comparing the reconstructed coordinates with the extrapolated values. Tracks measured in the upstream tracker are extrapolated upstream to ToF1 and ToF0, and downstream to TKD and ToF2. Where there are materials in the beamline, the energy change on passing through the material is estimated using the most probably energy loss. Material thicknesses are approximated by the on-axis thickness. Tracks were extrapolated through the fields using 4th-order Runge-Kutta integration of the Lorentz force law.

Asymmetric effects can be introduced due to scattering from the walls of the cooling channel as the beam is not symmetric in the channel. In order to minimise the effects of such scattering, only events whose projected trajectory is significantly distant from the apertures are considered in this analysis. The following sample selection is considered:

- Downstream sample: Events must be included in the downstream sample to be considered in this analysis
- Aperture cut: The projected upstream track must be within 100 mm radius from the beam axis at the following apertures: the upstream absorber safety window; the upstream absorber window; the absorber centre; the downstream absorber window; the downstream absorber safety window; the upstream edge of SSD; the Helium window in SSD; the downstream edge of the downstream PRY aperture. This is performed even when the lH2 absorber was not installed, for the sake of consistency and because in some instances mounting flanges can limit the aperture.
- 1 space point in ToF2: The event must have exactly one space point in ToF2.
- Successful track extrapolation to TKD and ToF2: The projected upstream track must have been successfully extrapolated to TKD and ToF2

The sample sizes are shown for data in table 13 and 14. The equivalent MC sample sizes are listed in 15 and 16.

Table 13: The extrapolated reconstructed data sample is listed. Samples are listed for 3-140 and 4-140 datasets.

	2017-2.7 3-140 None	2017-2.7 3-140 lH2 empty	2017-2.7 3-140 lH2 full	2017-2.7 3-140 LiH	2017-2.7 4-140 None	2017-2.7 4-140 lH2 empty	2017-2.7 4-140 lH2 full	2017-2.7 4-140 LiH
Downstream Sample	12945	8598	8838	11641	29028	23143	8146	23345
Cooling channel aperture cut	7218	4735	5171	6836	17681	14487	4919	14254
One space point in ToF2	6954	4524	4896	6485	16803	13790	4597	13370
Successful extrapolation to TKD	6954	4524	4896	6485	16803	13790	4597	13370
Successful extrapolation to ToF2	6954	4524	4896	6485	16803	13790	4597	13370
Extrapolation Sample	6954	4524	4896	6485	16803	13790	4597	13370

Table 14: The extrapolated reconstructed data sample is listed. Samples are listed for 6-140 and 10-140 datasets.

	2017-2.7 6-140 None	2017-2.7 6-140 lH2 empty	2017-2.7 6-140 lH2 full	2017-2.7 6-140 LiH	2017-2.7 10-140 None	2017-2.7 10-140 lH2 empty	2017-2.7 10-140 lH2 full	2017-2.7 10-140 LiH
Downstream Sample	25727	16864	28459	30013	12971	6430	13461	15462
Cooling channel aperture cut	15180	10067	15993	17021	5577	2796	4977	5960
One space point in ToF2	14432	9478	14854	15780	5257	2612	4476	5373
Successful extrapolation to TKD	14432	9478	14854	15780	5257	2612	4476	5373
Successful extrapolation to ToF2	14432	9478	14854	15780	5257	2612	4476	5373
Extrapolation Sample	14432	9478	14854	15780	5257	2612	4476	5373

Table 15: The extrapolated reconstructed simulated sample is listed. Samples are listed for 3-140 and 4-140 datasets.

	Simulated 2017-2.7 3-140 None	Simulated 2017-2.7 3-140 lH2 empty	Simulated 2017-2.7 3-140 lH2 full	Simulated 2017-2.7 3-140 LiH	Simulated 2017-2.7 4-140 None	Simulated 2017-2.7 4-140 lH2 empty	Simulated 2017-2.7 4-140 lH2 full	Simulated 2017-2.7 4-140 LiH
Downstream Sample	8543	9103	8382	8481	17915	1617	18121	18111
Cooling channel aperture cut	5111	5218	5032	5377	10864	984	10754	10402
One space point in ToF2	4539	4626	4499	4819	9536	867	9467	9117
Successful extrapolation to TKD	4539	4626	4499	4819	9536	867	9467	9117
Successful extrapolation to ToF2	4539	4626	4499	4819	9536	867	9467	9117
Extrapolation Sample	4539	4626	4499	4819	9536	867	9467	9117

Table 16: The extrapolated reconstructed simulated sample is listed. Samples are listed for 6-140 and 10-140 datasets.

	Simulated 2017-2.7 6-140 None	Simulated 2017-2.7 6-140 lH2 empty	Simulated 2017-2.7 6-140 lH2 full	Simulated 2017-2.7 6-140 LiH	Simulated 2017-2.7 10-140 None	Simulated 2017-2.7 10-140 lH2 empty	Simulated 2017-2.7 10-140 lH2 full	Simulated 2017-2.7 10-140 LiH
Downstream Sample	16809	1539	17490	17549	7856	667	8422	8517
Cooling channel aperture cut	10235	895	9444	9899	3392	313	3221	3324
One space point in ToF2	8993	783	8219	8576	2927	269	2772	2858
Successful extrapolation to TKD	8993	783	8219	8576	2927	269	2772	2858
Successful extrapolation to ToF2	8993	783	8219	8576	2927	269	2772	2858
Extrapolation Sample	8993	783	8219	8576	2927	269	2772	2858
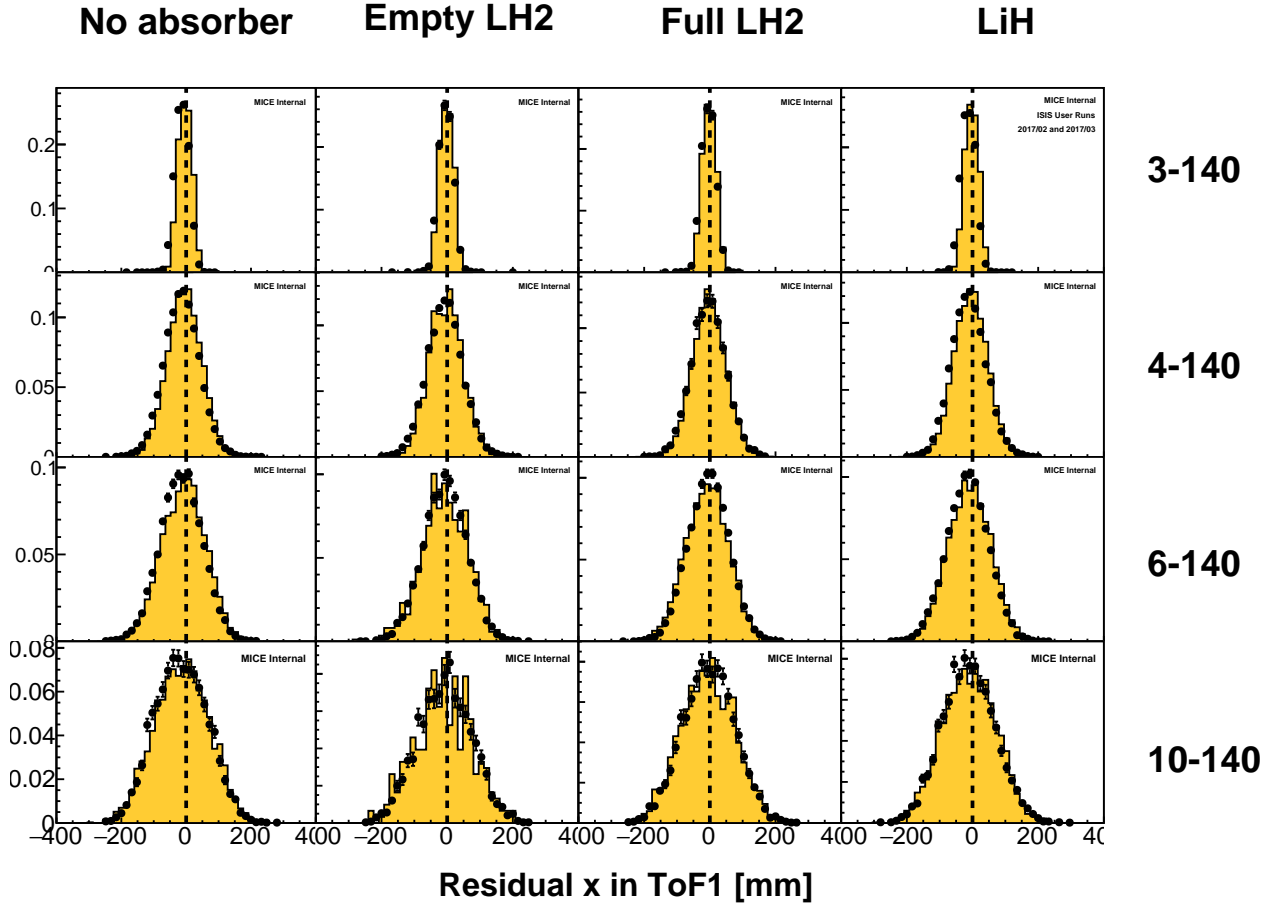
Figure 30: Residual horizontal (x) position in ToF1 of tracker tracks following extrapolation from TKU.

The extrapolated position following extrapolation to ToF1 is shown in fig. 30 and 31. In general the width of the distributions are comparable between MC and data. Where the diffuser is in place for higher emittance beams, the extrapolation goes through the diffuser material so the residuals are wider, owing to the increased scattering from the diffuser.

The time-of-flight residual in data shows a systematic offset from 0 and relative to the MC. The offset from 0 gets worse for higher emittance beams. It is thought to be an intrinsic property of the beam; muons that are scattered in materials between the tracker and the ToF have systematically shorter path lengths than the extrapolated trajectories, resulting in systematically longer extrapolated time of flight. There is some level of agreement between data and MC; the deficiency in the simulated ToF reconstruction as mentioned in sec. 3.2 is noted and may explain the discrepancy between data and MC here.

Small misalignments between TKU extrapolated tracks and TKD are observed, indicated by the offset of transverse variables from 0, shown in fig. 33 and 34. There are known, uncorrected misalignments in the detector system and there are expected to be additional misalignments in the magnets which could lead to these offsets.

The total momentum shows discrepancy between TKU and TKD of about 1 MeV/c. This is consistent with the systematic offset in the tracker momentum resolution shown in fig. 18 and 19. It is interesting to note that the level of agreement between MC and data varies on a setting-by-setting basis in a statistically significant manner. Agreement is better for the settings where the liquid hydrogen windows were installed.

Further small misalignments are observed in the position residuals between ToF2 and tracks extrapolated
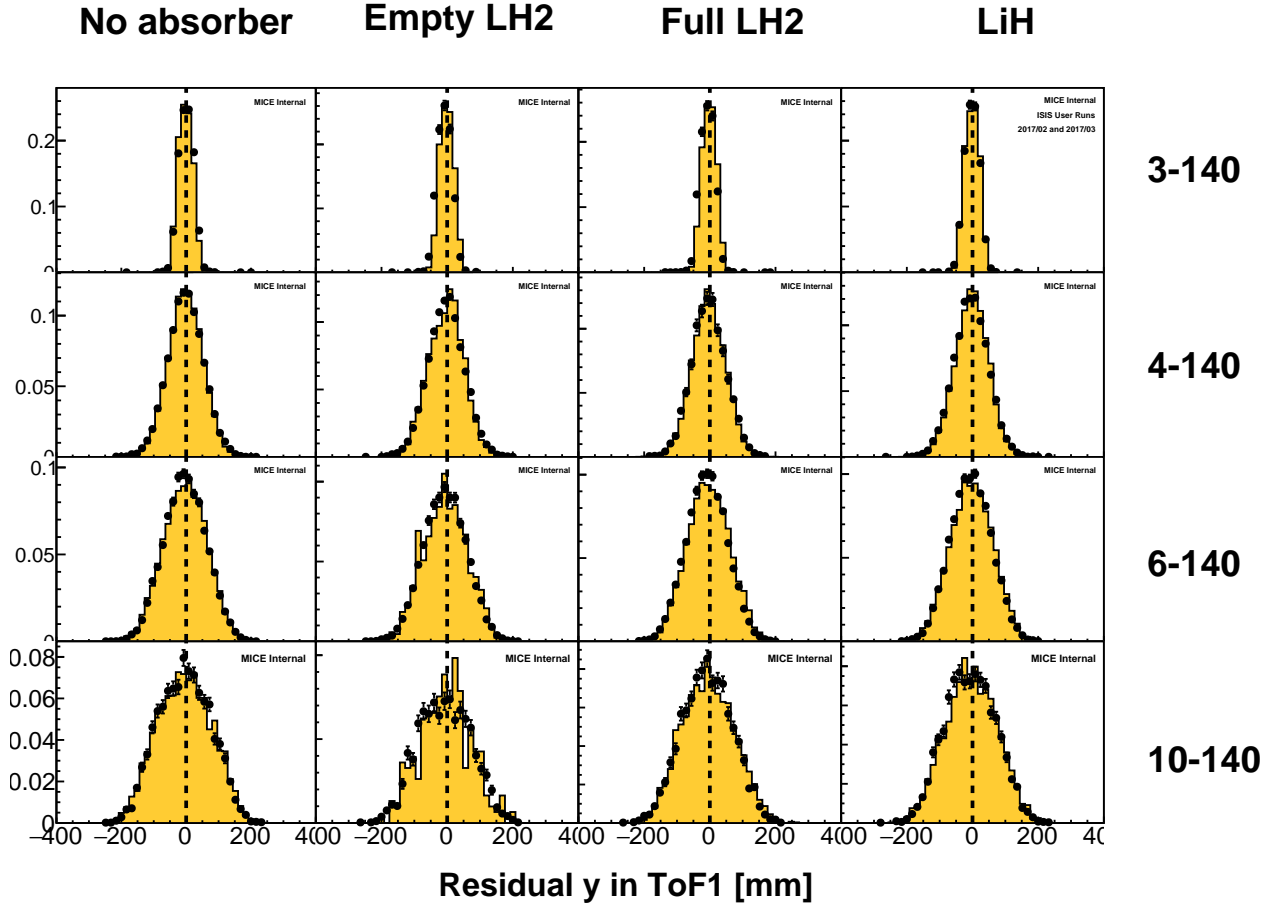
Figure 31: Residual vertical (y) position in ToF1 of tracker tracks following extrapolation from TKU.

from TKD. This is attributed to alignment issues.

The discrepancy between the time measured in ToF1 and the time measured in ToF2, using the extrapolated TKU track to estimate the time difference, is shown in fig. 38. Discrepancy is observed of the order of 300 ps. Significant discrepancy between MC and data is observed.

The discrepancy between position measured in ToF2 and the extrapolated track measured in TKD is shown in fig. 39 and 40. Discrepancy of the order of 10 mm is observed. This can arise from misalignment of the detectors in the reconstruction model or of the magnets.

3.4 Incorporation into Analysis

Discrepancies between the measurement and simulation at the level of a few MeV/c in momentum are observed in both TKU and TKD. These comparisons between the various detector systems are the only data-led validations that the reconstruction works at all.

The uncertainty is incorporated into the analysis by assuming a relatively large uncertainty in the magnetic field in the region of TKU and TKD and a significant misalignment. This yields a corresponding uncertainty in the absolute momentum scale and reconstructed amplitude distributions.
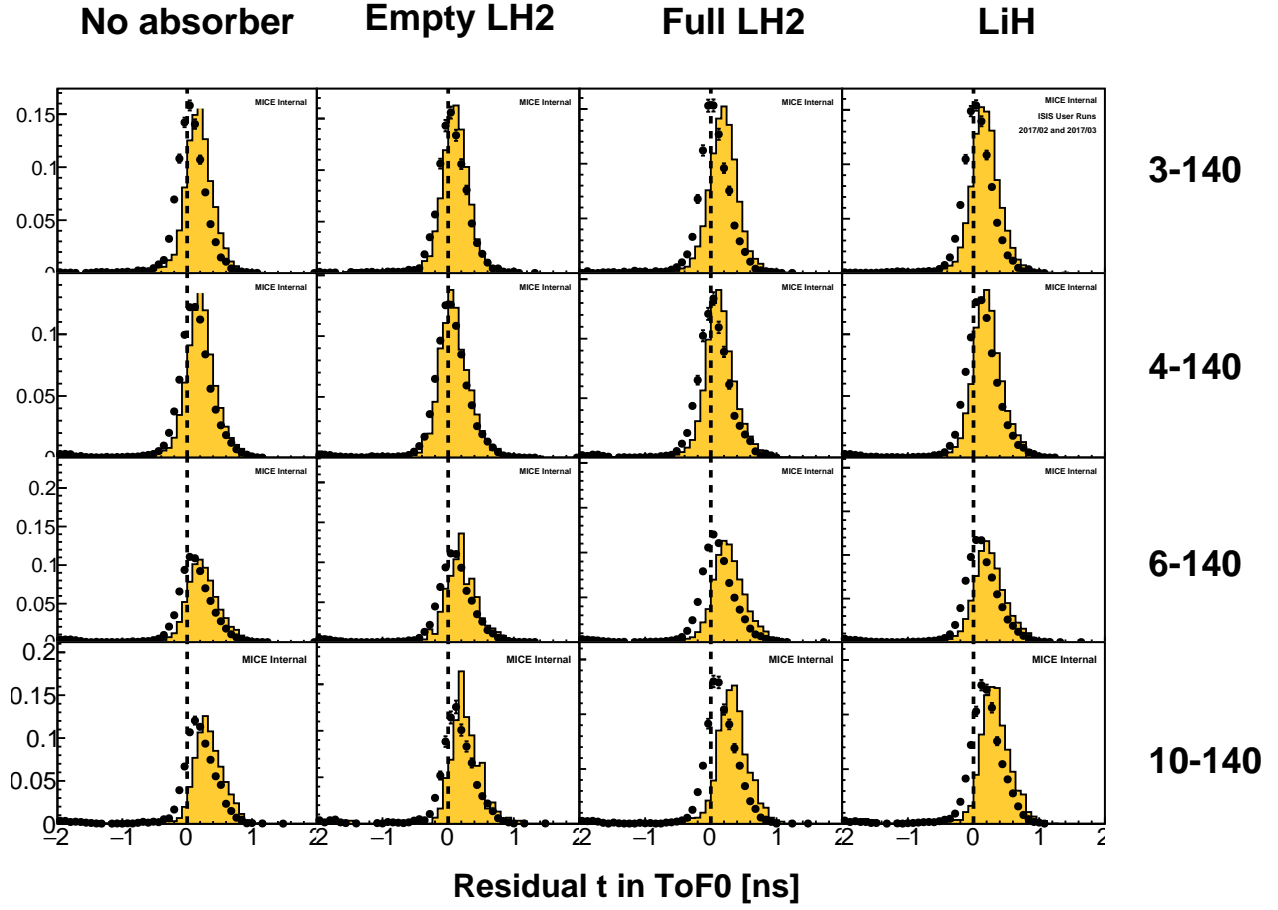
Figure 32: Residual ToF0 time of the extrapolated track. Track trajectories were drawn from TKU, while the track times were drawn from ToF1 with extrapolated offsets for time-of-flight from TKU to ToF1 considered.
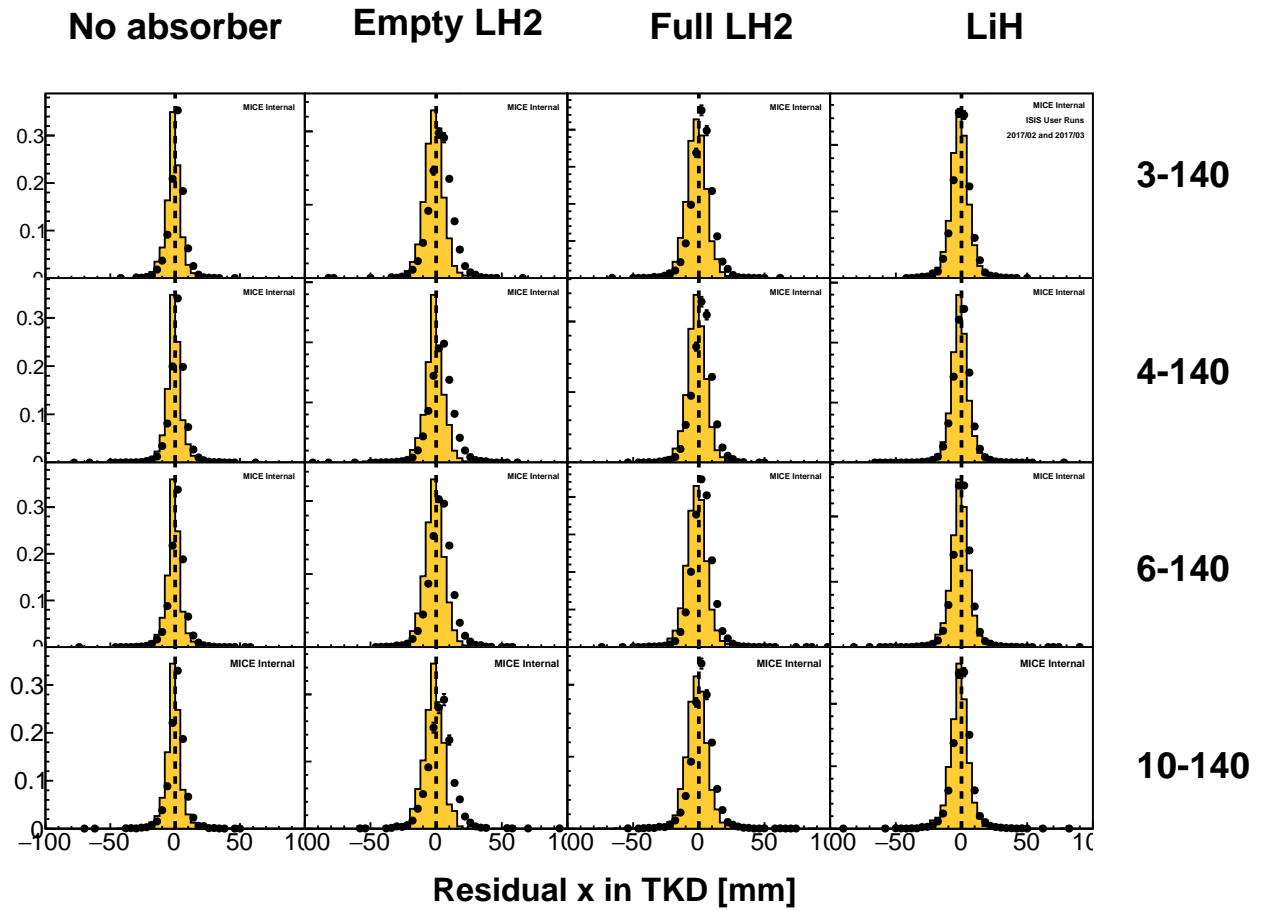
Figure 33: Residual x position of TKU tracks extrapolated to TKD, as compared to the tracks in TKD.
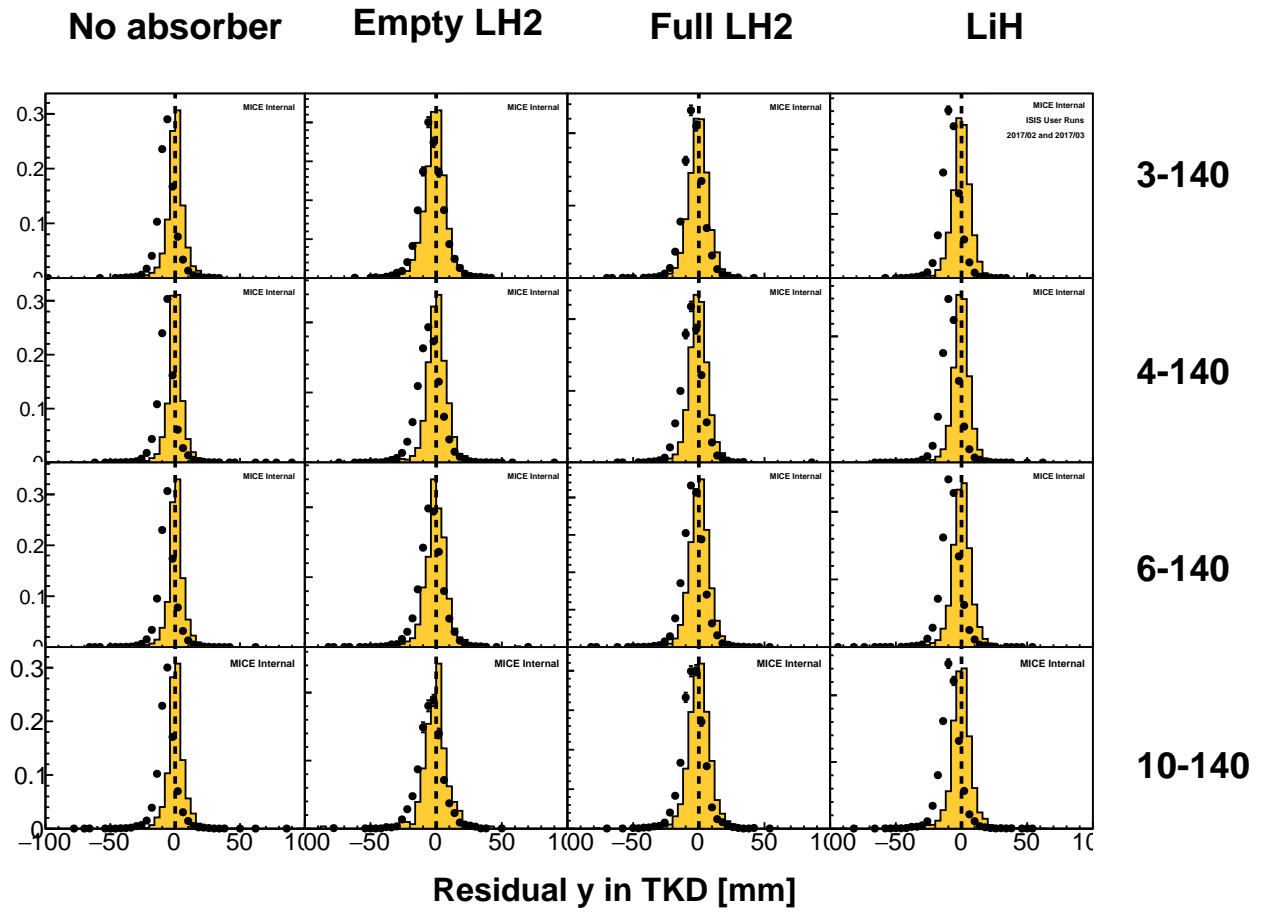
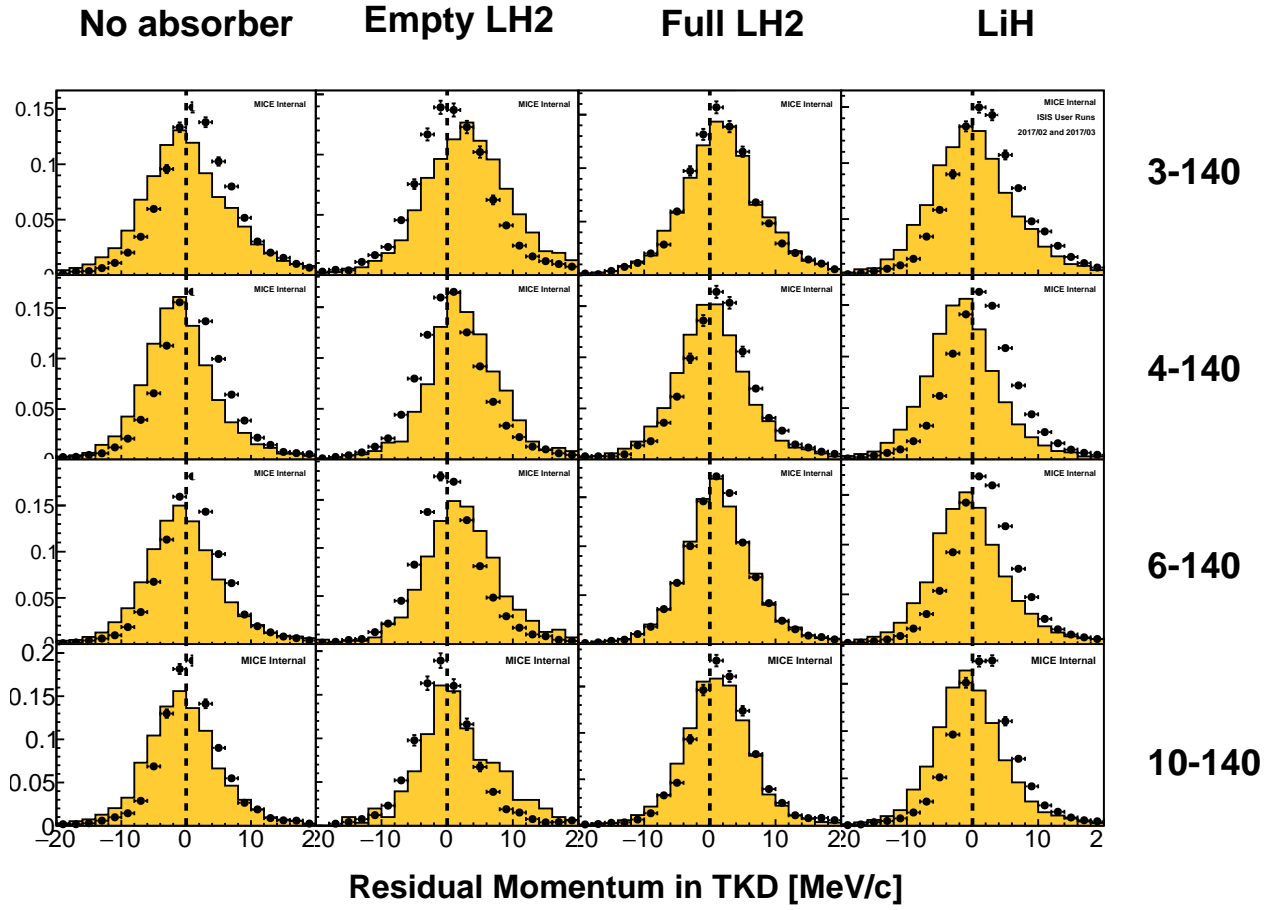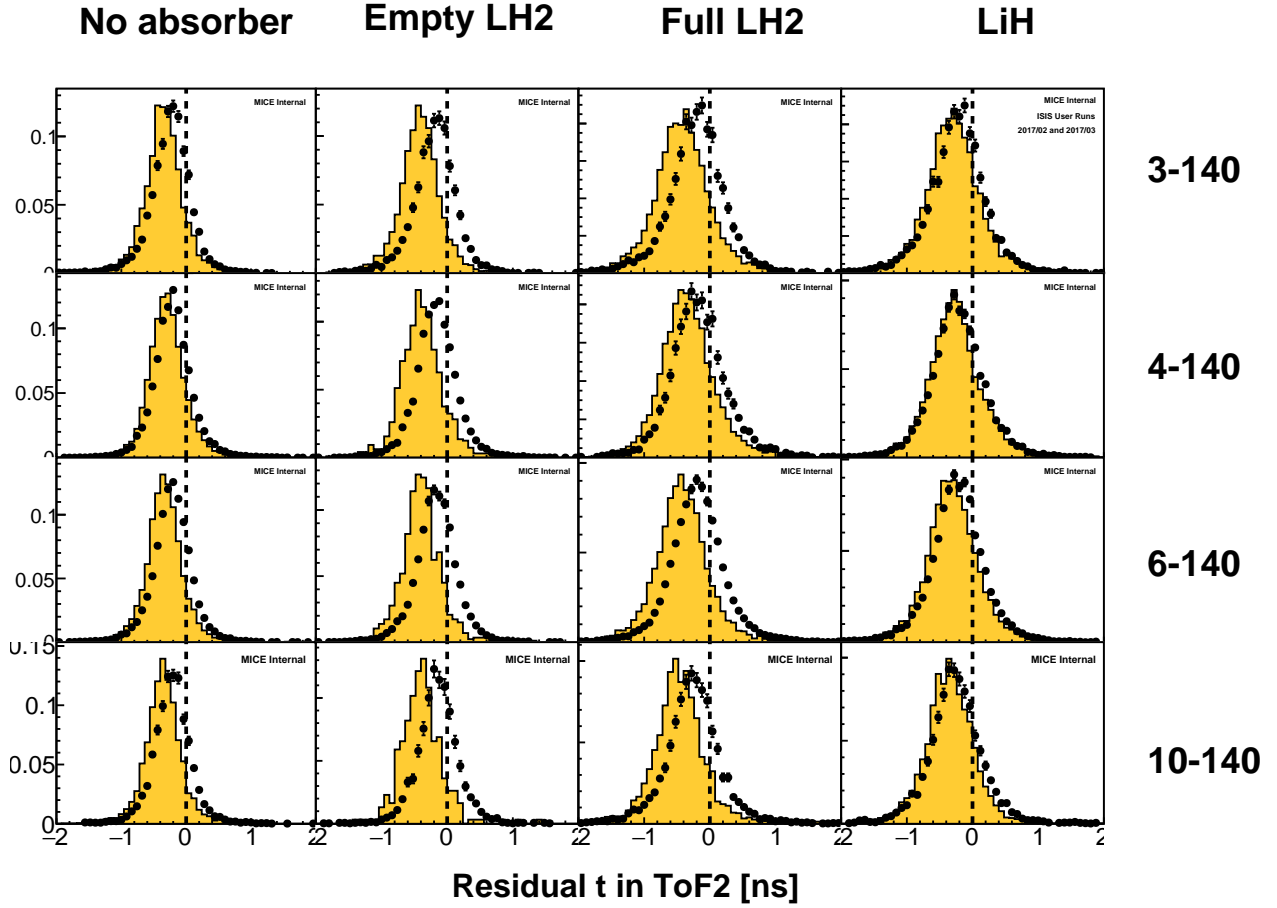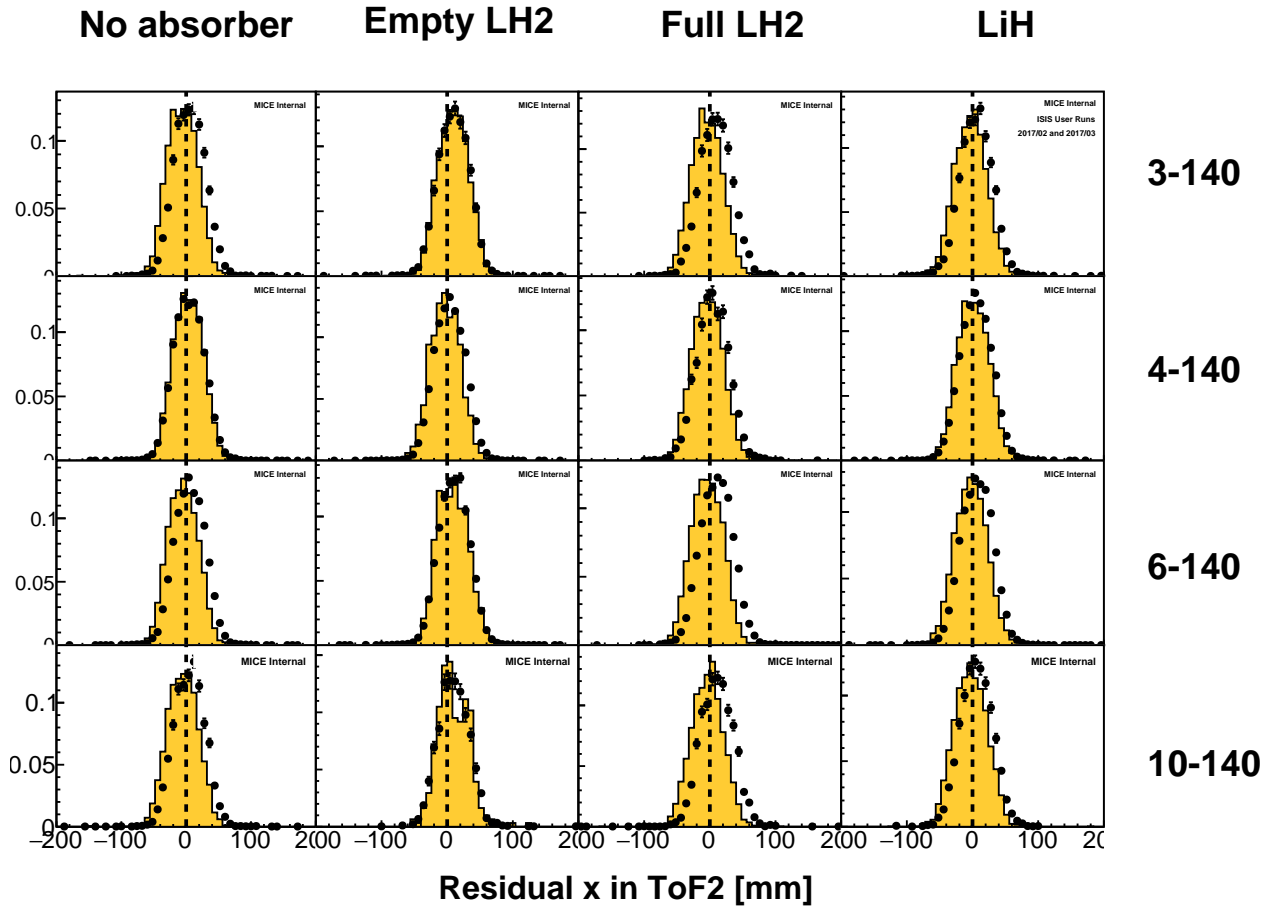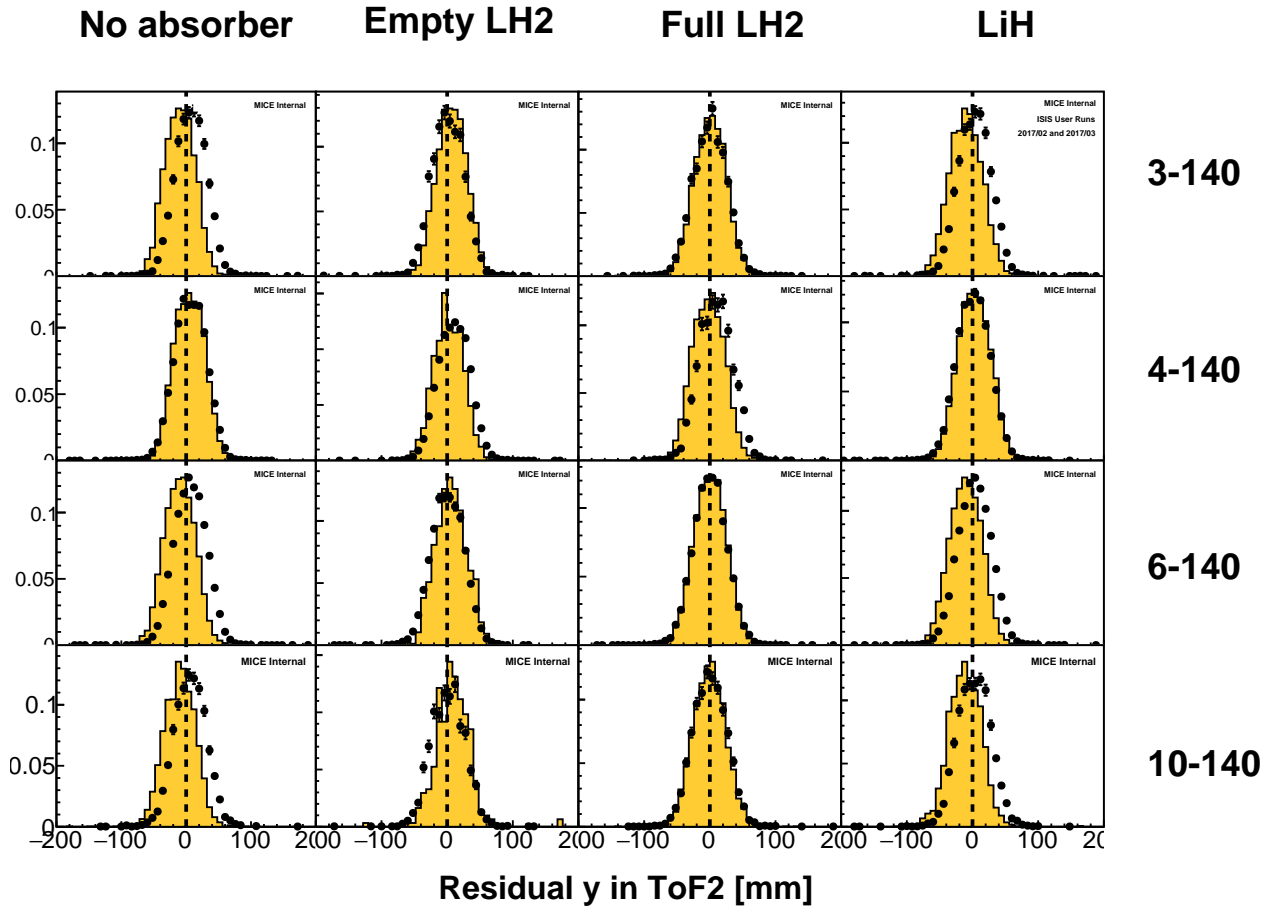Figure 34: Residual y position of TKU tracks extrapolated to TKD, as compared to the tracks in TKD.
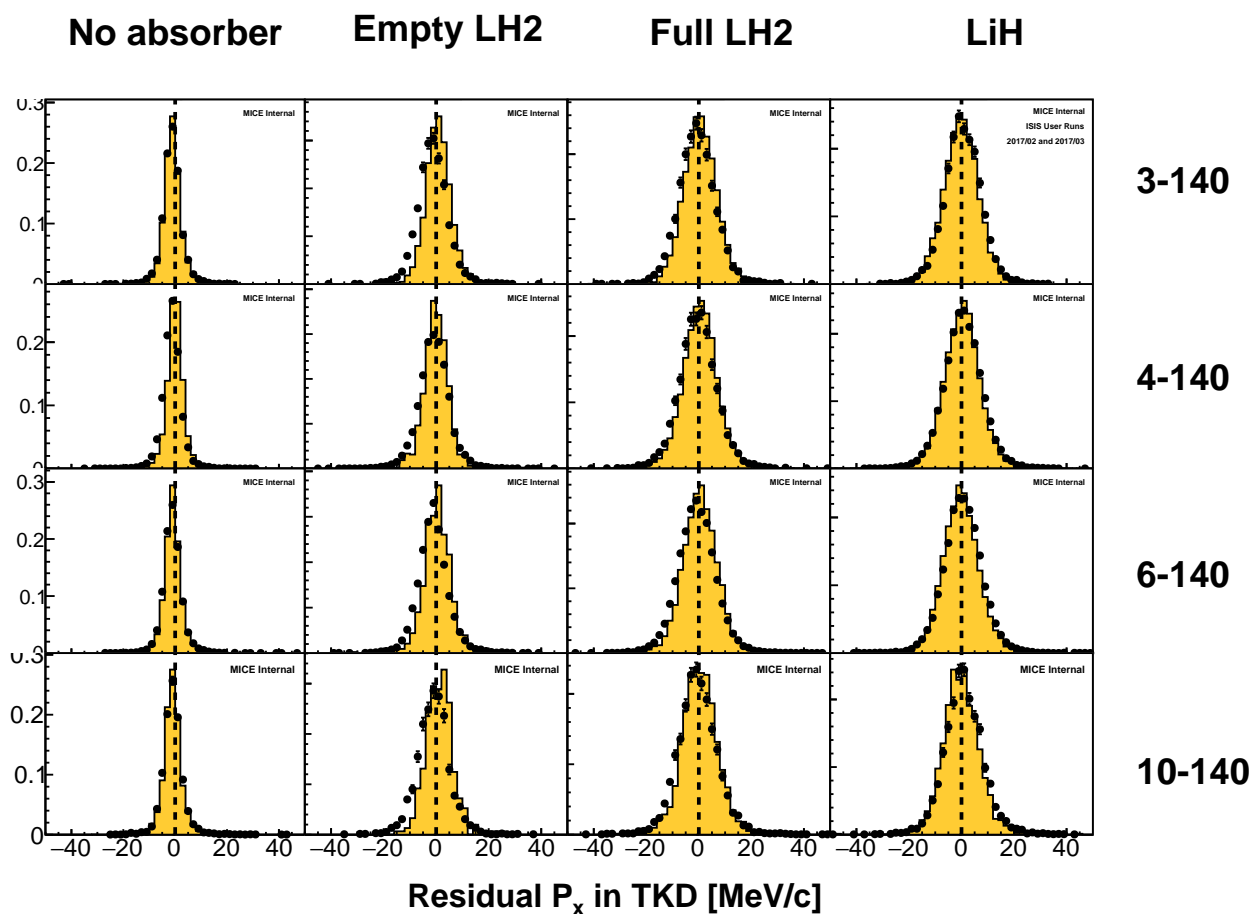
Figure 35: Residual p_x of TKU tracks extrapolated to TKD, as compared to the tracks in TKD.

54
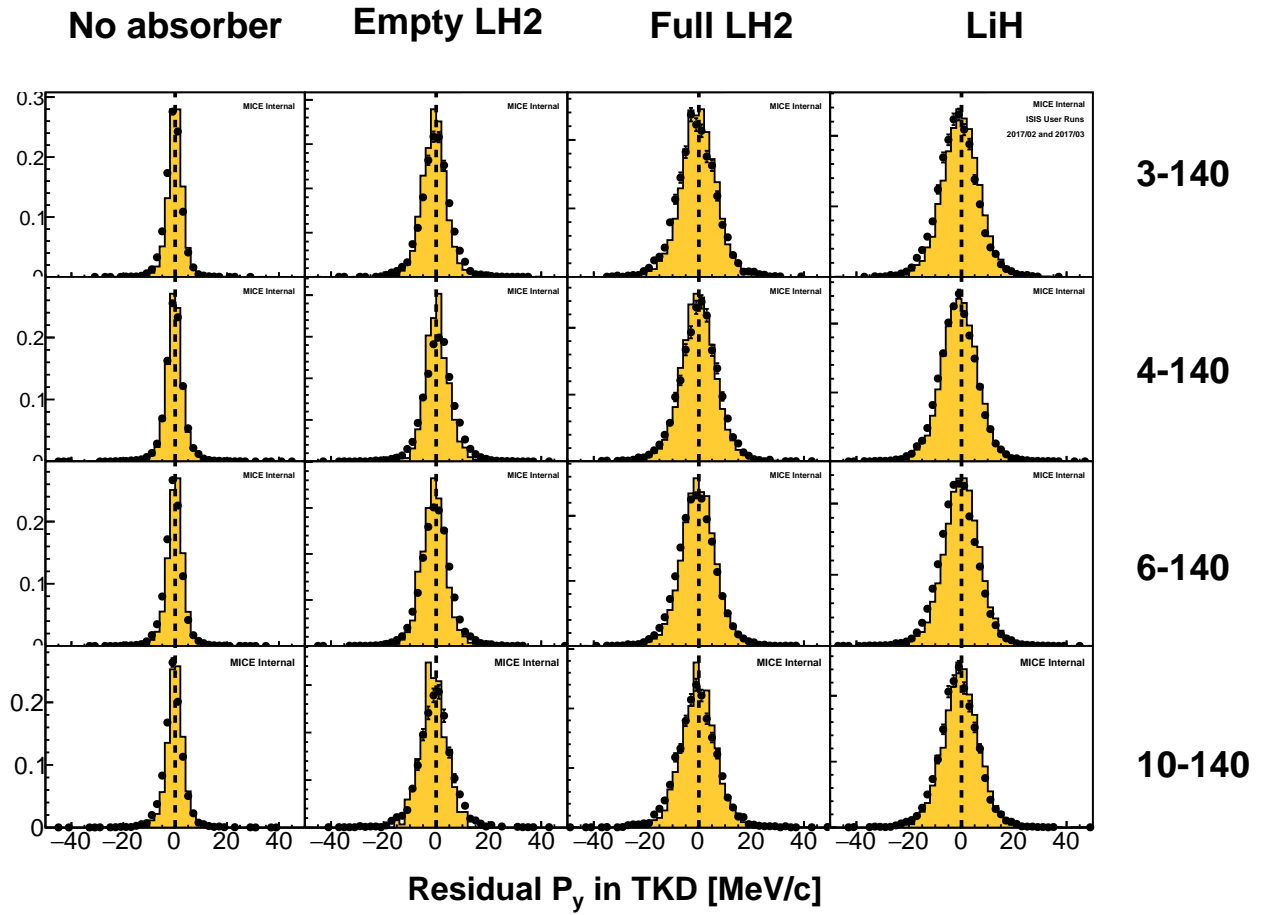
Figure 36: Residual p_y of TKU tracks extrapolated to TKD, as compared to the tracks in TKD.

Figure 37: Residual p_{tot} of TKU tracks extrapolated to TKD, as compared to the tracks in TKD.

Figure 38: Residual time of TKU tracks extrapolated to ToF2, as compared to the time measured in ToF2. The track times were drawn from ToF1 with appropriate offsets for time-of-flight from TKU to ToF1 considered.

Figure 39: Residual x position of TKD tracks extrapolated to ToF2, as compared to the position measured in ToF2.

Figure 40: Residual y position of TKD tracks extrapolated to ToF2, as compared to the position measured in ToF2.

59

4   Cooling Channel and Optics

Having validated the diagnostics, it is now of interest to examine the properties of the cooling channel.

4.1   Input Beam

The input beam distributions at the TKU reference planes are shown for position in fig. 41 and 42, for transverse momentum in fig. 43 and 44 and for total in momentum in 45. The simulated beam and data show good agreement.
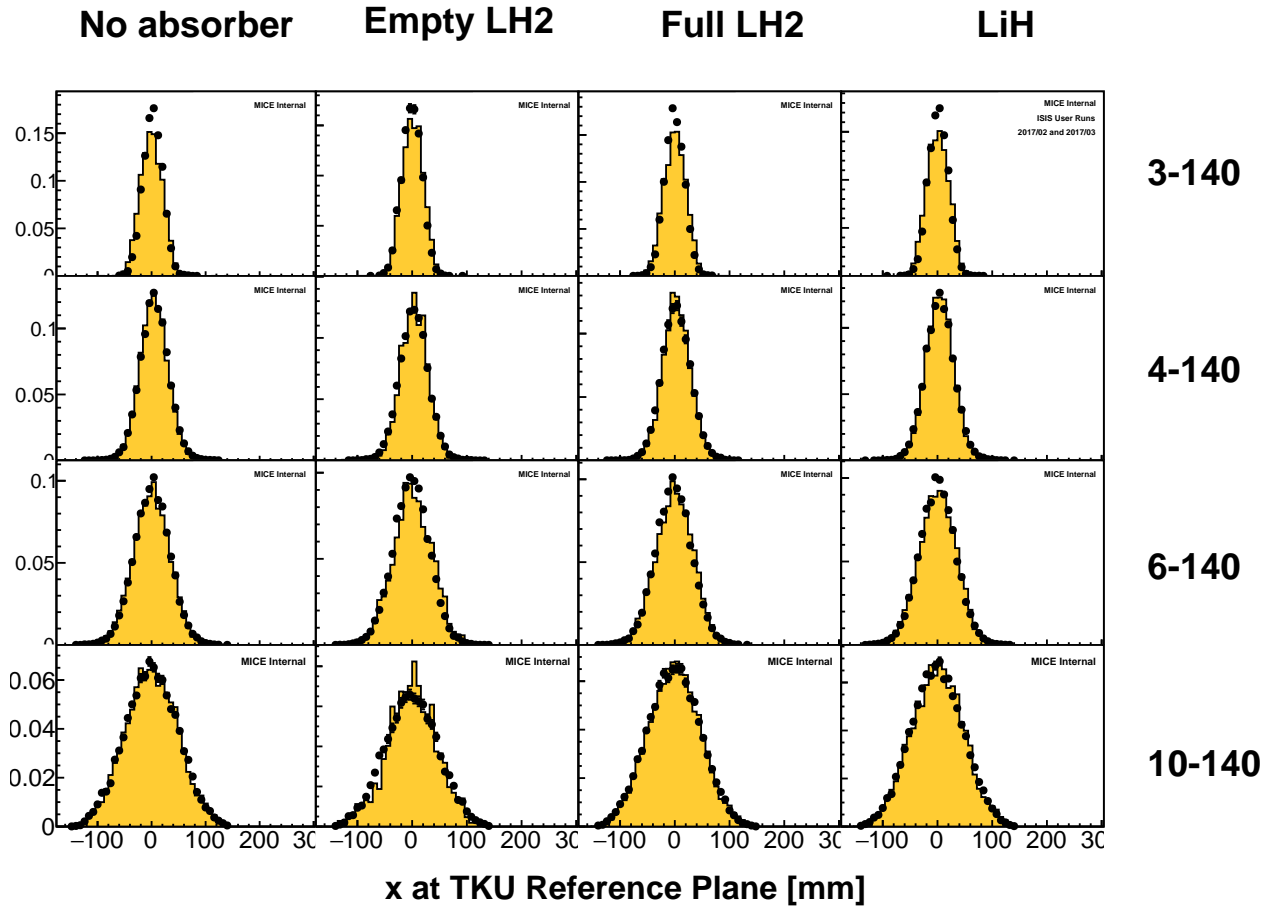
Figure 41: Horizontal position distribution in TKU for all events in the upstream sample.
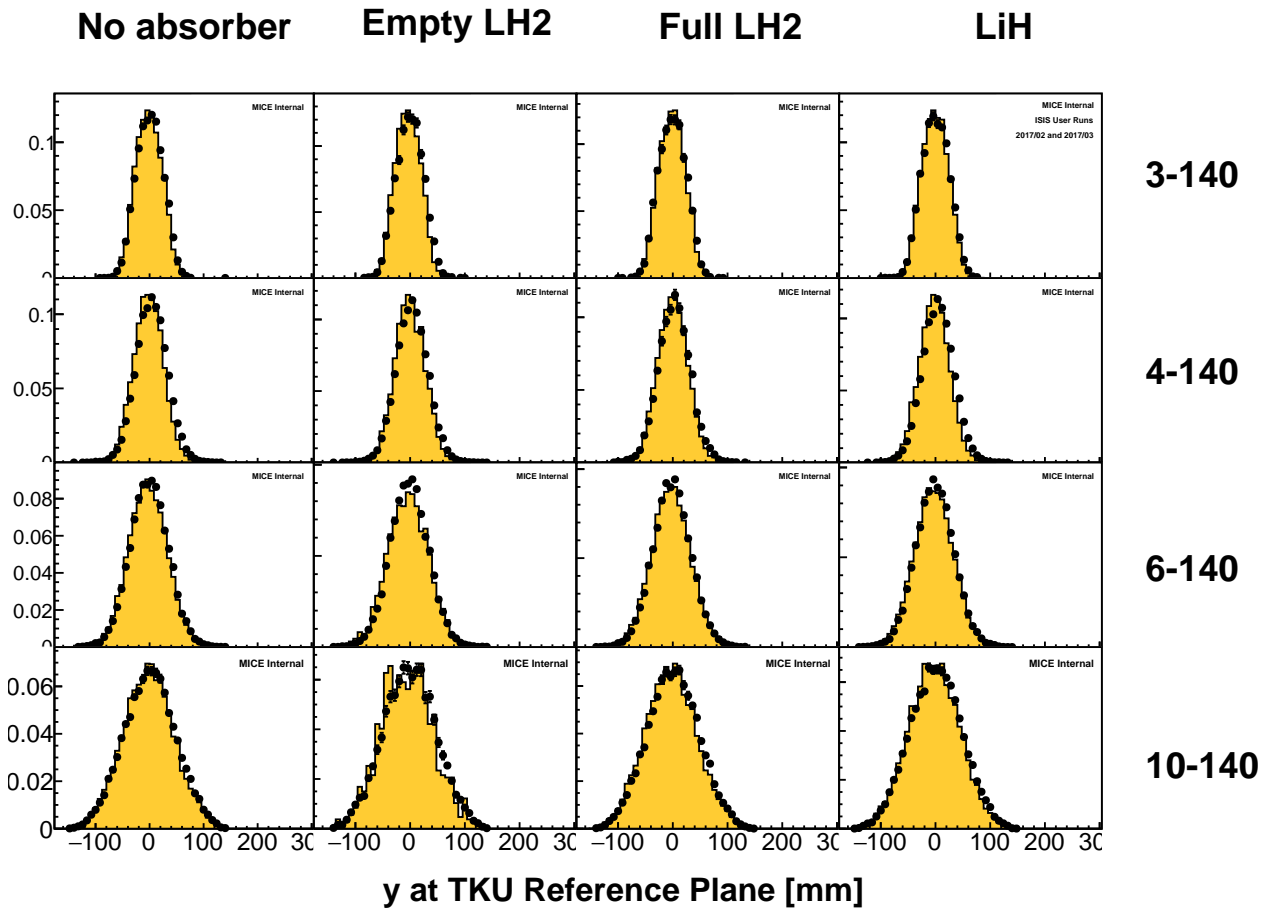
Figure 42: Vertical position distribution in TKU for all events in the upstream sample.
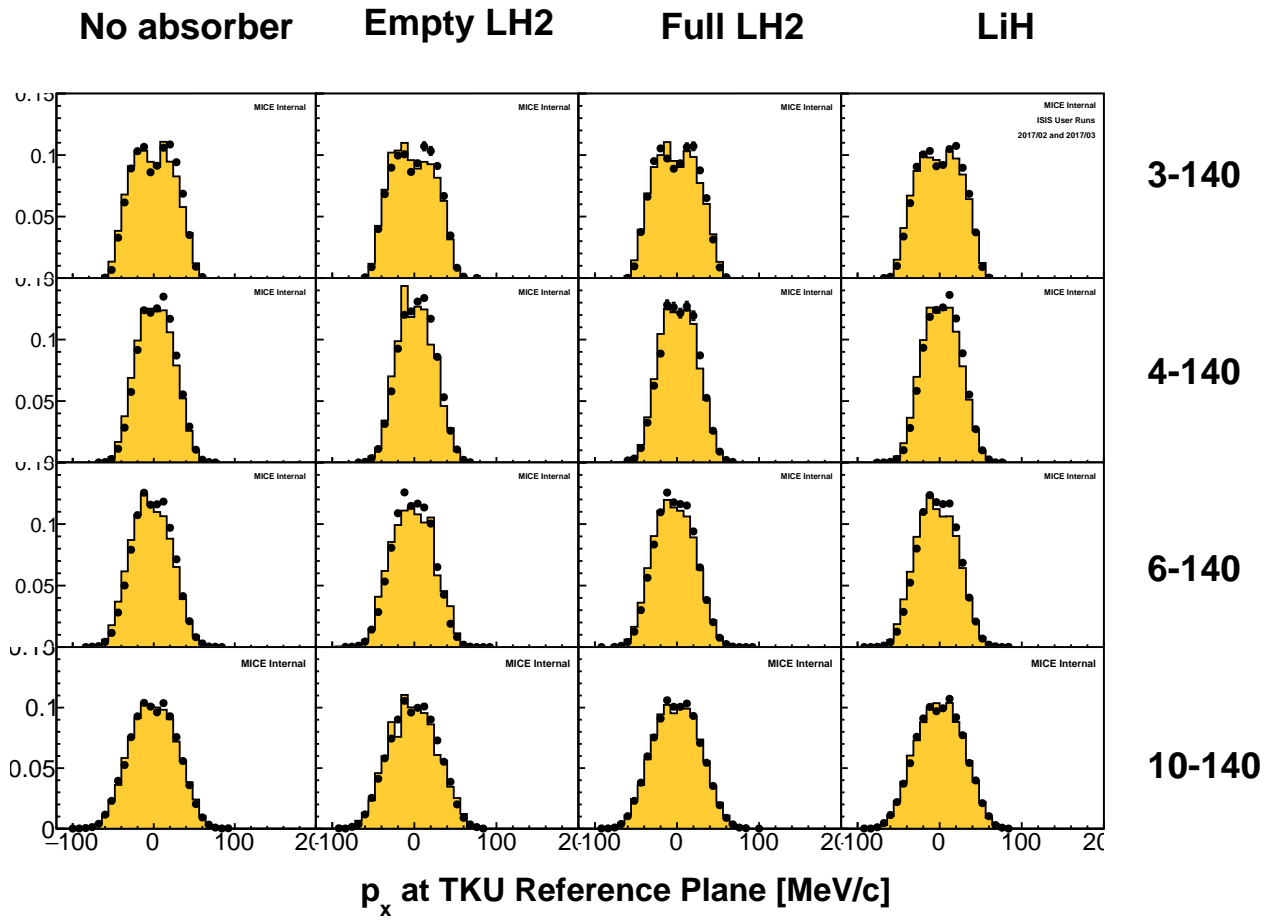
Figure 43: Horizontal momentum distribution in TKU for all events in the upstream sample.
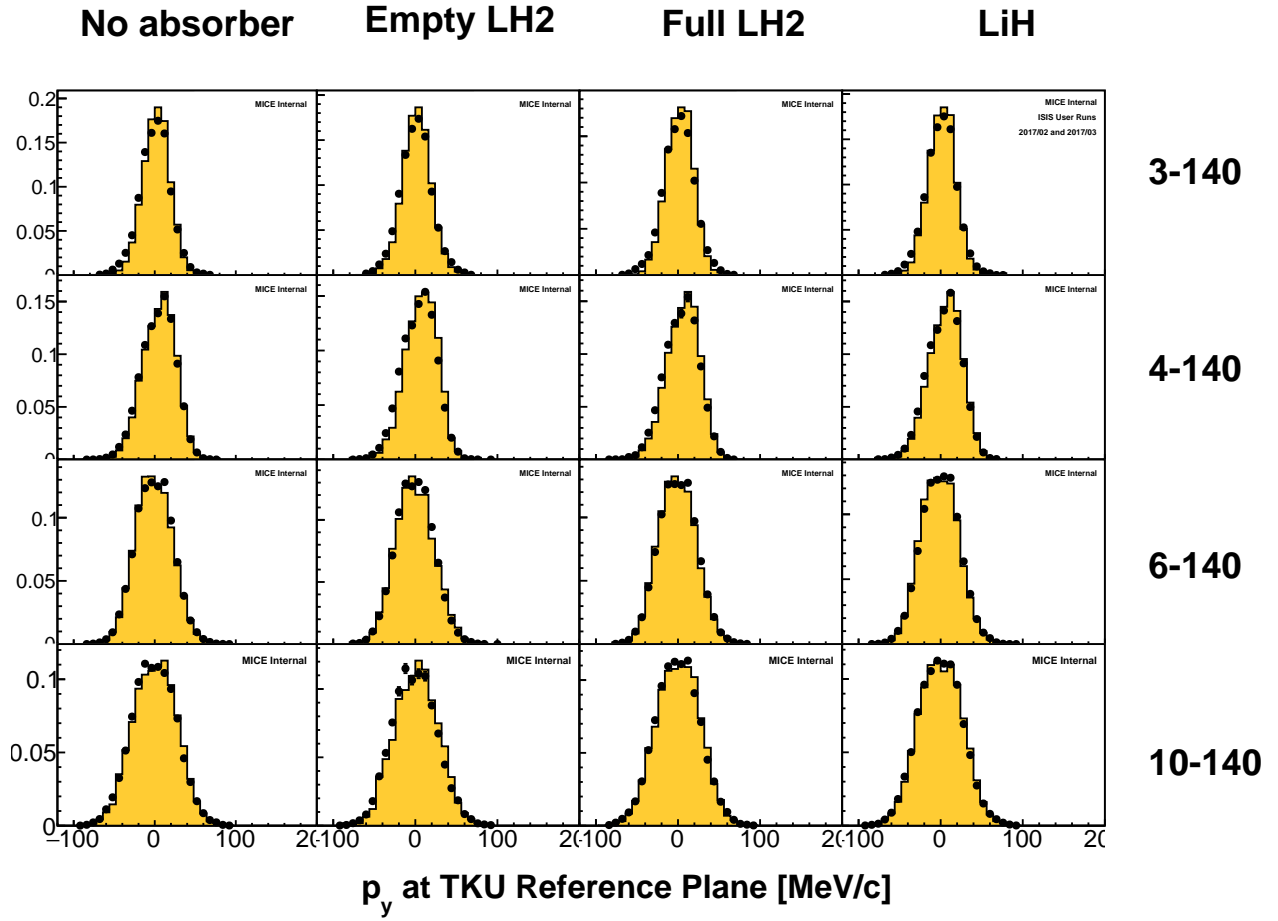
Figure 44: Vertical momentum distribution in TKU for all events in the upstream sample.
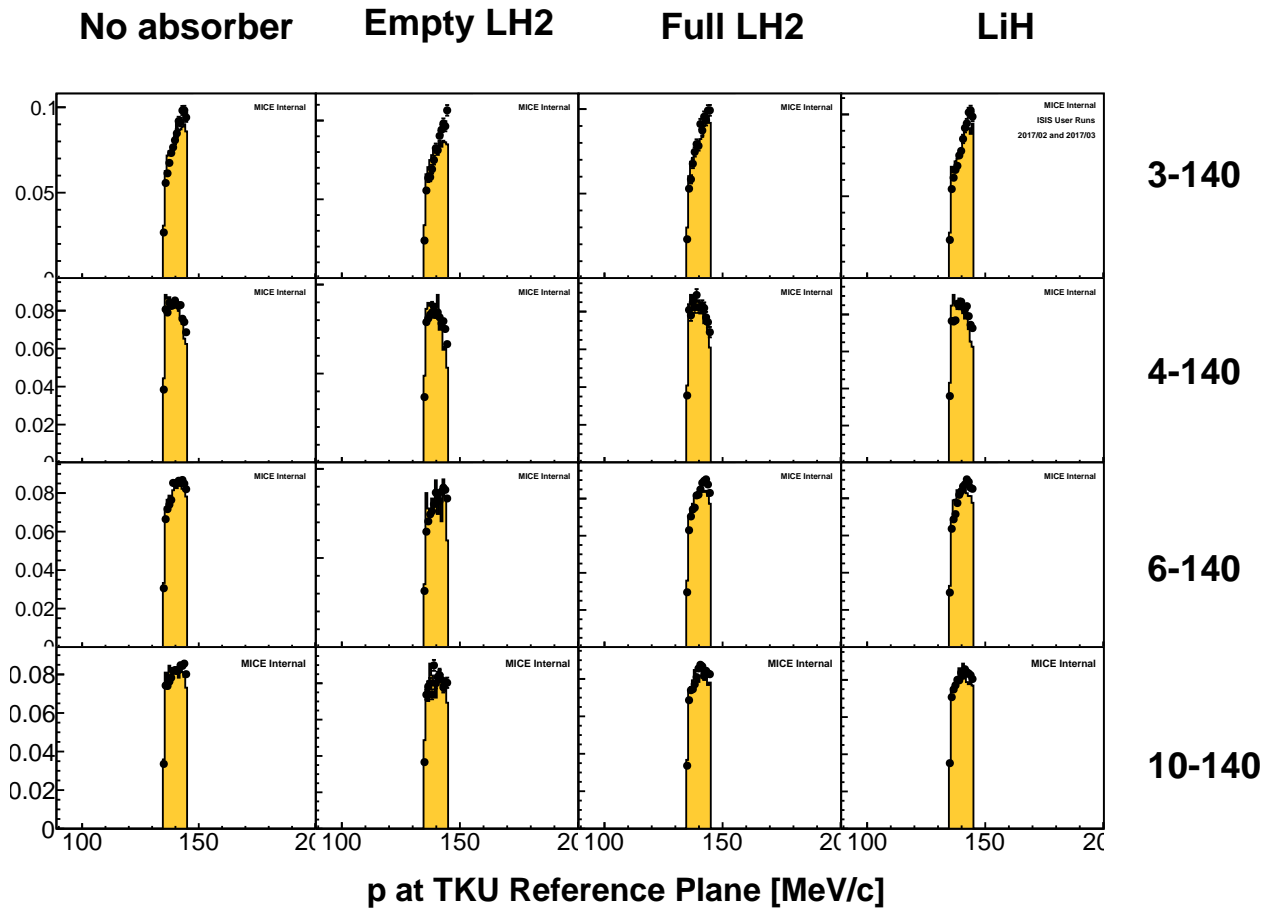
Figure 45: Total momentum distribution in TKU for all events in the upstream sample.

4.2 Magnets

The MICE cooling channel consists of 12 coils arranged in 3 magnet assemblies, SSU, FC and SSD. As shown in fig. 16 the magnetic field is exceptionally reproducible, even over the several weeks over which the data was taken.

4.3 Beam Transport

Bulk properties of the extrapolated beam are shown below. The measured points show the beam extrapolated by the global track matching routines to various z planes in the cooling channel geometry. The beam covariance matrix was calculated and various beam properties were drawn from the RMS ellipse. In the following plots, blue points show properties of the upstream sample extrapolated from TKU while red points show properties of the downstream sample extrapolated from TKD. The extrapolation routines do not take into account stochastic processes such as scattering, leading to a systematic discrepancy between the measured and extrapolated properties.

The 4-dimensional and 2-dimensional β functions are shown in fig. 46, 47 and 48. The 2-dimensional β functions are calculated using

$$\beta_i = Var(u_i)/\varepsilon_i \tag{5}$$

where $Var(u_i)$ is the variance of either x or y and ε_i is the corresponding 2-dimensional normalised RMS emittance. The 4-dimensional β function is calculated using

$$\beta_{4d} = \frac{Var(x) + Var(y)}{2\varepsilon_{4d}} \tag{6}$$

where ε_{4d} is the 4-dimensional normalised RMS emittance.

Some β-beating is evident in TKU, especially in the 3-140 configuration. This is expected; the Q789 triplet are not able to provide sufficient focussing to reproduce the low β functions required for adequate matching in SSU without the additional scattering provided by the diffuser. The higher emittance settings all reproduce similar optical performance. The 3-140 setting does yield a higher β in the absorber leading to proportionately less cooling as per equation 1. The higher β downstream of the focus coil may be associated with optical emittance growth.

The momentum loss in the absorber does affect the beam behaviour downstream of the absorber. The lower momentum results in a stronger focusing affect and larger phase advance, resulting in a focus (waist) in the region between M1D and M2D.

The extrapolated RMS beam width is shown in fig. 49 and 50. The largest beam radius is just downstream of the absorber for all the configurations. There was a fixed mounting flange for the liquid Hydrogen absorber installed at this location, even when the absorber was not installed. Interestingly, the 3 mm beam has rather a large beam radius owing to the beam transport issues outlined above. This may result in transmission losses despite the smaller beam emittance.
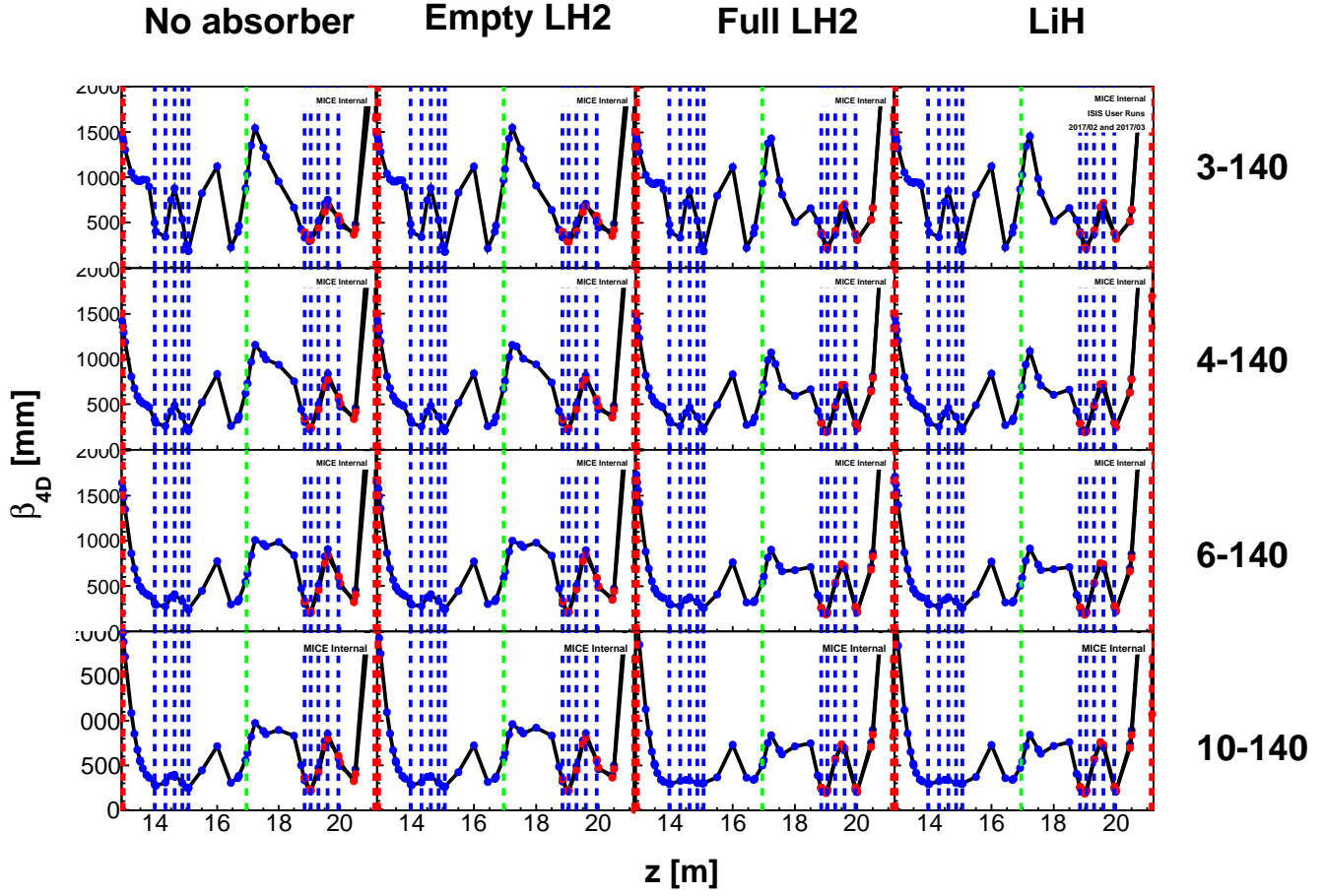
Figure 46: β_{4D} for events in the downstream sample, measured in TKU and extrapolated downstream (blue points) and events in TKD extrapolated downstream (red points). Red vertical lines indicate the position of ToF detectors, blue lines tracker stations and the green line represents the position of the absorber centre, when installed.
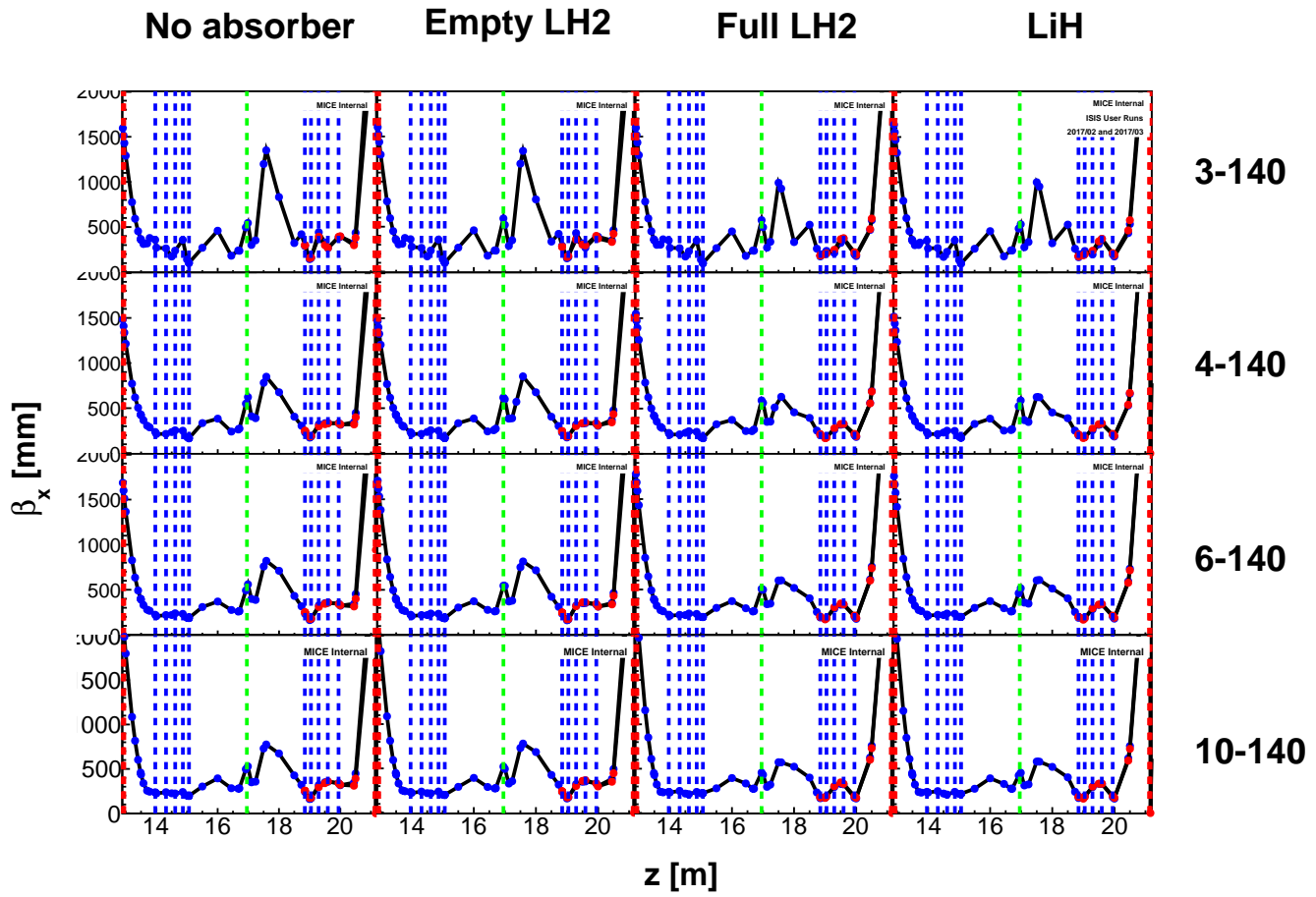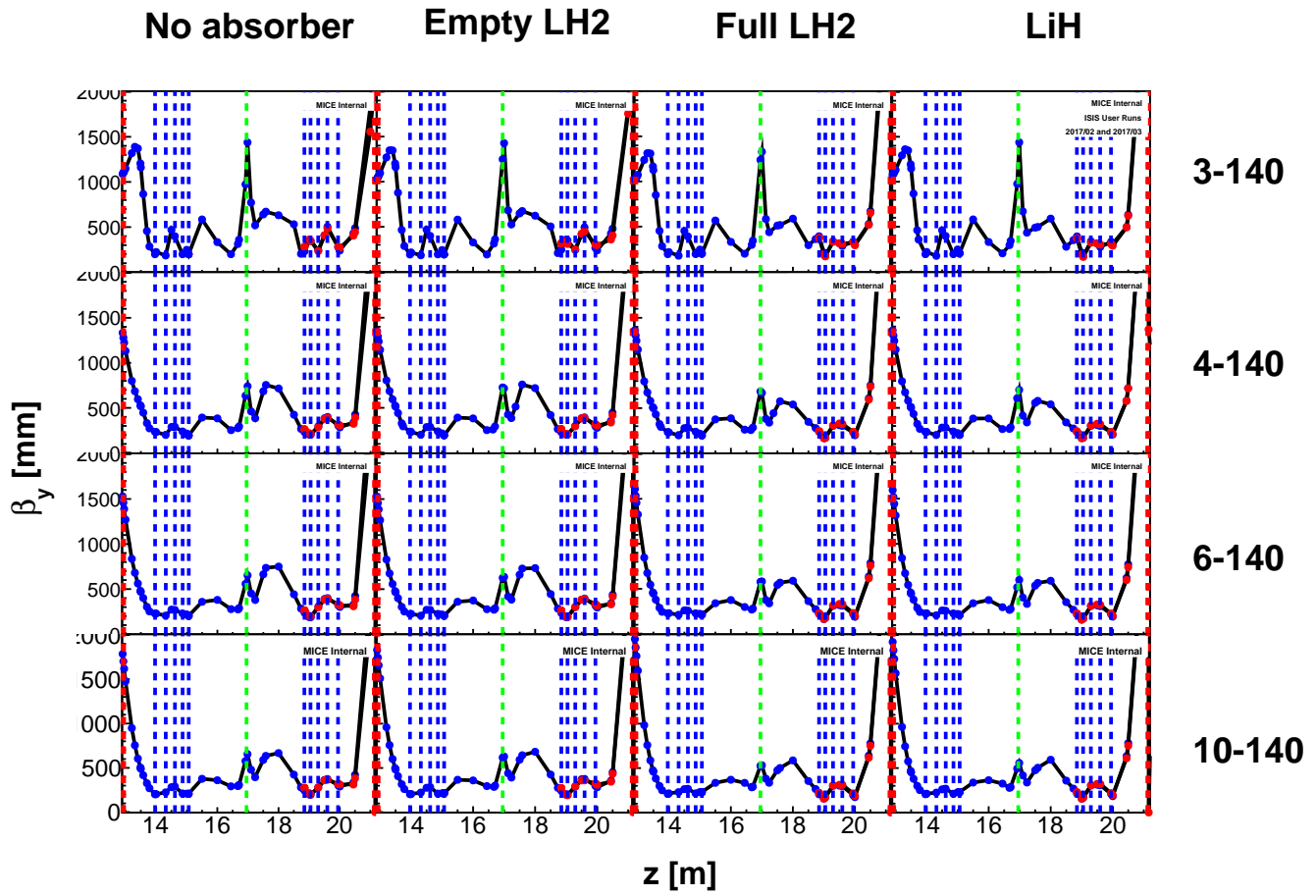
Figure 47: β_x of events in the downstream sample, measured in TKU and extrapolated downstream (blue points) and events in TKD extrapolated downstream (red points). Red vertical lines indicate the position of ToF detectors, blue lines tracker stations and the green line represents the position of the absorber centre, when installed.
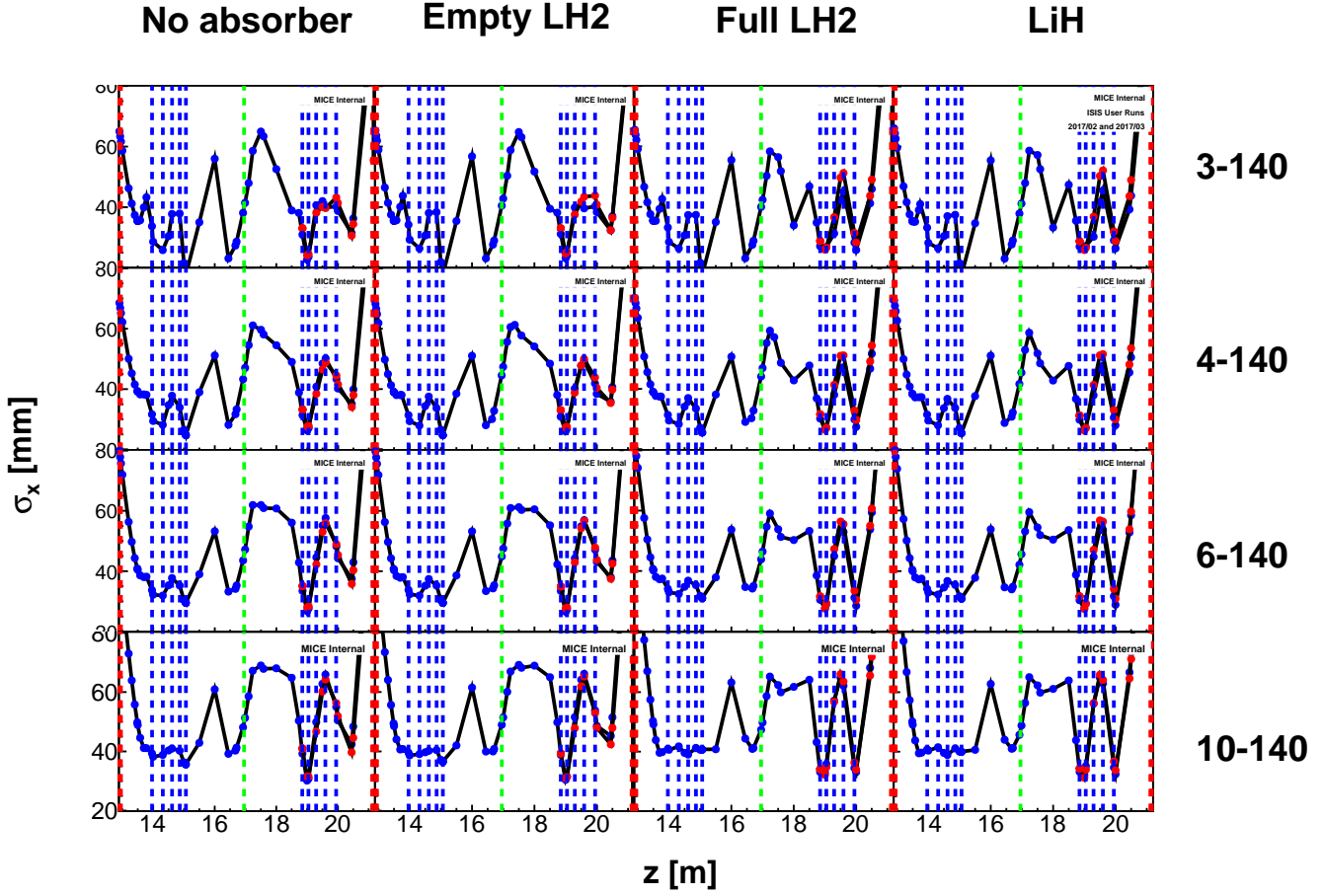
Figure 48: β_y of events in the downstream sample, measured in TKU and extrapolated downstream (blue points) and events in TKD extrapolated downstream (red points). Red vertical lines indicate the position of ToF detectors, blue lines tracker stations and the green line represents the position of the absorber centre, when installed.

Figure 49: Standard deviation of the vertical beam positions, σ_x, for events in the downstream sample, measured in TKU and extrapolated downstream (blue points) and events in TKD extrapolated downstream (red points). Red vertical lines indicate the position of ToF detectors, blue lines tracker stations and the green line represents the position of the absorber centre, when installed.
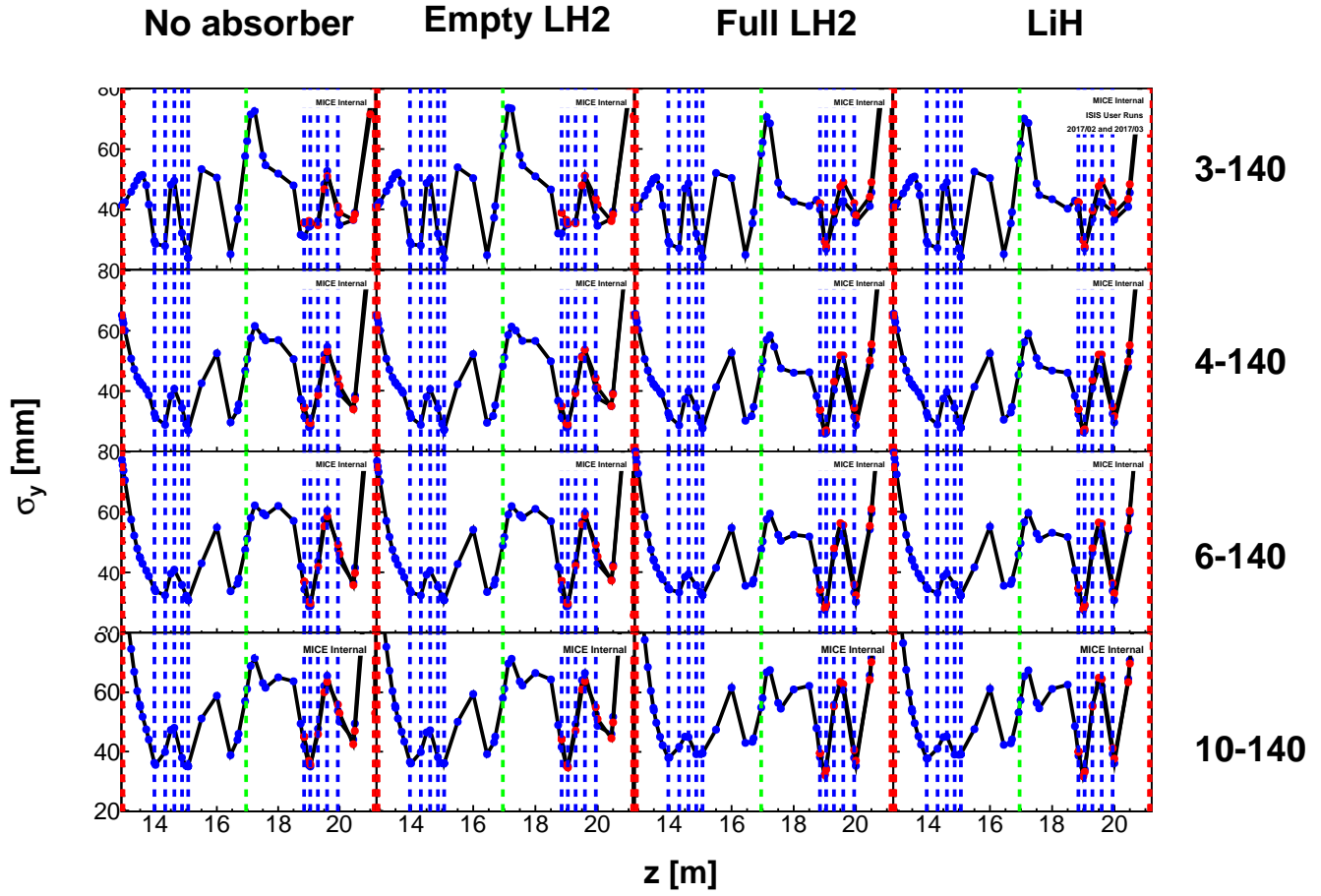
Figure 50: Standard deviation of the vertical beam positions, σ_y, for events in the downstream sample, measured in TKU and extrapolated downstream (blue points) and events in TKD extrapolated downstream (red points). Red vertical lines indicate the position of ToF detectors, blue lines tracker stations and the green line represents the position of the absorber centre, when installed.

4.4 Absorber

The main beam-based diagnostic of the absorber is the momentum loss of tracks as they pass through it. Where tracks pass through thicker or more dense materials, they lose more energy.

The momentum change between trackers is shown as a function of the radius of tracks extrapolated to the absorber midplane in fig. 51. For the no absorber case there is a small momentum change arising from the tracker Helium windows. When the lH2 windows were installed, there is a significant tendency for higher radius tracks to lose more momentum, owing to the thicker aluminium at higher radius. When the lH2 was filled, the higher energy loss from aluminium appears to be offset due to the thickness of the hydrogen itself. The momentum change in the lithium hydride is essentially independent of radius, as expected from the cylindrical shape.

The momentum change in the absorber is shown as a function of the height of tracks extrapolated to the absorber midplane in fig. 52. There is no significant vertical correlation, beyond those noted above and the energy loss appears to be symmetric about the beamline.
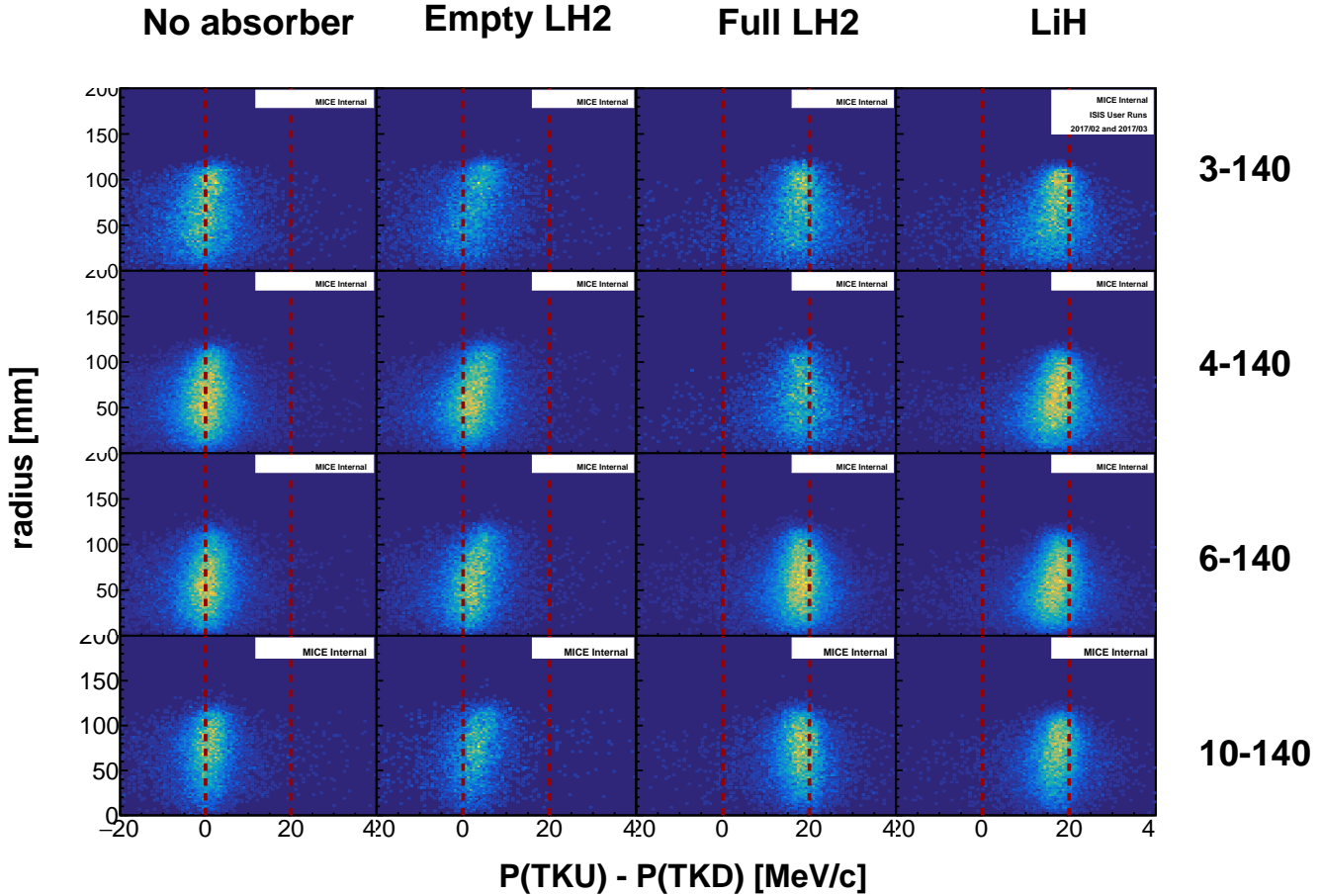

Figure 51: Change in momentum between TKU and TKD as a function of the extrapolated track's distance from the beam axis at the absorber midplane. Vertical lines have been drawn at 0 and 20 MeV/c.
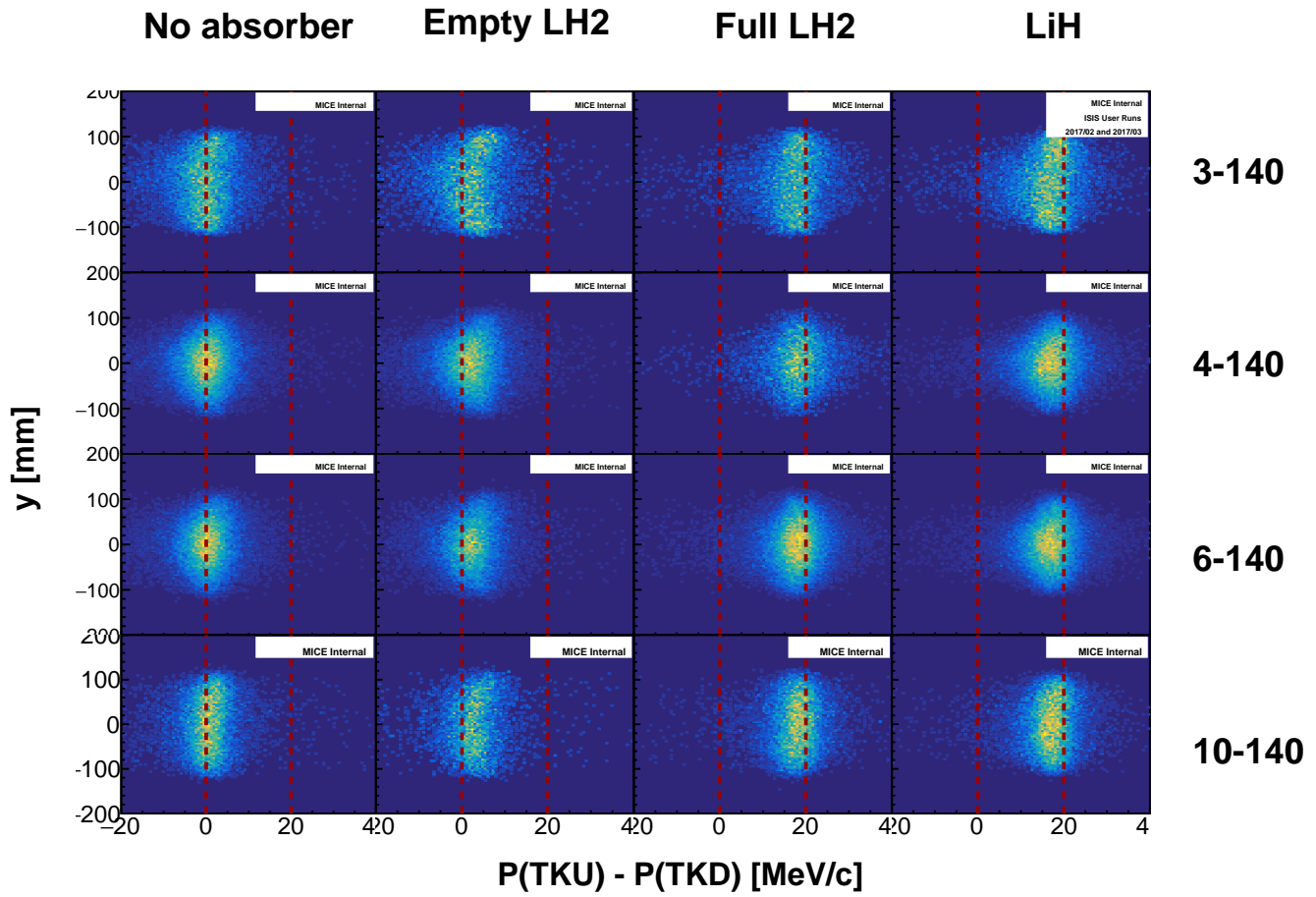
Figure 52: Change in momentum between TKU and TKD as a function of the extrapolated track's height at the absorber midplane. Vertical lines have been drawn at 0 and 20 MeV/c.
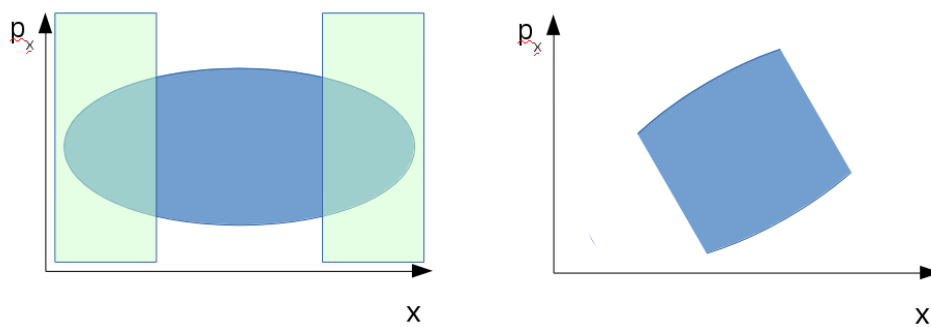

Figure 53: Schematic showing a beam ellipse scraped and then subsequently rotated in (x, p_x) space by a focussing system. The resultant distribution will look quite non-Gaussian, potentially with the observed non-Gaussian shoulders depending on the degree of rotation.

4.5   Output Beam

The position distribution of the downstream beam sample measured in TKD is shown in fig. 54 and fig. 55. The 3-140 beam has significant shoulders. These can arise due to scraping, for example where the beam gets rather large around station 4 of TKD, as shown in 53. The solenoid field between station 1 and station 4 leads to a partial rotation of the region occupied by the scraped particles, both between horizontal and vertical spaces and between position and momentum spaces. In general reasonable agreement is demonstrated between simulation and data.

The transverse and total momenta in TKD is shown in fig. 56, 57 and 58. The transverse distributions are reproduced in simulation with good agreement. The simulation shows more momentum loss than the data; this was also observed in the momentum residual plot fig. 37. The additional momentum loss in simulation is especially pronounced for the lithium hydride and empty absorber cases.
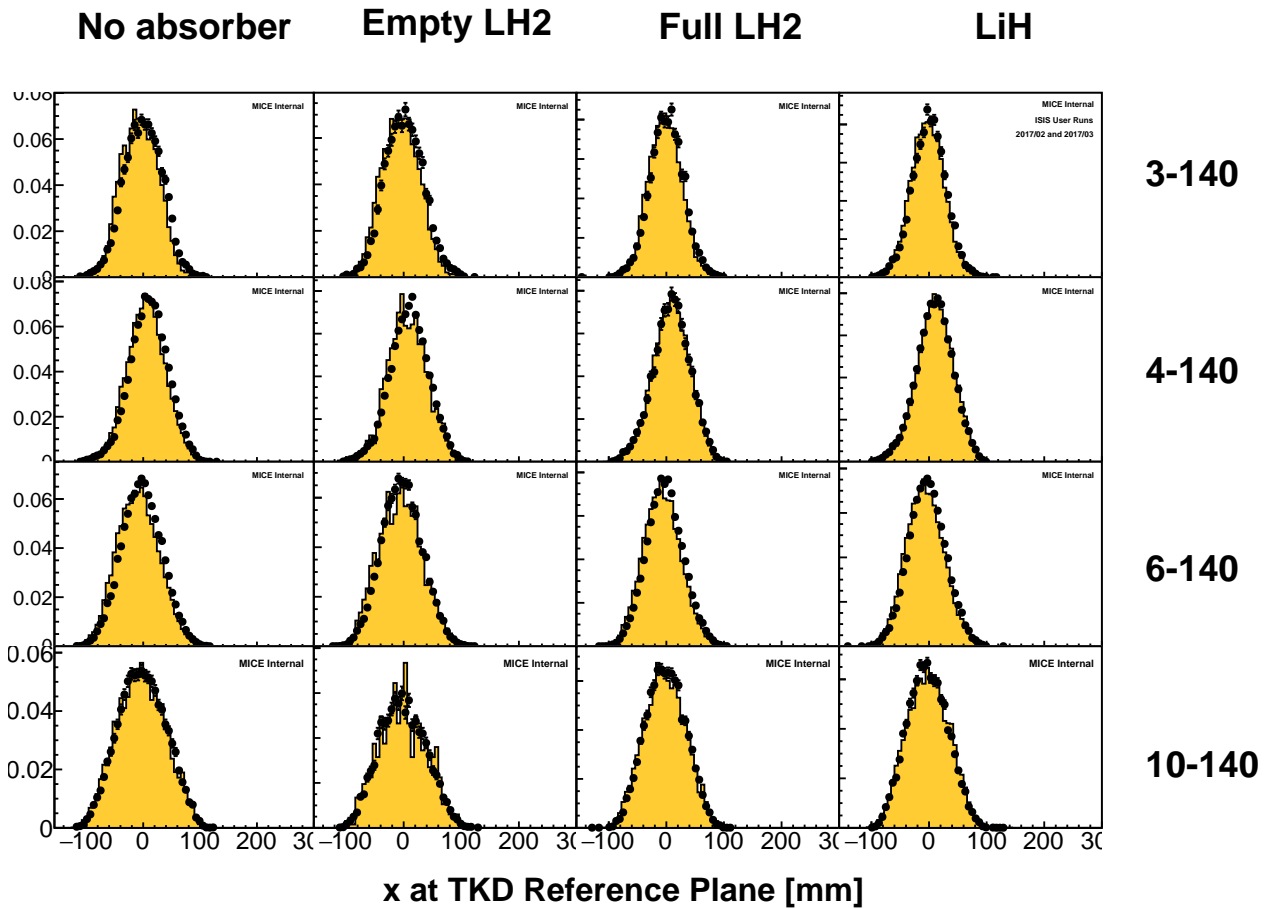

Figure 54: Horizontal position distribution in TKD for all events in the downstream sample.
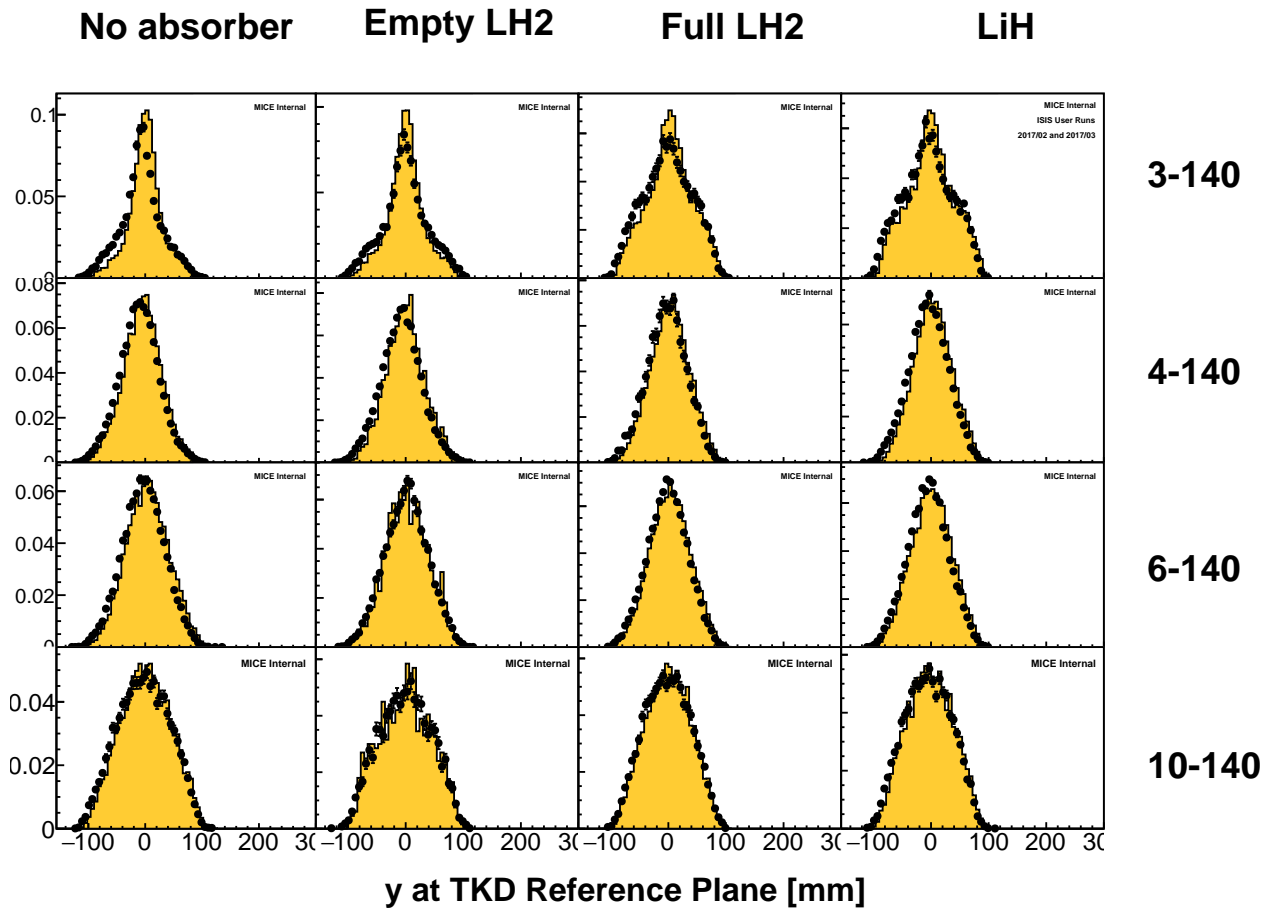
Figure 55: Vertical position distribution in TKD for all events in the downstream sample.
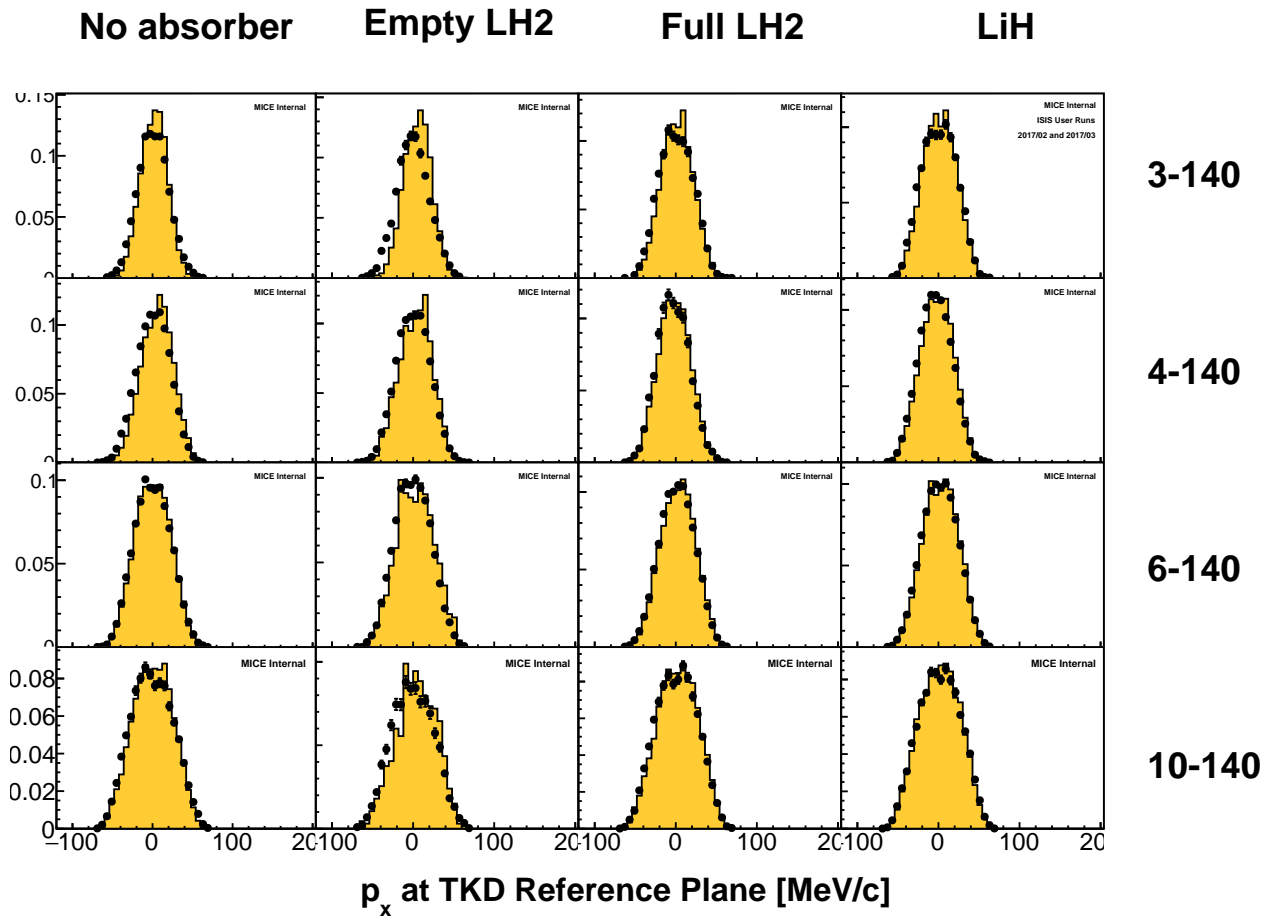
Figure 56: Horizontal momentum distribution in TKD for all events in the downstream sample.
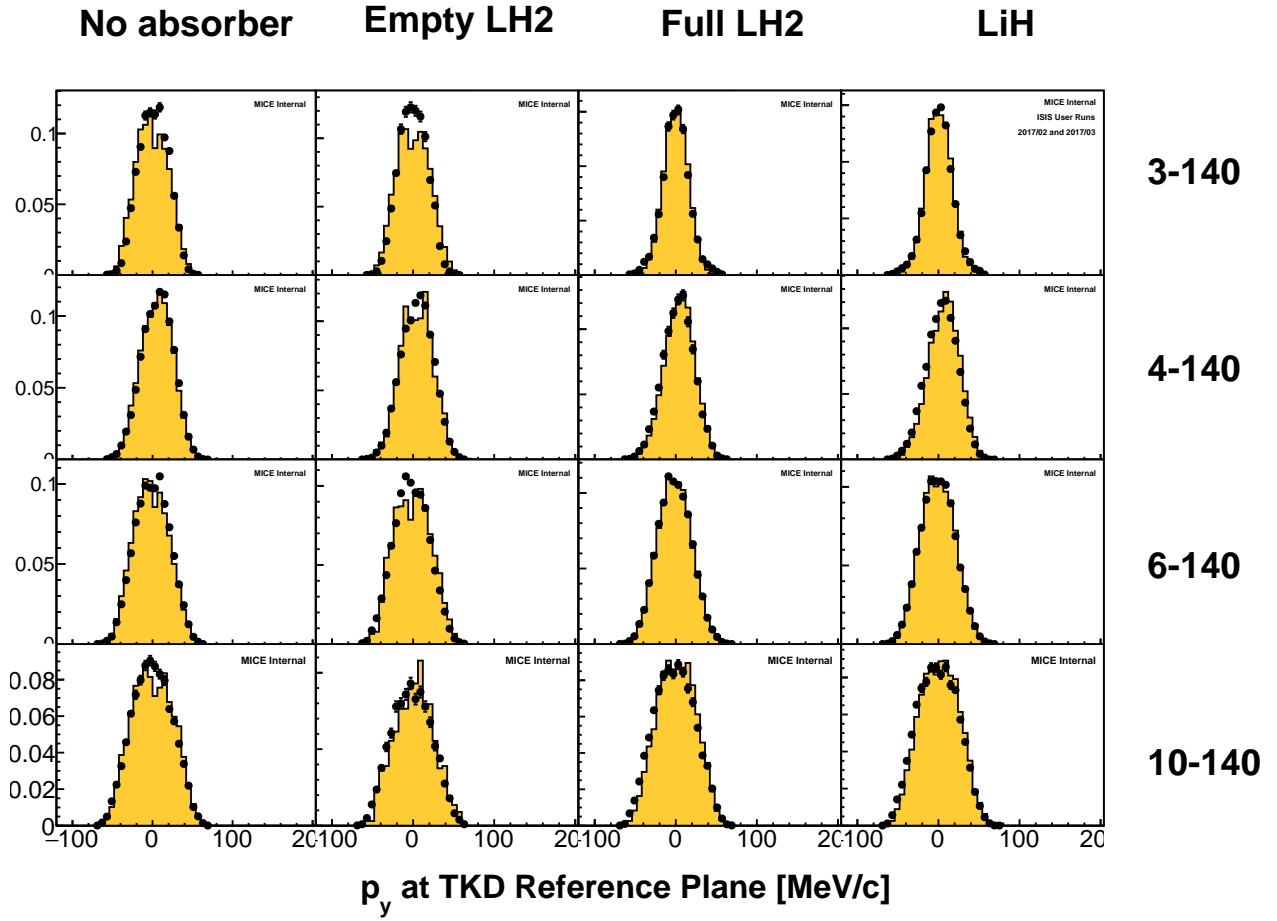
Figure 57: Vertical momentum distribution in TKD for all events in the downstream sample.
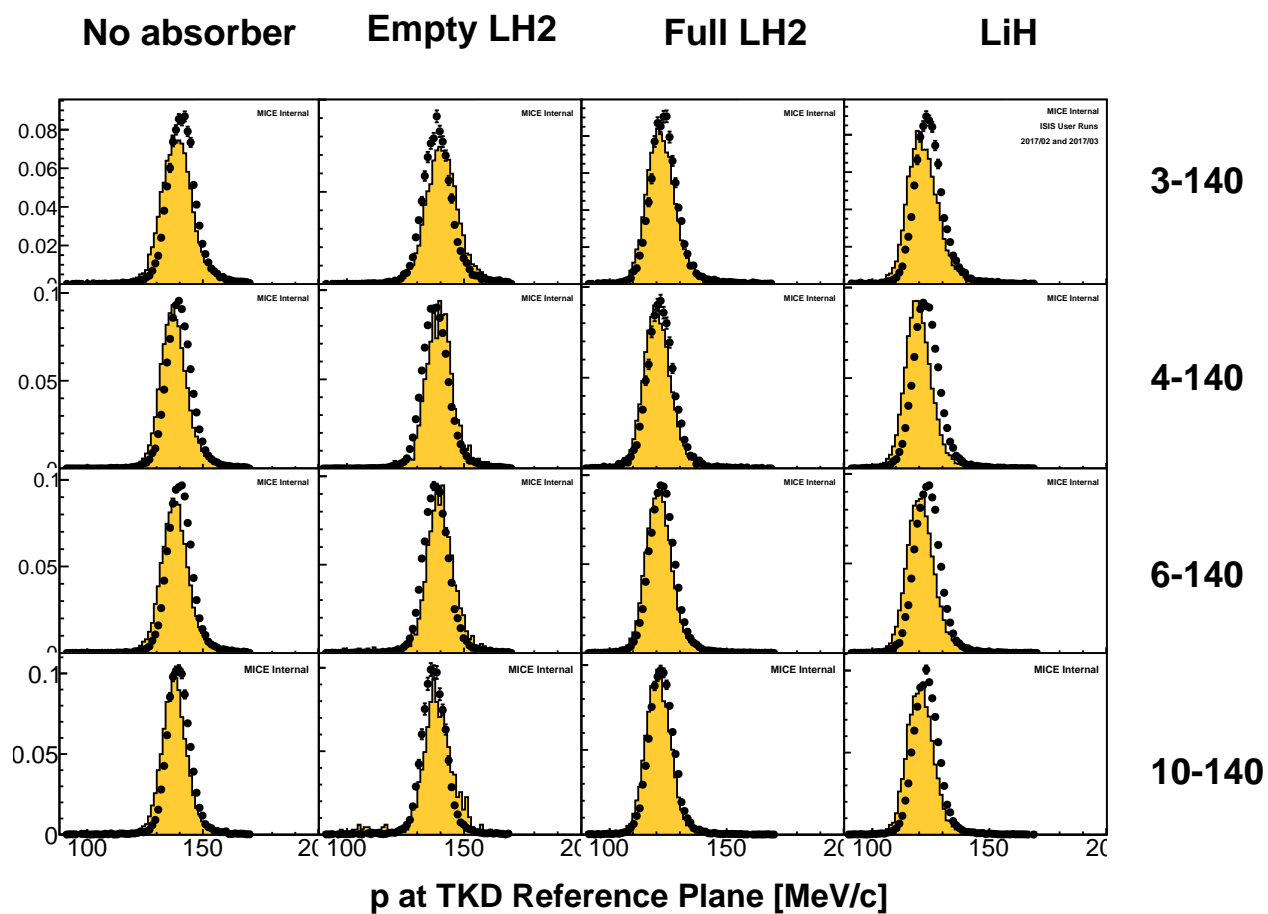
Figure 58: Total momentum distribution in TKD for all events in the downstream sample.

5 Calculation of Amplitude

Having validated the performance of the cooling channel equipment the main results of the analysis are now presented. In this note, cooling is characterised by the change in particle amplitude.

For a beam with elliptical phase space contours, the 4D amplitude of the ith particle is defined by

$$A_i = \epsilon_n (\mathbf{u}_i - <\mathbf{u}>)^T \mathbf{V^{-1}} (\mathbf{u}_i - <\mathbf{u}>) \tag{7}$$

where ϵ_n is the 4D normalised emittance, $\mathbf{u}$ is the 4D phase space vector (x, p_x, y, p_y), $<\mathbf{u}>$ is the mean of the 4D phase space vector and $\mathbf{V}$ is the matrix of covariances with elements $v_{ij} = <u_i u_j> - <u_i u_j>$. When A_i is $1/\varepsilon_n$, eq. 7 also defines the locus of points in space u_i that make up the RMS hyper-ellipsoid corresponding to the covariance matrix $\mathbf{V}$.

It can be shown that, in the linear approximation, A_i is conserved [21]. For a so-called 'matched' beam, A_i is on-average conserved even in the non-linear approximation, below some dynamic aperture. This is because muons follow closed contours in phase space. A 'matched' beam is one where the curves in phase space are uniformly filled, so that if a muon moves to a portion of the curve with a higher amplitude, another muon will move to replace it at the lower amplitude. On average, the amplitude does not change.

Following the failure of coil M2D [22], it was not possible to find an optics that had both a matched beam in SSU and the good transmission and tight focussing necessary to observe cooling. In order to make the required measurements, the optics team sacrificed the matched beam requirement and accepted worse beam transmission. As a consequence, a modified amplitude is defined that explicitly rejects the effects of tails. The basic algorithm is

```
while events in sample {
    calculate amplitudes
    remove highest amplitude event
    update covariance matrix
}
```

This basic algorithm is biased; the calculation of the covariance matrix uses the same sample as the amplitude calculation, so the covariance matrix will be biased by statistical deviations in the sample. In order to avoid this bias, the sample is split into two - a 'ref'(erence) sample, used to calculate the covariance matrix, and a 'test' sample, used to calculate the amplitudes. The 'ref' and 'test' samples are swapped so that no statistical power is lost from the analysis.

The algorithm is also rather CPU intensive; the amplitude calculation has to be repeated for every event, every time an event is removed, so CPU time goes as $O(N^2)$. Rather than repeat the amplitude calculation for every event, the data can be binned by amplitude. Events are removed per-bin; the amplitudes are recalculated; and the process is repeated until no events are removed from a given bin. The CPU time is observed to go as $O(log(N))$. Further optimisation may be possible.

The full algorithm is outlined below.

78

```
Split data into equal size ref_sample and test_sample
for cut_bin in reversed(ref_sample_bins) {
    calculate covariance matrix using ref_sample
    calculate amplitudes in ref_sample and bin
    do until no events are removed {
        loop over ref_sample {
            rebin ref_sample events
            if new bin >= cut_bin {
                remove events from ref_sample
            }
            update covariance matrix
        }
    }
    loop over test_sample {
        rebin test_sample events using covariance matrix previously calculated
        if new_bin >= cut_bin {
            remove events from test_sample
            store the amplitude of removed events
        }
    }
}
swap the ref_bin and test_bin designation and repeat
```

A test analysis is shown in fig. 59, together with a 2D section of some of the 4D RMS hyper-ellipsoids used to calculate the amplitude. Because the ellipses are calculated for each subsample, there are two series (rose-tinted and green-tinted). The total sample size was 10000 events.

A double peaked distribution is used to illustrate the resolving power of the technique. As the centre of the beam is approached, the ellipse calculation successfully centres on the brighter peak. This yields a double-peaked amplitude distribution.

5.1 Effect of Detector Performance

The resolution, inefficiency and impurity of the detectors will lead to inaccuracies in the measured amplitude distribution. Tracker resolution leads to movement of events from one bin to another due to changes in the measured phase space variables from the actual position or momentum of the particle. Impurity and inefficiency leads to an artificial enhancement or depletion of a particular region of phase space, which is assumed to deplete each bin without causing any bin migrations.

5.1.1 Simulation of Detector Effects

The detector simulation has been used to estimate the magnitude of these effects and make a correction. A hybrid simulation was devised in order to provide a sufficiently large sample of events that statistical fluctuations in the sample did not dominate over the relatively small effect of bin migrations due to the detectors. The upstream data sample, taken at TKU station 5, was smeared using a KDE routine [23] and then the smeared distribution was sampled in order to provide a large number of events (approximately 10^6 muons). All events
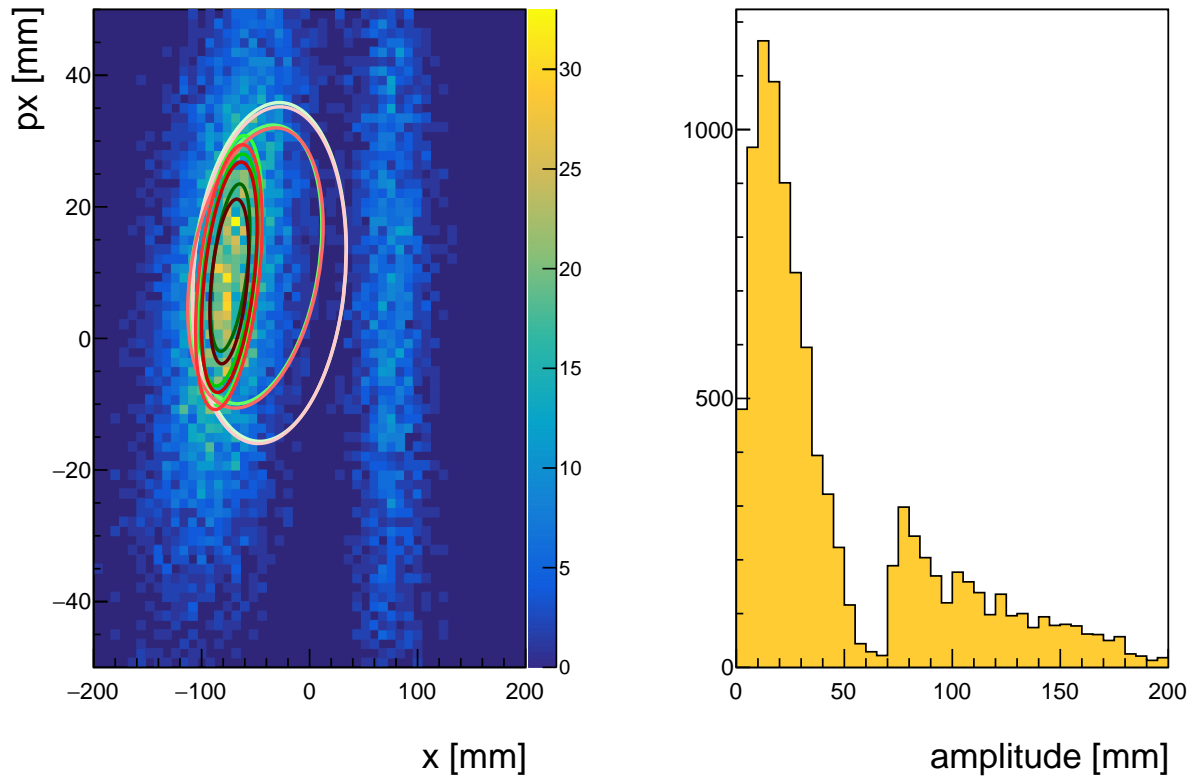
Figure 59: Test amplitude distribution: double peaked distribution with ellipses used for calculation of **V** superimposed (left); and calculated amplitude distribution (right).

were assumed to be muons in station 5, which is consistent with the simulation and data. This sample was tracked from TKU through to TKD.

Several subsamples were drawn from these muons. The upstream reconstructed sample had the following requirements:

- exactly one TKU track;
- TKU χ^2 per degree of freedom less than 4;
- estimated radial excursion of the reconstructed track from the beam axis in TKU less than 150 mm; and
- TKU momentum between 135 and 145 MeV/c at the reference plane.

The downstream reconstructed sample had the following requirements:

- in the upstream reconstructed sample;
- exactly one TKD track;
- TKD χ^2 per degree of freedom less than 4;
- estimated radial excursion of the reconstructed track from the beam axis in TKD less than 150 mm; and
- TKD momentum between 90 and 170 MeV/c at the reference plane.

In order to estimate inefficiency and purity, 'truth' samples were considered, corresponding to the events that should have been reconstructed. The upstream truth sample had the following requirements:

- in the upstream reconstructed sample;
- MC truth muon in all 5 TKU stations; and
- estimated radial excursion of the truth track from the beam axis in TKU less than 150 mm; and

The downstream truth sample had the following requirements:

- in the upstream truth sample;
- MC truth muon in all 5 TKD stations;
- estimated radial excursion of the truth track from the beam axis in TKD less than 150 mm; and
- TKD true momentum between 90 and 170 MeV/c at the reference plane.

Each muon was recorded with its truth phase space variables (x, p_x, y, p_y) and, if it was reconstructed, its reconstructed phase space variables, both recorded at the tracker reference planes. The number of events surviving each cut is listed in tables 17, 18, 19 and 20.

Table 17: The upstream reconstructed simulated sample is listed.

	Simulated 2017-2.7 3-140 lH2 empty Systematics tku base	Simulated 2017-2.7 4-140 lH2 empty Systematics tku base	Simulated 2017-2.7 6-140 lH2 empty Systematics tku base	Simulated 2017-2.7 10-140 lH2 empty Systematics tku base
All Events	1095790	1095787	1095774	1095724
One track in TKU	1044432	1033482	1013371	958894
TKU χ^2/dof	1024814	1013368	994331	941404
TKU fiducial volume	1024334	1013136	993833	931880
TKU momentum	717107	704300	699576	649264
Upstream Sample	717107	704300	699576	649264

Table 18: The downstream reconstructed simulated sample is listed.

	Simulated 2017-2.7 3-140 lH2 empty Systematics tku base	Simulated 2017-2.7 4-140 lH2 empty Systematics tku base	Simulated 2017-2.7 6-140 lH2 empty Systematics tku base	Simulated 2017-2.7 10-140 lH2 empty Systematics tku base
Upstream Sample	717107	704300	699576	649264
One track in TKD	658809	660413	630981	491533
TKD χ^2/dof	636698	644689	611802	475933
TKD fiducial volume	628695	630782	579498	423850
TKD momentum	615429	623630	571445	418220
Downstream Sample	615429	623630	571445	418220

Table 19: The extrapolated reconstructed simulated sample is listed.

	Simulated 2017-2.7 3-140 lH2 empty Systematics tku base	Simulated 2017-2.7 4-140 lH2 empty Systematics tku base	Simulated 2017-2.7 6-140 lH2 empty Systematics tku base	Simulated 2017-2.7 10-140 lH2 empty Systematics tku base
Upstream Sample	717107	704300	699576	649264
Muon in all TKU stations	717107	704300	699576	649264
TKU true fiducial volume	717106	704292	699565	648924
Upstream MC True Sample	717106	704292	699565	648924

Table 20: The upstream truth simulated sample is listed.

	Simulated 2017-2.7 3-140 lH2 empty Systematics tku base	Simulated 2017-2.7 4-140 lH2 empty Systematics tku base	Simulated 2017-2.7 6-140 lH2 empty Systematics tku base	Simulated 2017-2.7 10-140 lH2 empty Systematics tku base
Upstream MC True Sample	717106	704292	699565	648924
Muon in all TKD stations	669924	669547	646052	513525
TKD true fiducial volume	660024	653147	605786	446155
TKD true momentum	659526	652419	604340	442888
Downstream MC True Sample	659526	652419	604340	442888

5.1.2 Calculation of Correction

Several amplitude distributions were generated from these samples, with N_i events in the ith bin:

- $N_i^{t|t}$: number of events in the ith bin of the amplitude $A^{t|t}$ calculated from the truth sample using truth phase space variables;
- $N_i^{r|t}$: number of events in the ith bin of the amplitude $A^{r|t}$ calculated from the reconstructed sample using truth phase space variables; and
- $N_i^{r|r}$: number of events in the ith bin of the amplitude $A^{r|r}$ calculated from the reconstructed sample using reconstructed phase space variables.

Each of these distributions was calculated in both the upstream region and the downstream region. A vector $\mathbf{E}$ and matrix $\mathbf{S}$ are defined relating the number of events in each sample according to

$$N_i^{r|t} = \sum_j S_{ij} N_j^{r|r} \tag{8}$$

$$N_i^{t|t} = E_i N_i^{r|t} \tag{9}$$

so that

$$N_i^{t|t} = E_i \sum_j S_{ij} N_j^{r|r}. \tag{10}$$

Then

$$E_i = \frac{N_i^{t|t}}{N_i^{r|t}}. \tag{11}$$

Q_{ij} is defined as the number of events in the ith bin of the distribution of $A^{r|r}$ and the jth bin of the distribution of $A^{r|t}$. Then

$$\sum_j Q_{ij} = N_i^{r|t} \tag{12}$$

so

$$S_{ij} = \frac{Q_{ij}}{N_j^{r|r}}. \tag{13}$$

$\mathbf{S}$ and $\mathbf{E}$ are useful quantities because for the same RMS ellipse, they are independent of the actual number of events in each amplitude bin.

5.1.3 Migration Matrix Correction

The corrections have been calculated for 3-140, 4-140, 6-140 and 10-140 beams with no absorber. Deviations in the corrections in TKD may exist when an absorber is installed due to the lower beam momentum but these are assumed to be small.

The full migration matrix $\mathbf{S}$ is shown in fig. 60 for the upstream tracker and fig. 61 for the downstream tracker. It is noted that while bin migrations are relatively common, migrations through more than one bin are rather rare.

The probability of an event being reconstructed in the same amplitude bin as it was found in truth, corresponding to the diagonal elements of $\mathbf{S}$, is shown in fig. 62 and 63 for upstream and downstream detectors respectively. The correction is significant and becomes larger for higher amplitudes. There is a significant cusp at 15 mm amplitude, visible in all upstream and downstream samples but especially pronounced in the 10-140 sample.
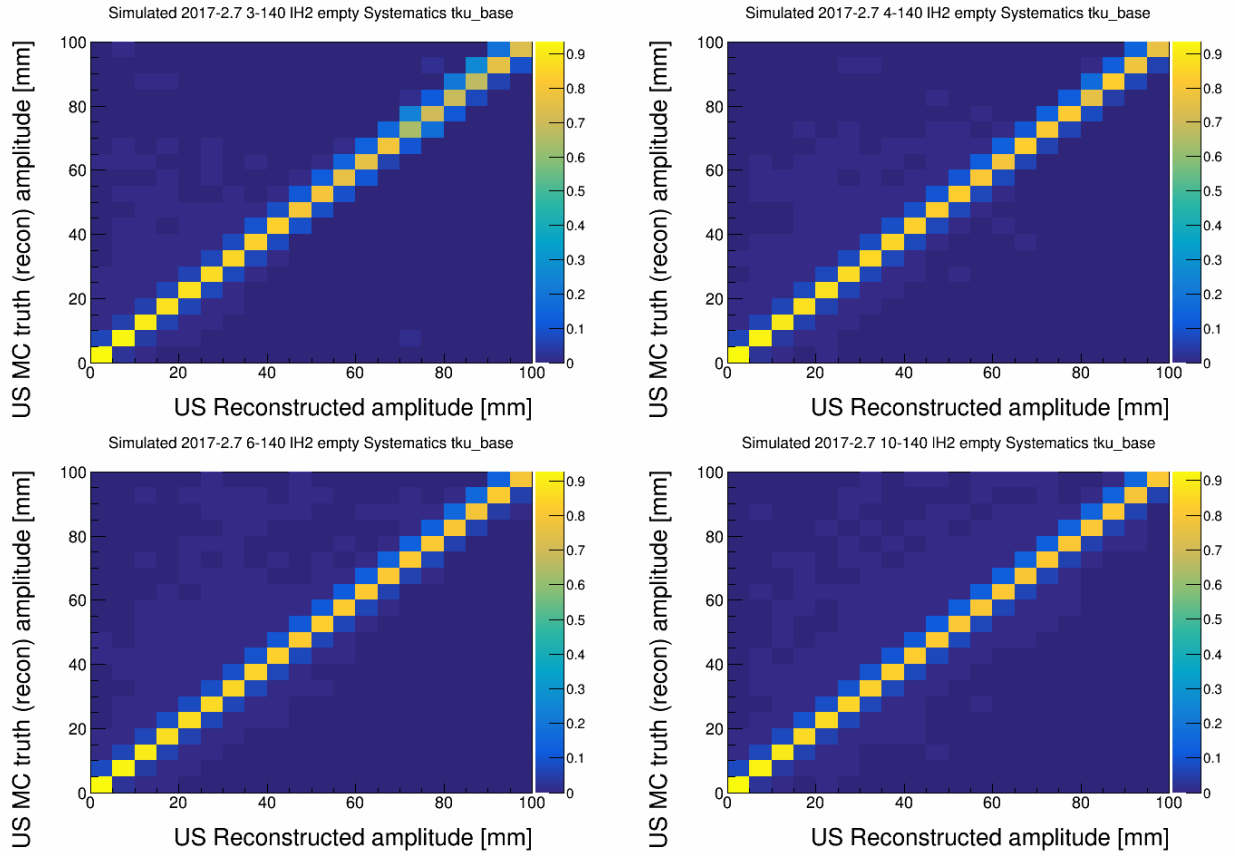
Figure 60: Probability of TKU reconstruction in a certain amplitude bin compared to the true amplitude bin for 3-140 (top left); 4-140 (top right); 6-140 (bottom left) and 10-140 (bottom right) configurations.

5.1.4 Inefficiency Correction

The inefficiency in TKU is less than $O(10^{-3})$, arising due to events that are reconstructed in the TKU fiducial volume but whose true trajectory falls outside the TKU fiducial volume. No correction is made in TKU.

There is a notable efficiency correction in TKD as shown in fig. 64. The correction is large at low amplitudes, where inefficiency arises as scattering can be dominant over curvature of the track for tracks with low transverse momentum. There is also a large correction at high amplitudes, where inefficiency can arise due to deformation of the helix from field non-uniformity near to the end coils.

5.2 Uncertainties

Measurement uncertainty is dominated by statistical uncertainty and uncertainty in the correction. The estimation of this uncertainty is described below.

5.2.1 Statistical uncertainty

In this note, the change in emittance of a sample of muons is studied. Statistical uncertainty in the change in emittance arises due to finite sampling of the scattering and straggling distribution in the absorber. Explicitly, the uncertainty arising due to sampling of the input beam distribution is not considered in this note. There is no
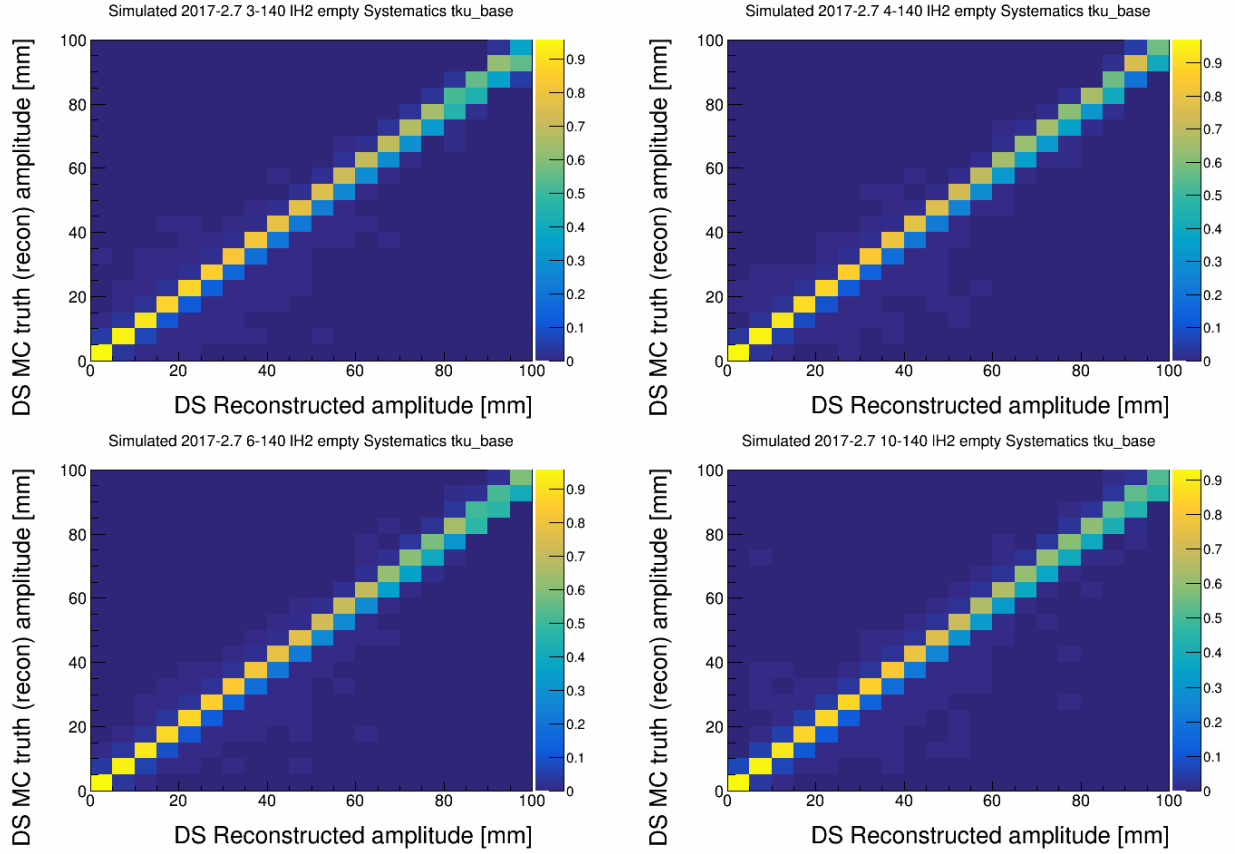
Figure 61: Probability of TKD reconstruction in a certain amplitude bin compared to the true amplitude bin for 3-140 (top left); 4-140 (top right); 6-140 (bottom left) and 10-140 (bottom right) configurations.

statistical uncertainty in the upstream distribution, because it is exactly that set of events that have been selected for analysis.

The statistical uncertainty in the downstream distribution is taken by considering the number of events in the ith bin upstream and the jth bin downstream, $N_{ij}^{us \cup ds}$. The number of events is taken to follow a binomial distribution where the number of trials is taken as the number of events in the ith bin upstream, N_i^{us} and the probability of success is estimated as the ratio $N_{ij}^{us \cup ds} / N_i^{us}$. The uncertainty in $N_{ij}^{us \cup ds}$ is given by the width of the 68% confidence interval and the uncertainty in the downstream bin N_j^{us} is given by summing uncertainties in $N_{ij}^{us \cup ds}$ over all upstream bins. Summation is done by adding in quadrature.

The statistical uncertainty in the cumulative distribution is found by adding in quadrature the error on each bin in the probability distribution that contributes to a given cumulative bin. The statistical error in the ratio distributions is found by adding in quadrature the upstream and downstream error, normalised to the number of events in each bin.

Only a subset of the full dataset is included in this analysis. More data can reduce the statistical uncertainties.

5.2.2 Correction Uncertainty

The correction procedure outlined above assumes perfect knowledge of the detector system. In reality this is not perfectly known. In order to understand this uncertainty, imperfections are introduced into the simulation of the detector system and the resulting change in the correction is assigned as the uncertainty. The following imperfections are introduced one-by-one and their effects on the correction are studied:
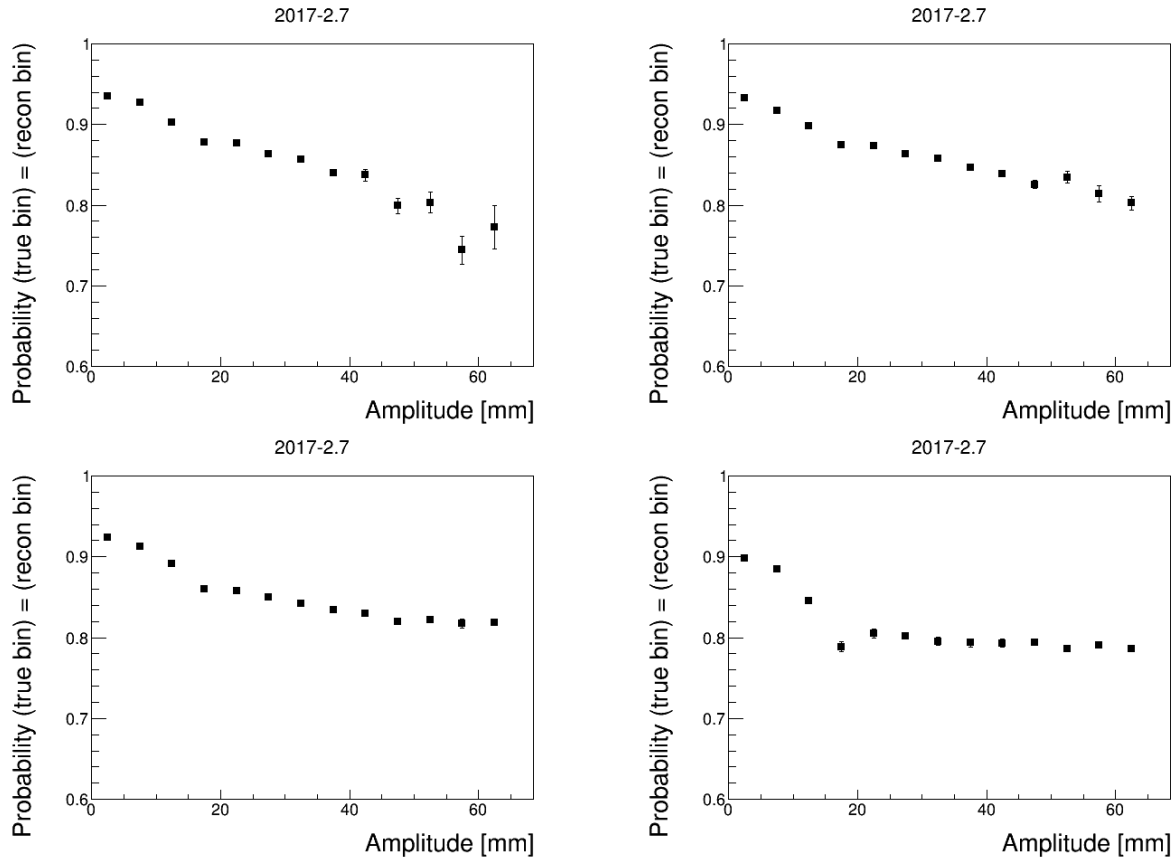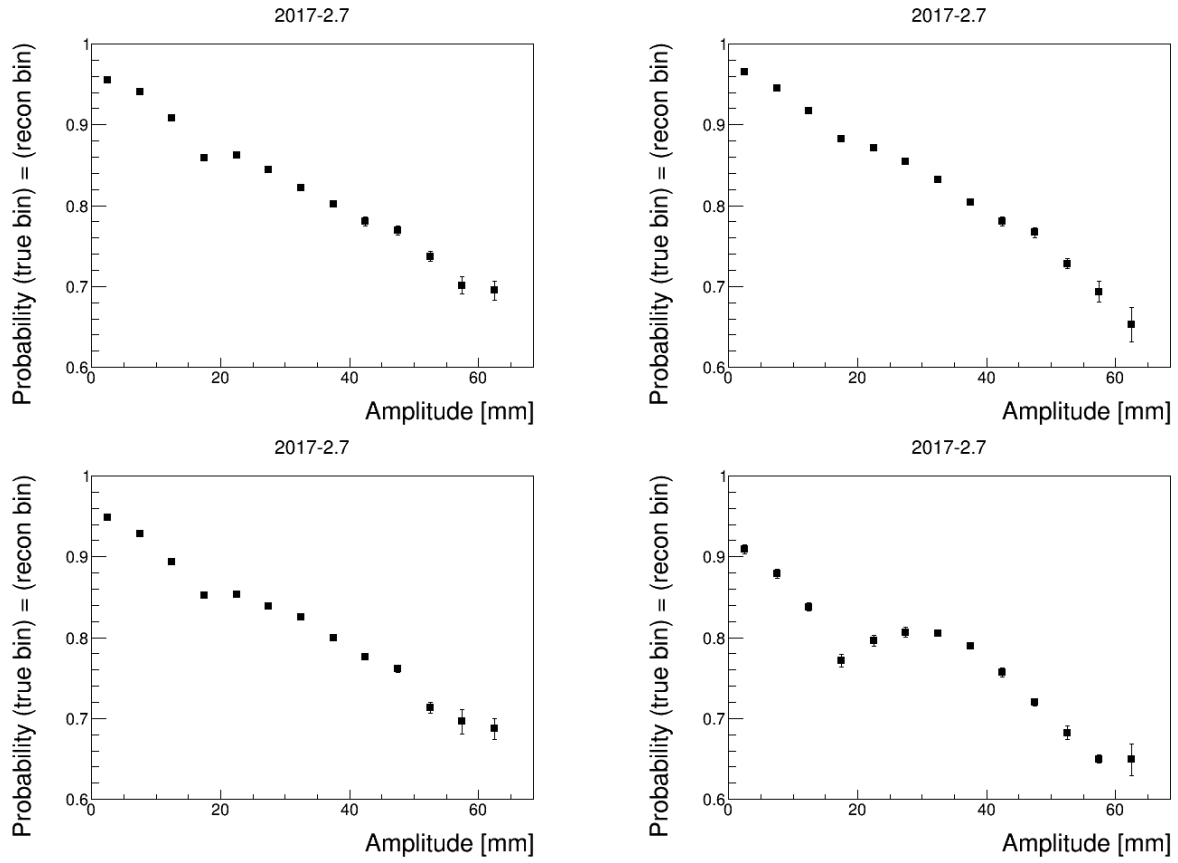
Figure 62: Probability of remaining in the true amplitude bin after reconstruction in TKU for 3-140 (top left); 4-140 (top right); 6-140 (bottom left) and 10-140 (bottom right) configurations.

- Displacement in the horizontal plane through 3 mm
- Rotation in the horizontal plane through 3 mrad
- Mispowering of the Centre coil by 3 %
- Mispowering of the End1 coil by 5 %
- Mispowering of the End2 coil by 5 %
- Increasing the tracker glue density by 50 %

The effect of each of these uncertainties on the correction coefficients is shown in fig. 65, 66 and 67.

It is noted that even with this large data set, statistical fluctuations in the uncertainties are significant.

Figure 63: Probability of remaining in the true amplitude bin after reconstruction in TKD for 3-140 (top left); 4-140 (top right); 6-140 (bottom left) and 10-140 (bottom right) configurations.
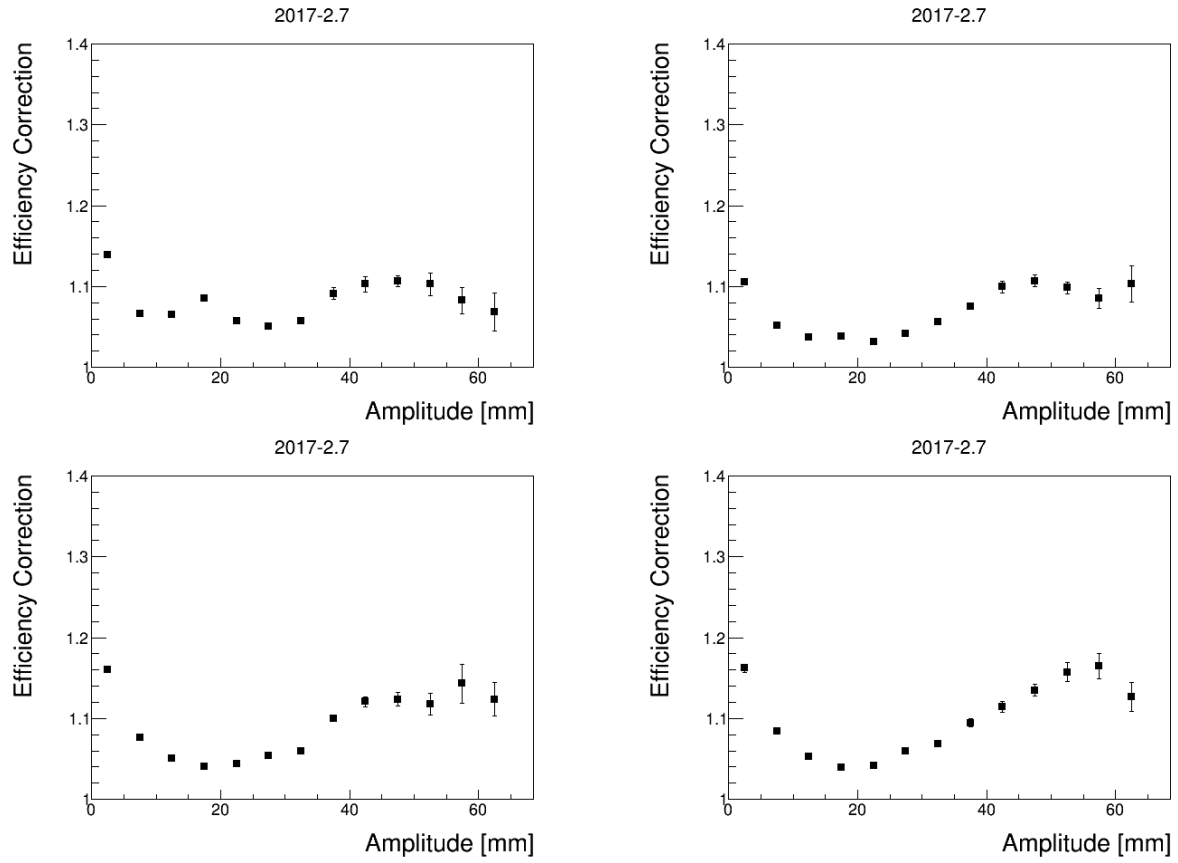
Figure 64: TKD efficiency correction for 3-140 (top left); 4-140 (top right); 6-140 (bottom left) and 10-140 (bottom right) configuratons.
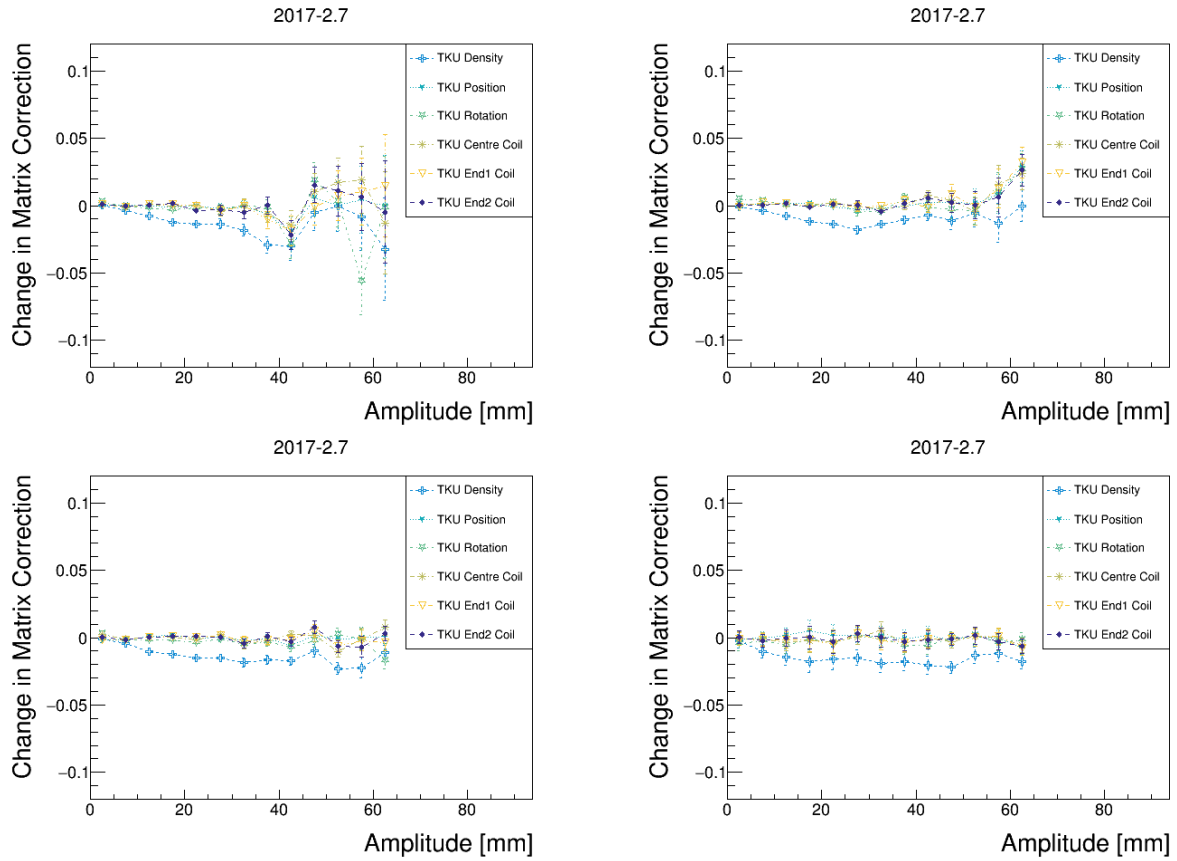
Figure 65: Effect on diagonal terms of the TKU **S** matrix for 3-140 (top left); 4-140 (top right); 6-140 (bottom left) and 10-140 (bottom right) configuratons.
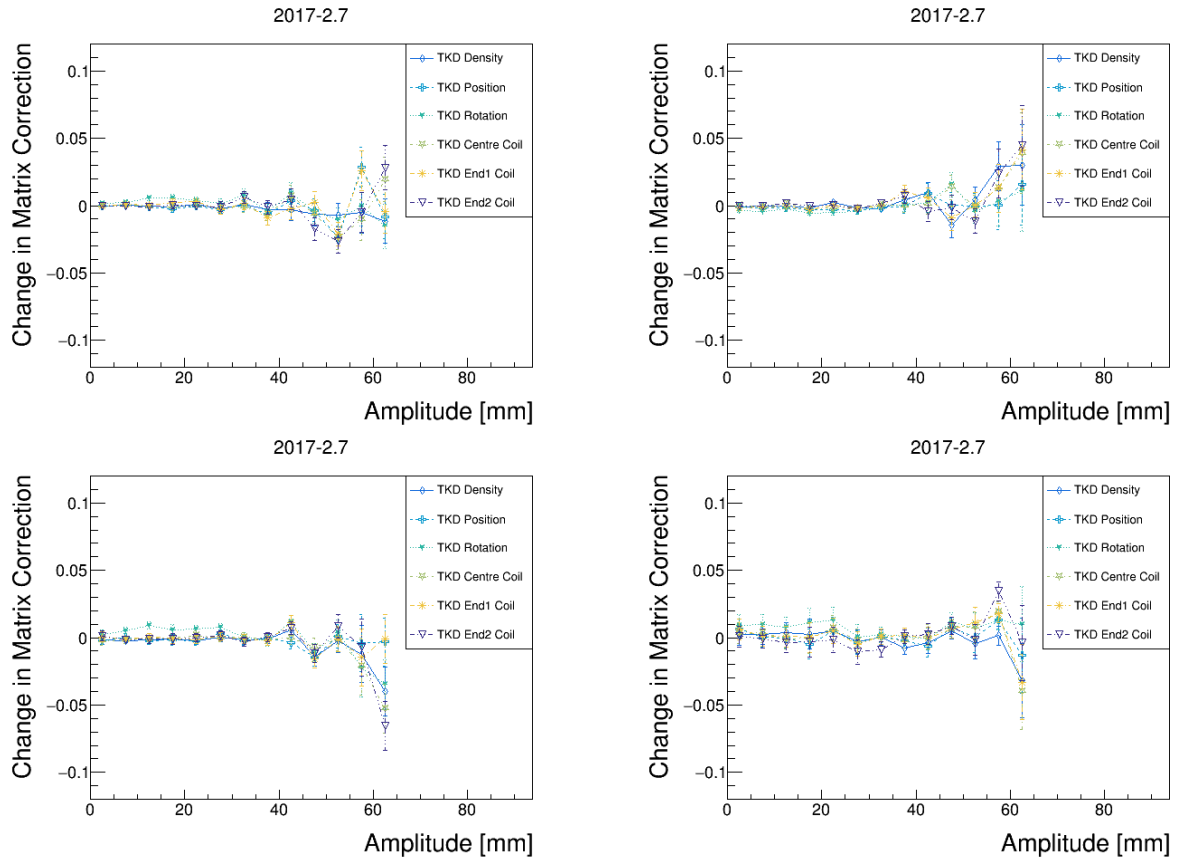
Figure 66: Effect on diagonal terms of the TKD **S** matrix for 3-140 (top left); 4-140 (top right); 6-140 (bottom left) and 10-140 (bottom right) configuratons.
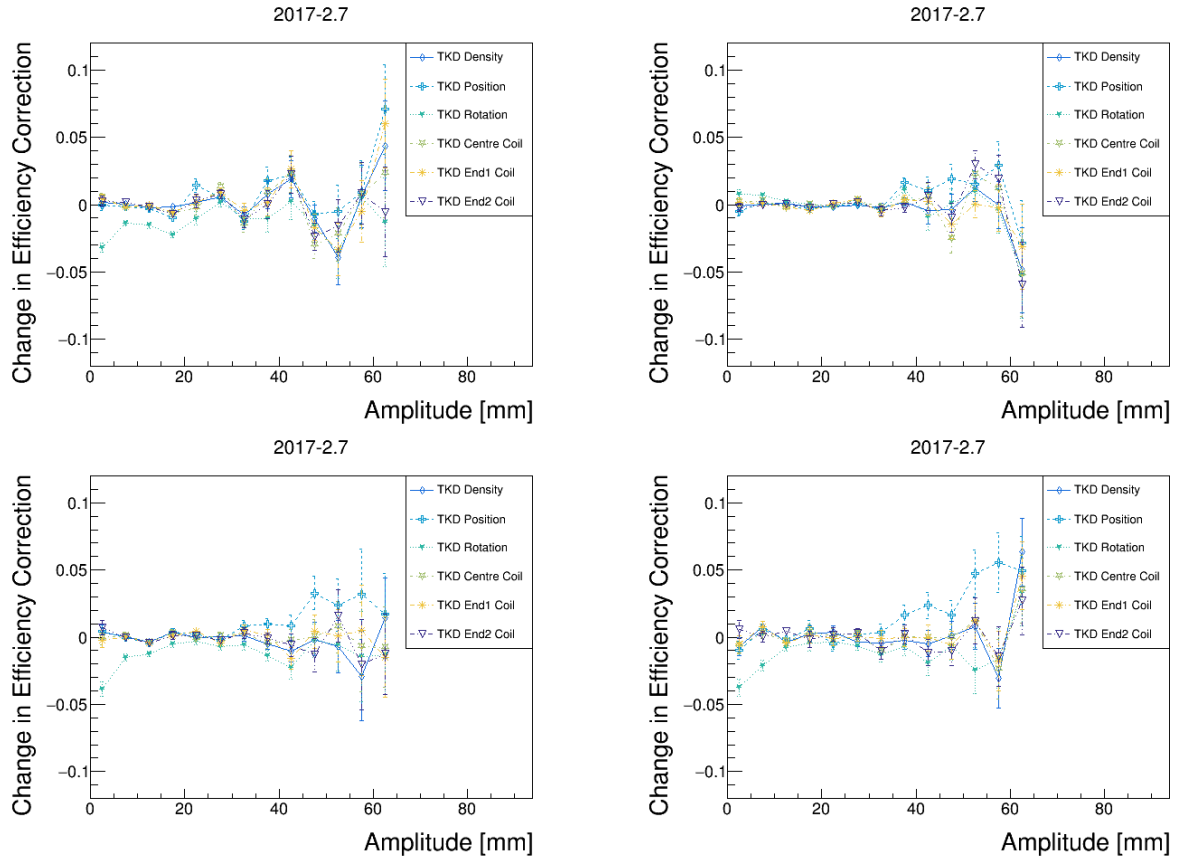
Figure 67: Effect on the efficiency **E** of varying the simulation geometry as compared to the reconstruction geometyr in TKD for 3-140 (top left); 4-140 (top right); 6-140 (bottom left) and 10-140 (bottom right) configuratons.

5.3 Results

The amplitude density and cumulative distributions are shown in fig. 68 and 69. The ratio of the downstream and upstream density distributions is shown in fig. 70. The ratio of the downstream and upstream cumulative distributions is shown in fig. 71. Where the ratio is greater than 1, the density has increased on passing between the trackers. If this occurs in the beam core, then it indicates events have migrated from the tail of the beam towards the core, which is indicative of cooling.

For all 3-140 settings, the number of events in the beam core is lower downstream than upstream indicating significant dilution of the beam core. The 3-140 setting exhibits significant mismatch and this dominates the amplitude evolution.

For the 4-140 settings the number of events in the beam core is approximately the same upstream and downstream. This setting is expected to be near to the equilibrium emittance of both absorbers.

For the 6-140 and 10-140 setting, the events traversing no absorber or with an empty hydrogen absorber do not exhibit a significant change in core density. The settings with a filled liquid hydrogen absorber or lithium hydride do exhibit a change in core density indicating migration of tracks towards the beam core when an absorber is installed. The 10-140 setting exhibits a greater increase in core density, at the expense of more loss in the tails due to scraping. The onset of scraping can be seen most clearly at above 40 mm.
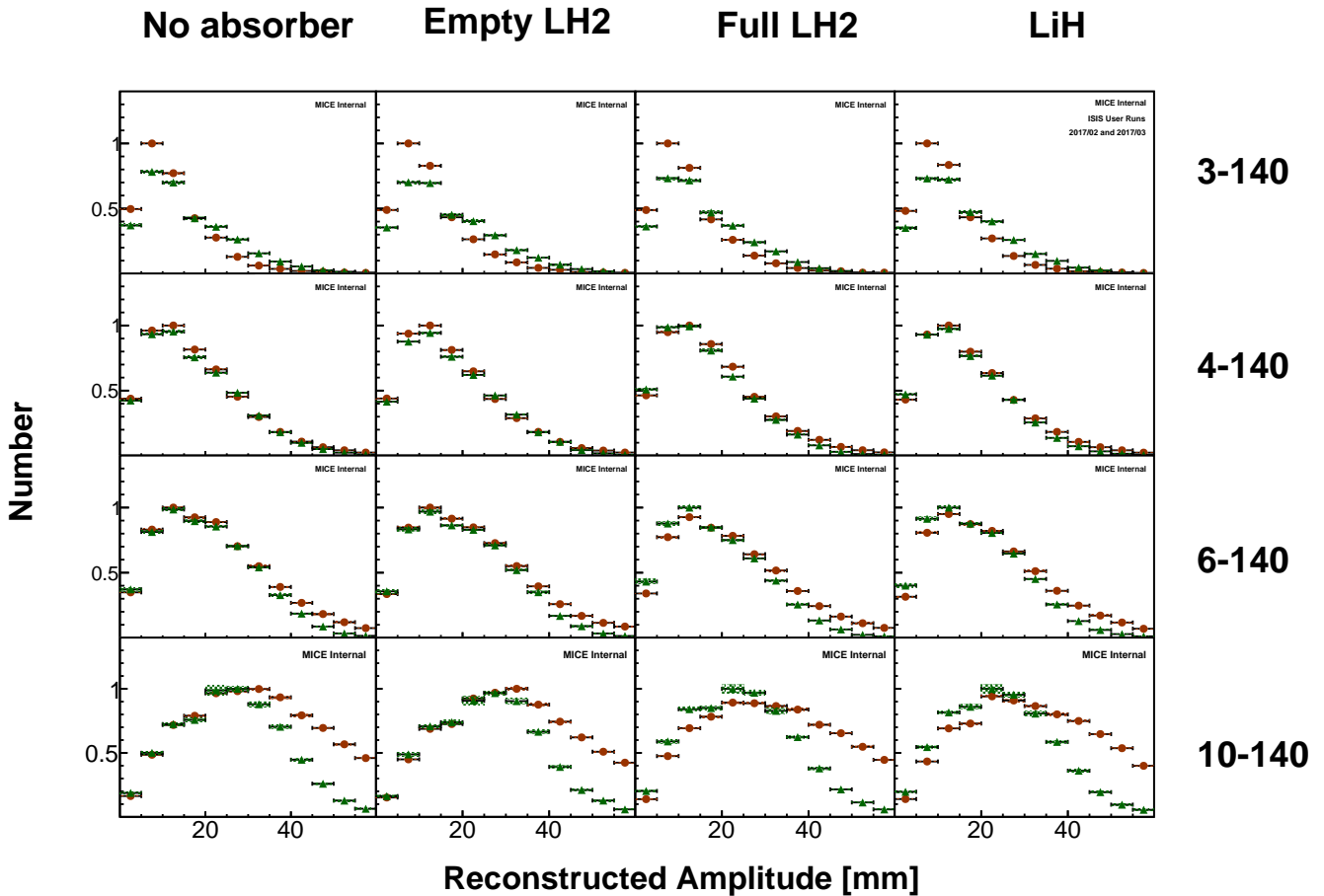

Figure 68: Distribution of amplitudes. The upstream distribution is shown by orange circles while the downstream distribution is shown by green triangles. Where significant, statistical uncertainty is represented by bars and systematic uncertainty by hashed boxes
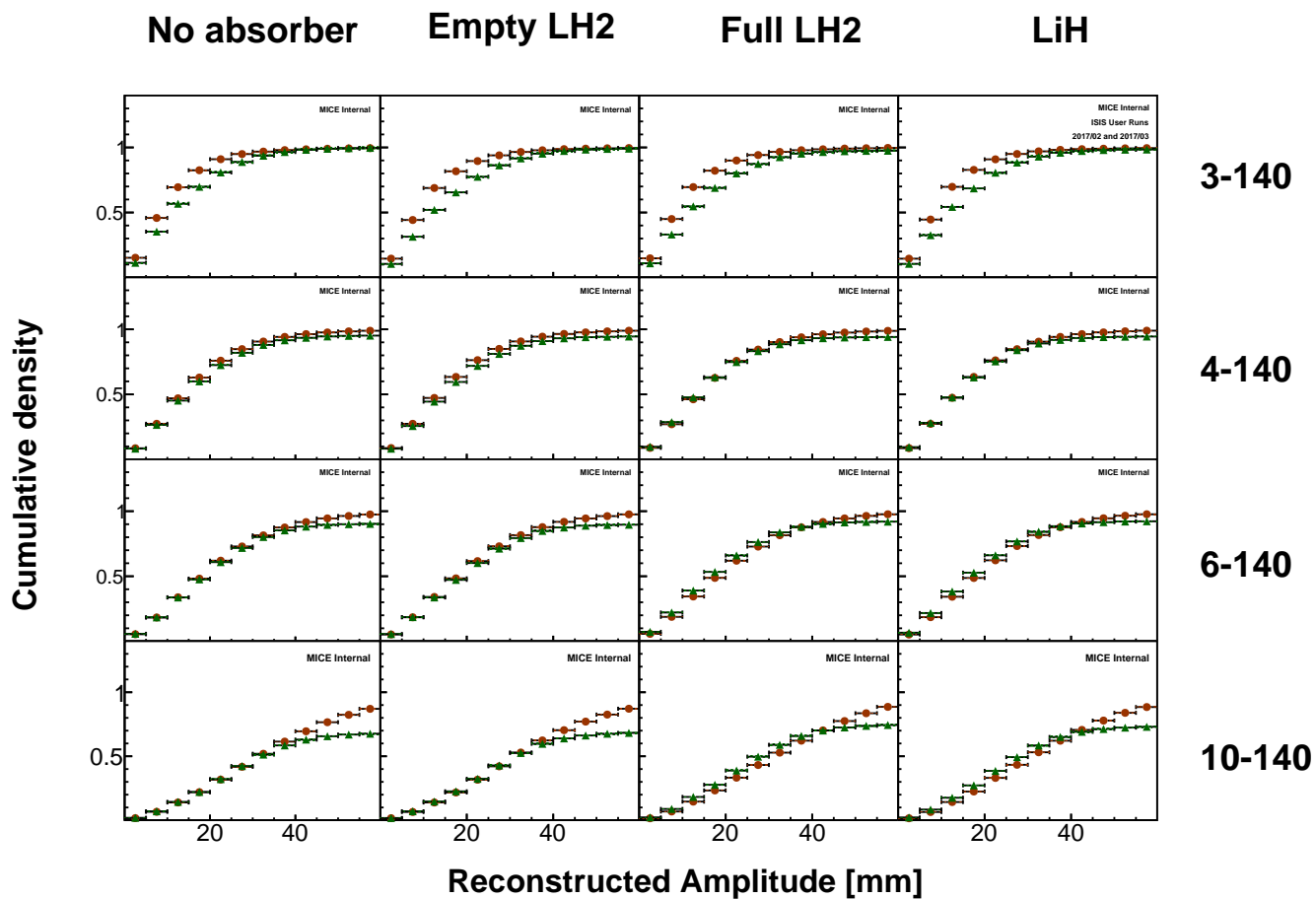
Figure 69: Cumulative amplitude distribution. The upstream distribution is shown by orange circles while the downstream distribution is shown by green triangles. Where significant, statistical uncertainty is represented by bars and systematic uncertainty by hashed boxes.
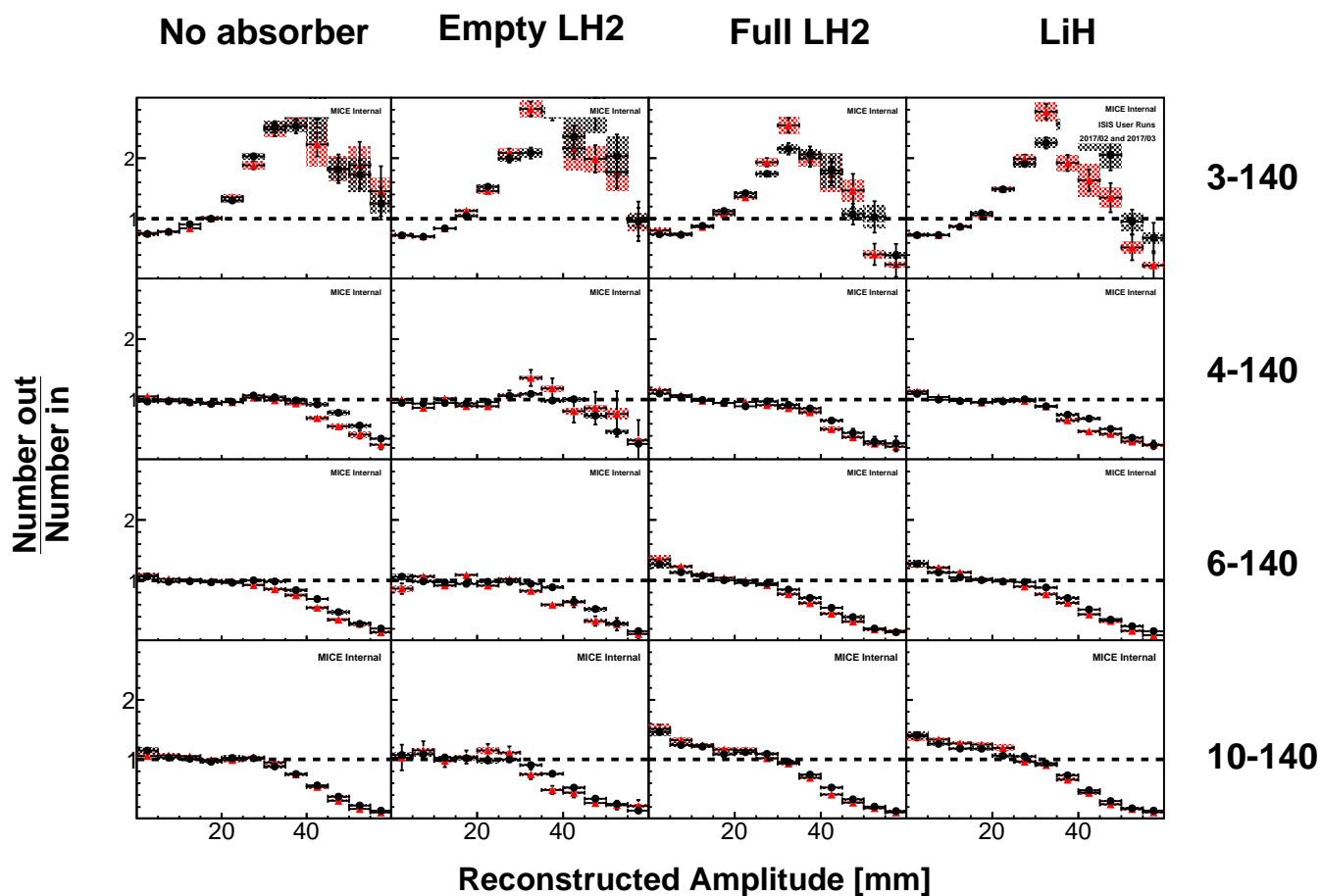
Figure 70: Ratio of amplitude density. Data is shown in black and simulation is shown in red. Statistical uncertainty is represented by bars and systematic uncertainty by hashed boxes.
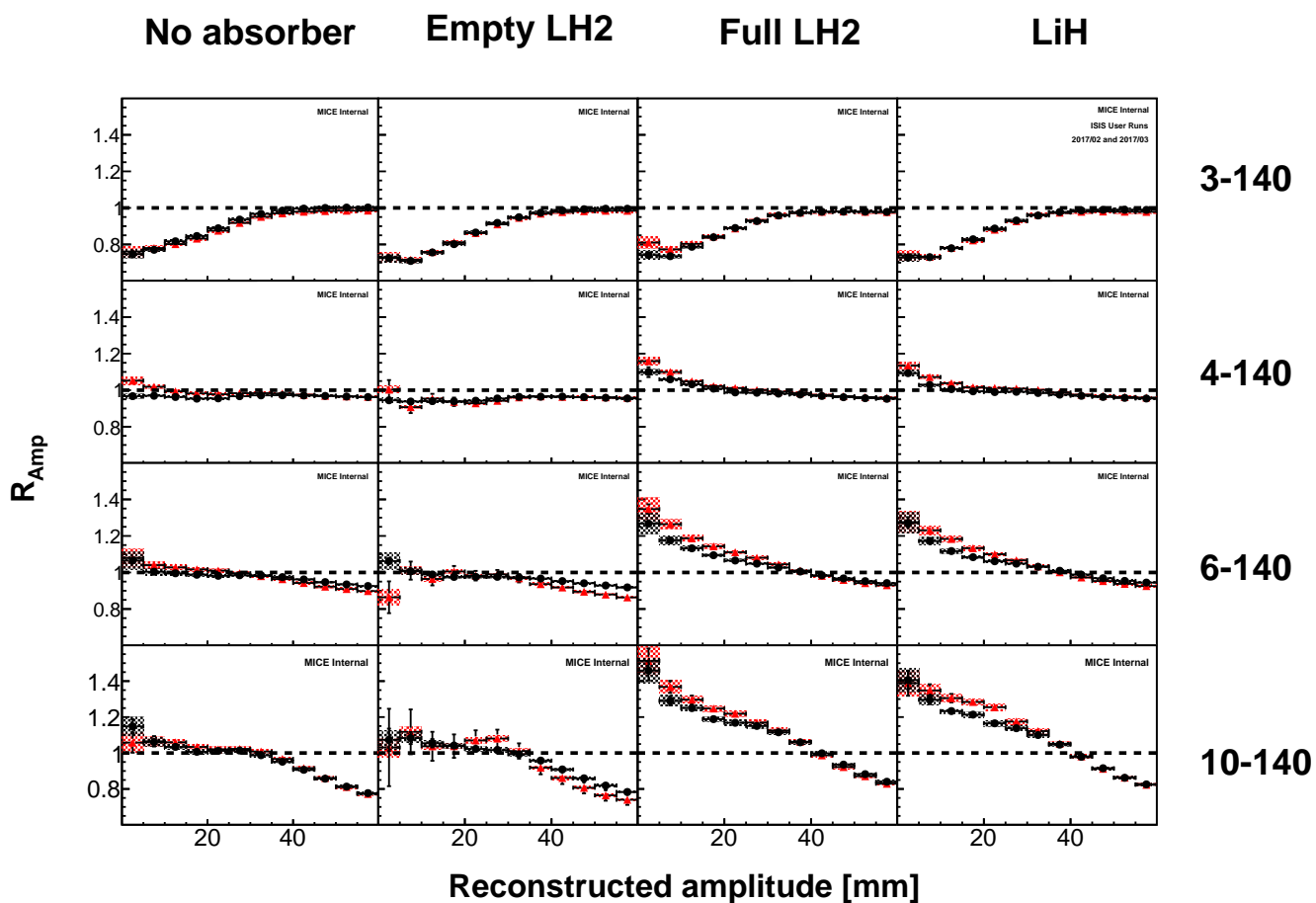
Figure 71: Ratio of amplitude cumulative distribution. Data is shown in black and simulation is shown in red. Statistical uncertainty is represented by bars and systematic uncertainty by hashed boxes.

6 Conclusions

An analysis has been presented of the evolution of amplitude in the presence of absorbers. As this is the first analysis to use the full MICE system including upstream and downstream detectors and fields, the system performance has been explored in detail.

The experiment has been described. The data selection has been described. The resolution of the trackers was discussed and the reconstructed tracker tracks were compared with each other and the ToF detectors following extrapolation through the fields.

The cooling channel was studied. Exceptional stability was demonstrated in the cooling channel magnets. The optical performance was studied and the extrapolated upstream optical functions were shown to agree well with the downstream optical functions. The energy loss in the absorber was shown to be stable and reasonable. The beam distributions of the beam upstream and downstream was shown.

The algorithm for amplitude calculation was outlined and shown to work with a toy distribution. A correction routine was discussed to correct for tracker resolution and inefficiency. The evaluation of uncertainties on the measurement was described.

The amplitude distributions were shown upstream and downstream of the absorber. For low input emittances or settings without an absorber, the beam core was shown to exhibit no increase in density while for high input emittances and settings with an absorber installed the beam core was shown to exhibit an increase in density. This is consistent with beam cooling. The amount of cooling observeved was broadly consistent with simulation.

References

[1] I need to do the references

[2] citation

[3] citation

[4] citation

[5] citation

[6] citation

[7] citation

[8] citation

[9] citation

[10] citation

[11] citation

[12] citation

[13] citation

[14] citation

[15] citation

[16] citation

[17] citation

[18] citation.

[19] citation

[20] citation.

[21] citation

[22] citation

[23] citation

R. Roser, A. Name[†]

Fermilab, P.O. Box 500, Batavia, IL 60510-5011, USA

[†] *Also at another institute*

K. Long

Physics Department, Blackett Laboratory, Imperial College London, Exhibition Road, London, SW7 2AZ, UK